

University of Windsor

## Scholarship at UWindor

---

Electronic Theses and Dissertations

Theses, Dissertations, and Major Papers

---

2010

### The Role of Turbulent Integral Length Scale on The Drag of a Circular Cylinder in Cross Flow

Nibras Younis  
*University of Windsor*

Follow this and additional works at: <https://scholar.uwindsor.ca/etd>

---

#### Recommended Citation

Younis, Nibras, "The Role of Turbulent Integral Length Scale on The Drag of a Circular Cylinder in Cross Flow" (2010). *Electronic Theses and Dissertations*. 216.

<https://scholar.uwindsor.ca/etd/216>

This online database contains the full-text of PhD dissertations and Masters' theses of University of Windsor students from 1954 forward. These documents are made available for personal study and research purposes only, in accordance with the Canadian Copyright Act and the Creative Commons license—CC BY-NC-ND (Attribution, Non-Commercial, No Derivative Works). Under this license, works must always be attributed to the copyright holder (original author), cannot be used for any commercial purposes, and may not be altered. Any other use would require the permission of the copyright holder. Students may inquire about withdrawing their dissertation and/or thesis from this database. For additional inquiries, please contact the repository administrator via email ([scholarship@uwindsor.ca](mailto:scholarship@uwindsor.ca)) or by telephone at 519-253-3000ext. 3208.

**The Role of Turbulent Integral Length Scale on The  
Drag of a Circular Cylinder in Cross Flow**

by

Nibras Younis

A Thesis

Submitted to the Faculty of Graduate Studies  
through the Department of Mechanical, Automotive & Materials Engineering  
in Partial Fulfillment of Requirements for  
the Degree of Master of Applied Science at the  
University of Windsor

Windsor, Ontario, Canada

2009

© 2009 Nibras Younis

**The Role of Turbulent Integral Length Scale on The  
Drag of a Circular Cylinder in Cross Flow**

by  
Nibras Younis

APPROVED BY:

---

Dr. S. Cheng, Outside Department Reader  
Department of Civil and Environmental Engineering

---

Dr. G. W. Rankin, Department Reader  
Department of Mechanical, Automotive & Material Engineering

---

Dr. D.S-K. Ting, Advisor  
Department of Mechanical, Automotive & Material Engineering

---

Dr. N. Zamani, Chair of Defense  
Department of Mechanical, Automotive & Material Engineering

25 August 2009

## **Author's Declaration of Originality**

I certify that I have obtained a written permission from the copyright owner(s) to include the above published material(s) in my thesis. I certify that the above material describes work completed during my registration as a graduate student at the University of Windsor.

I declare that, to the best of my knowledge, my thesis does not infringe upon anyone's copyright nor violate any proprietary rights and that any ideas, techniques, quotations, or any other material from the work of other people included in my thesis, published or otherwise, are fully acknowledged in accordance with the standard referencing practices. Furthermore, to the extent that I have included copyrighted material that surpasses the bounds of fair dealing within the meaning of the Canada Copyright Act, I certify that I have obtained a written permission from the copyright owner(s) to include such material(s) in my thesis.

I declare that this is a true copy of my thesis, including any final revisions, as approved by my thesis committee and the Graduate Studies office, and that this thesis has not been submitted for a higher degree to any other University or Institution.

## Abstract

The effects of the Reynolds number ( $Re$ ), freestream turbulence intensity ( $Tu$ ) and integral length scale ( $\Lambda$ ) on the drag coefficient ( $C_d$ ) of a circular cylinder in cross flow were experimentally studied for  $6.45 \times 10^3 < Re < 1.82 \times 10^4$ . ABS cylinders of three different diameters, and three aluminum orificed perforated plates were used.  $Tu$  was fixed at approximately 0.5%, 5%, 7% and 9% and the normalized integral length scale ( $\Lambda/D$ ) was varied from 0.35 to 1.05. Current smooth flow results are consistent with the standard  $C_d$  versus  $Re$  results in the literature. Present turbulent results have confirmed the general trend of decreasing  $C_d$  with increasing  $Tu$ . The effectiveness of  $Tu$  in reducing  $C_d$  is found to lessen with increasing  $\Lambda/D$ . Most interestingly, freestream turbulence of low  $Tu$  and large  $\Lambda/D$  can increase the  $C_d$  above the corresponding (same  $Re$ ) smooth flow value. Most significant  $C_d$  reduction of 74.7% was detected at  $Re=18200$ ,  $Tu=9\%$  and  $\Lambda/D=0.35$ .

## **Acknowledgements**

The author would like to express his sincere gratitude to Dr. David Ting for his excellent guidance and support during this study. The invaluable comments and assistance from the committee members are gratefully acknowledged. Technical assistance from the staff of the University of Windsor is appreciated. Gratitude goes especially to Mr. Patrick Seguin and to Mr. Andy Jenner who made most of the parts needed for this experiment.

The financial support from the Natural Sciences and Engineering Research Council of Canada in the form of Research Assistantship and Equipment Grants are gratefully acknowledged. The financial support from the Department of Mechanical, Automotive and Materials Engineering in the form of a Graduate Assistantship is acknowledged. Thanks also go to the Faculty of Graduate Studies and Research of the University of Windsor for awarding the author the University of Windsor Tuition Scholarship.

## Table of Contents

Author's Declaration of Originality.....	III
Abstract.....	IV
Acknowledgments.....	V
List of Tables.....	IX
List of Figures.....	X
Nomenclature.....	XIII
Chapter 1 Introduction.....	1
1.1 Objectives.....	1
1.2 Scope of Study.....	2
Chapter 2 Literature Review.....	2
2.1 Smooth flow past a smooth cylinder.....	2
2.1.1 Creeping flow or non-separation ( $0 < Re < 4 \sim 5$ ).....	3
2.1.2 Steady separation or closed near-wake ( $4 \sim 5 < Re < 30 \sim 48$ ).....	5
2.1.3 Periodic laminar ( $30 \sim 48 < Re < 180 \sim 200$ ).....	5
2.1.4 Transition of laminar eddies in the wake ( $180 \sim 200 < Re < 220 \sim 250$ ).....	6
2.1.5 Transition of an irregular eddy during its formation ( $220 \sim 250 < Re < 350 \sim 400$ ).....	6
2.1.6 Development of transition waves ( $350 \sim 400 < Re < 10^3 \sim 2 \times 10^3$ ).....	6
2.1.7 Formation of transition eddies ( $10^3 \sim 2 \times 10^3 < Re < 2 \times 10^4 \sim 4 \times 10^4$ ).....	7
2.1.8 Burst to turbulence ( $2 \times 10^4 \sim 4 \times 10^4 < Re < 1 \times 10^5 \sim 2 \times 10^5$ ).....	7
2.1.9 Precritical ( $1 \times 10^5 \sim 2 \times 10^5 < Re < 3 \times 10^5 \sim 3.4 \times 10^5$ ).....	7
2.1.10 One-bubble ( $3 \times 10^5 \sim 3.4 \times 10^5 < Re < 3.8 \times 10^5 \sim 4 \times 10^5$ ).....	8
2.1.11 Two-bubble ( $3.8 \times 10^5 \sim 4 \times 10^5 < Re < 5 \times 10^5 \sim 10^6$ ).....	9
2.1.12 Supercritical ( $5 \times 10^5 \sim 10^6 < Re < 3.4 \times 10^6 \sim 6 \times 10^6$ ).....	10
2.1.13 Post-critical ( $Re > 3.4 \times 10^6$ ).....	10

2.2 Turbulent flow.....	10
2.2.1 $Re < 2 \times 10^5$ .....	11
2.2.2 $2 \times 10^5 < Re < 6 \times 10^5$ .....	19
2.2.3 $Re > 6 \times 10^5$ .....	20
2.3 End plate effect.....	22
2.4 Blockage effect.....	25
2.5 Surface roughness effect.....	26
2.6 Moist air density.....	28
CHAPTER 3 Experimental Details.....	28
3.1 Wind tunnel and test model.....	28
3.2 Hot-wire anemometer.....	33
3.3 Traversing mechanism.....	33
3.4 Load cell.....	34
3.5 Orificed perforated plates.....	37
3.6 End plate design.....	38
CHAPTER 4 Data Analysis.....	39
4.1 Hot-wire data analysis.....	39
4.2 Drag coefficient.....	40
4.3 Taylor microscale procedure.....	42
4.4 Boundary layer effect .....	44
4.5 End plate effects on $C_d$ .....	45
4.6 Blockage effects on $C_d$ .....	46
4.7 The decay of turbulence downstream of the orificed perforated plate.....	47
4.8 Integral length scale.....	50
4.9 Taylor microscale.....	50
4.10 Re matrix .....	54
CHAPTER 5 Results and Discussion.....	56
5.1 Results Table .....	56
5.2 Cylinder drag under 'no turbulence' condition.....	58
5.3 The general effect of freestream turbulence .....	59



5.4 Effect of turbulent Reynolds number.....	60
5.5 Effect of turbulence intensity.....	62
5.6 Effect of integral length scale.....	64
5.7 Taylor microscale with drag coefficient .....	66
5.8 Drag results on a three dimensional curve.....	69
5.9 Current drag results comparison .....	69
CHAPTER 6 Conclusions and Recommendations.....	71
6.1 Conclusions.....	71
6.2 Recommendations.....	72
REFERENCES.....	73
APPENDIX A: MatLab Programs.....	78
A.1 Program to calculate the integral length scale.....	78
A.2 Program to calculate the air density.....	79
APPENDIX B: Data Acquisition Selection.....	81
B.1 Sample number.....	81
B.2 Sampling frequency.....	81
APPENDIX C: Hot-wire Probe Calibration .....	85
APPENDIX D: FFT for load cell output.....	86
D.1 FFT MatLab program.....	86
APPENDIX E: Taylor Microscale.....	87
APPENDIX F: Uncertainty Analysis.....	88
F.1 Uncertainty in Reynolds number .....	88
F.2 Uncertainty in drag coefficient.....	92
F.3 Uncertainty in turbulence intensity.....	96
F.4 Uncertainty in integral length scale.....	98
Vita Auctoris.....	101

## List of Tables

Table 1	Flow pattern & drag coefficient with Re [Bearman, 1969].....	9
Table 2	Freestream velocity selection to achieve 3 repeating values of Re.....	54
Table 3	The selection of the relative integral lengths by three turbulence intensities by three Res.....	55
Table 4	Summary of drag results, with the percentage change in the turbulent $C_d$ value .....	57
Table E.1	Mesh size for the orificed perforated plates.....	87

## List of Figures

Figure 1	Standard $C_d$ -Re curve.....	3
Figure 2	Wake behind a circular cylinder.....	4
Figure 3	Strouhal number versus Reynolds number.....	9
Figure 4	Standard $C_d$ -Re band.....	11
Figure 5	Strouhal number versus Re [Bearman, 1968].....	12
Figure 6	Turbulence intensity and $\Lambda/D$ effects on $C_d$ -Re [Bruun & Davies, 1975, Kiya et al., 1982, Surry, 1972].....	14
Figure 7	Turbulence intensity and $\Lambda/D$ effects on $C_d$ -Re [Savkar et al., 1980, Arie et al., 1981].....	15
Figure 8	$C_d$ -Re For different turbulence intensities [Cheung & Melbourne, 1983].....	21
Figure 9	St-Re For different turbulence intensities [Cheung & Melbourne, 1983].....	21
Figure 10	End plate design as recommended by Standby [1974] and confirmed by Fox [1992].....	23
Figure 11	End plate design used by Szepessy and Bearman [1992] (a) Cylinder with end plates (b) Side view of an end plate .....	24
Figure 12	The effect of blockage on $C_d$ -Re [Richter and Naudascher, 1976]...	25
Figure 13	Effect on surface roughness on the drag of a circular cylinder [Achenbach, 1971], $k_s$ is Nikuradse sand-grain roughness .....	27
Figure 14	The overall view of the wind tunnel.....	29
Figure 15	Cylinder in cross flow with end plate (a) Wind tunnel experiment setup (b) End plate location.....	31
Figure 16	Actual setup with the end plate in the wind tunnel (a) End plate connection assembly with a 48 mm length connection piece (b) Load cell connection.....	32
Figure 17	The light-duty 2-D traversing mechanism.....	34

Figure 18	Load cell attached to the aluminum angle.....	35
Figure 19	Load cell, calibration check.....	36
Figure 20	The orificed perforated plates (a) d25, d37.5, and d50 (b) Looking upstream to the plate (c) Cross section of the plate .....	37
Figure 21	End plate.....	38
Figure 22	Integral length scale for d37.5 plate @ 20 x/d and $U_0 = 5.51$ m/s.....	40
Figure 23	Load cell sample size check, 26.7 mm cylinder, $Tu=5\%$ , and $U_0=10.7$ m/s .....	41
Figure 24	Taylor microscale for d37.5 plate @ 20 x/d and $U_0 = 5.51$ m/s (a) Taylor microscale (b) Zoom in the contact between the autocorrelation and the parabola.....	43
Figure 25	Wind tunnel boundary layer check (a) $U_0 = 2.1$ m/s (b) $U_0=10.7$ m/s.....	44
Figure 26	Dummy piece to check the effect of end plate.....	45
Figure 27	End plate effects on $C_d$ .....	46
Figure 28	Blockage effects on $C_d$ .....	47
Figure 29	Turbulence intensity downstream of (a) d25 Plate (b) d37.5 Plate (c) d50 Plate.....	49
Figure 30	Integral length scales downstream of (a) d25 Plate (b) d37.5 Plate (c) d50 Plate.....	51
Figure 31	Taylor microscale downstream of (a) d25 Plate (b) d37.5 Plate (c) d50 Plate.....	52
Figure 32	Sample curve fits for $\lambda$ versus x/d (d25 plate).....	53
Figure 33	Results for smooth flow on the standard curve.....	58
Figure 34	$\Lambda/D=0.35$ Current study results with respect to [Brunn & Davies, 1975, Surry, 1972].....	59
Figure 35	Re Effects (a) $\Lambda/D=1.05$ (b) $\Lambda/D=0.7$ (c) $\Lambda/D=0.35$ .....	61

Figure 36	Tu Effects (a) $\Lambda/D=1.05$ (b) $\Lambda/D=0.7$ (c) $\Lambda/D=0.35$ .....	63
Figure 37	$\Lambda/D$ Effects (a) Tu=5% (b) Tu=7% (c) Tu=9%.....	65
Figure 38	Integral length scale/Taylor microscale versus $C_d$ , $D = 48.5\text{mm}$ .....	66
Figure 39	Integral length scale/Taylor microscale versus $C_d$ , $D = 26.7\text{mm}$ .....	67
Figure 40	Drag results for the current study.....	68
Figure 41	Drag results comparison (a) Current drag results when Tu = 9% compared to Savkar et al. [1980], Tu = 9.5% and Arie et al. [1981], Tu = 9.3% (b) Current drag results when Tu = 5% compared to Arie et al. [1981], Tu = 5.4%.....	70
Figure 42	Current drag results compared to Bruun & Davies, [1975], Arie et al. [1981], Surry [1972], and Kiya et al. [1982].....	71
Figure B1	Sample size check for d25 plate located at 20 x/d and $U_0 = 8.1$ m/s (a) $U_{\text{mean}}$ (b) $U_{\text{rms}}$ (c) Tu % (d) Integral length scale ( $\Lambda$ ).....	82
Figure B2	Sample size check for d37.5 plate located at 20 x/d and $U_0 = 8.1$ m/s (a) $U_{\text{mean}}$ (b) $U_{\text{rms}}$ (c) Tu% (d) Integral length scale ( $\Lambda$ ).....	83
Figure B3	Sample size check for d50 plate located at 20 x/d and $U_0 = 8.1$ m/s (a) $U_{\text{mean}}$ (b) $U_{\text{rms}}$ (c) Tu % (d) Integral length scale ( $\Lambda$ ).....	84
Figure D1	Frequency for 26.7 mm cylinder, Tu=5%, and $U_0=10.7$ m/s .....	86

## Nomenclature

A	Cylinder frontal area, $A = L \times D$ (m <sup>2</sup> )
B	Blockage ratio
B <sub>f</sub>	Coefficient fit (equal to 0.0209)
C <sub>0</sub> , C <sub>1</sub> , C <sub>2</sub> , C <sub>3</sub> , C <sub>4</sub>	Hot-wire calibration coefficients
C <sub>d</sub>	Nondimensional drag coefficient, $C_d = \frac{2 \times F_d}{\rho \times U_0^2 \times A}$
d	Perforated plate holes diameter (mm)
D	Cylinder diameter (mm)
E	Voltage data of 1D probe (mV)
F <sub>d</sub>	Drag force (N)
F <sub>D</sub>	Drop force (N)
F(r)	Autocorrelation function
F <sub>s</sub>	Shedding frequency (Hz)
f <sub>s</sub>	Sampling frequency (kHz)
H	Wind tunnel height (m)
k <sub>s</sub>	Nikuradse sand-grain roughness (m)
K	Define as, $K = B_f \left( t - \frac{X_0}{U} \right)^{-n}$
n	Power law decay
N	Sample size
M	Value varies from 0 to N-1.
M <sub>s</sub>	Mesh size for the orificed perforated plate (mm)
L	Cylinder length (mm)
P	Air pressure (kPa)
ΔP	Pressure difference across the Pitot-tube (kPa)
r	Eddy size ( m )
Re	Reynolds number, $Re = \frac{\rho \times U_0 \times D}{\mu}$
rms	Root mean square

St	Strouhal number, $St = \frac{F_s \times D}{U}$
t	Elapsing time (s)
T	Air temperature (°C)
Tu	Turbulence intensity $\frac{u_{rms}}{U}$ (%)
U	Calibrator velocity (m/s)
$U_0$	Free stream velocity (m/s)
$\bar{U}$	Time-averaged velocity (m/s)
$U_i$	Instantaneous velocity (m/s)
u	Instantaneous fluctuating velocity (m/s)
$\overline{u^2}$	Turbulence variance (m/s) <sup>2</sup>
$u_{rms}$	Root mean square velocity (m/s)
$U_{eff}$	Effective velocity in x component (m/s)
W	Uncertainty
x	Wind tunnel x direction
$X_0$	Virtual origin, equal to 7 × mesh size (mm)
y	Wind tunnel y direction

#### Greek Symbols

$\Lambda$	Integral length scale (mm)
$\mu$	Dynamic viscosity ( $\frac{kg}{m \times s}$ )
$\nu$	Kinematic viscosity (m <sup>2</sup> /s)
$\rho$	Air density (kg/m <sup>3</sup> )
$\tau$	Time (s)
$\tau_\Lambda$	Integral time scale (s)
$\lambda$	Taylor microscale (mm)

## **CHAPTER 1 Introduction**

A cylindrical body in cross flow is a common scenario in nature and in widespread applications of aeronautical, civil, mechanical, and chemical engineering. Circular cylinders are the basic component of tubular heat exchangers, where vibration problems may occur due to flow-induced forces. Other examples where the flow around and the fluid forces on cylindrical objects are of great significance include nuclear reactors, offshore/marine structures, submarine cables, cooling towers, chimney stacks, tall buildings/towers and power transmission lines. Although the circular cylinder geometry is simple, the variety of flow phenomena and their interactions are very complicated.

The wake behind a circular cylinder is typically turbulent and so is the oncoming flow. A working knowledge of turbulent phenomena is essential in the practice of engineering and it is one of the most fundamental flow configurations in fluid mechanics. The flow around and the wake of the cylinder are detected by the cylinder characteristics (size and surface roughness), and flow characteristics (Reynolds number, turbulence intensity, and integral length scale). Changing these parameters can significantly alter the boundary layer, separation point, and the structure of the wake.

Knowledge of flow past a circular cylinder in cross flow has been accumulated over a century. Even though many researchers have considered the freestream turbulence parameters, however, due to the fact that turbulence is a multi-aspect topic with dependency of one turbulent parameter on another, there is a lack of systematic studies focusing on the role of the integral length scale and its interaction with other turbulence parameters and the overall effects on the cylinder drag and wake structure.

### **1.1 Objectives**

The focus of this study is on the independent effects of freestream Reynolds number ( $Re$ ), turbulence intensity ( $Tu$ ), and the integral length scale/cylinder diameter ratio ( $\Lambda/D$ ) on the drag coefficient of a circular cylinder. The investigation was conducted in a closed-loop wind tunnel. The proper combination of orificed perforated plate hole diameter, cylinder location downstream with respect to the orificed perforated plates, and the wind speed in the wind tunnel enabled the quasi-independent alterations of turbulence intensity and relative integral length scale.



## 1.2 Scope of Study

In the current study, the effects of  $Tu$  and  $\Lambda/D$  of freestream turbulent flow generated downstream of the orificed perforated plates on the drag coefficient of a circular cylinder in cross flow were examined experimentally for three different values of Reynolds number. The experiments were conducted in a closed-loop wind tunnel. In order to measure the turbulence parameters, a single normal Dantec hot-wire probe of DISA type 55P11 was used. To measure the drag forces a six component load cell (ATI Industrial Automation include Force/Torque data acquisition, and F/T transducer, Gamma version SI-32-2.5) was used.

Within the available equipment limitations, the Reynolds number range based on freestream velocity, and cylinder diameter was altered from  $6.45 \times 10^3$  to  $1.82 \times 10^4$ , turbulence intensity ( $Tu$ ) was fixed at 0.5%, 5%, 7%, and 9%, and ( $\Lambda/D$ ) was varied from 0.35 to 1.05, by the utilization of orificed perforated plates.

## CHAPTER 2 Literature Review

The circular cylinder in cross flow received a great deal of attention because it is of both scientific and practical interest. This section provides a review of a circular cylinder in cross flow.

### 2.1 Smooth flow past a smooth cylinder

When a single, smooth cylinder is subject to a steady, isothermal, non-turbulent flow, distinct flow patterns occur with only very limited variation, over ranges of  $Re$  which are called flow regimes. Hence, the start and end of all flow regimes can be specified by  $Re$  alone [Zdravkovich, 1997].

From the drag curves plotted in the published papers and books reviewed, the standard curve for the drag coefficient versus Reynolds number was assembled, by using a digitizer, as shown in Figure 1. The five most important references are mentioned in the Figure. Four different regimes are identified by Achenbach [1971] and confirmed by Zdravkovich [1997] specifically, subcritical regime up to  $Re$  of  $2 \times 10^5$ , precritical regime  $2 \times 10^5 < Re < 3.4 \times 10^5$ , critical regime  $3.4 \times 10^5 < Re < 5 \times 10^5$ , and supercritical regime  $5 \times 10^5 < Re < 6 \times 10^6$ . When  $Re > 6 \times 10^6$  (transcritical) is so overwhelming that a

discussion of it has to be left out of this section. The wake behind a circular cylinder is shown in Figure 2 for different values of  $Re$ .

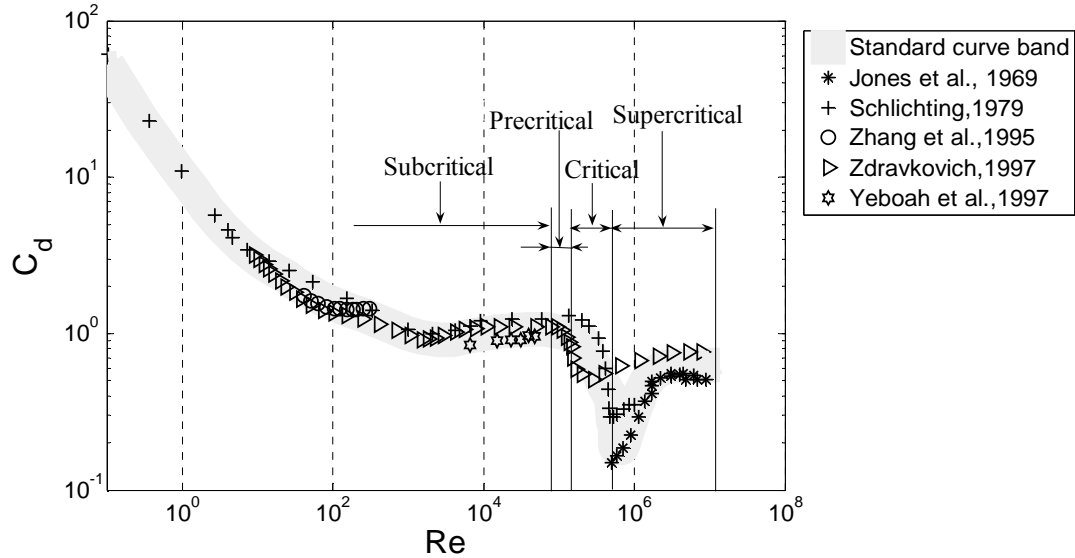


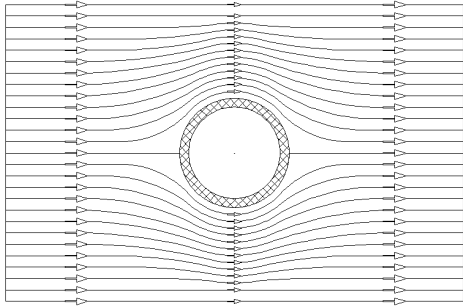
Figure 1 Standard  $C_d$ - $Re$  curve

### 2.1.1 Creeping flow or non-separation ( $0 < Re < 4 \sim 5$ )

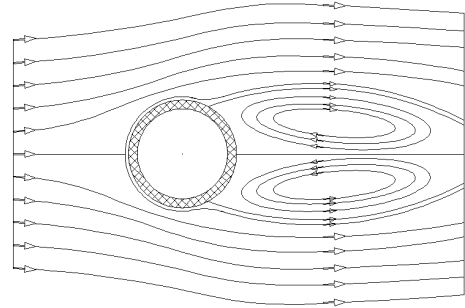
For  $Re < 5$ , streamlines firmly attach around the cylinder circumference with no visible wake behind the cylinder. Vronskaya and Taganov [1979] determined experimentally the value of drag coefficient for a high aspect ratio circular cylinder for  $Re$  range of  $10^{-4}$  to  $10^{-1}$  by using the free fall method and compared the experiment results (quite close) with those of Tritton [1959], where  $F_D$  is the drop force (N),

$$F_D = 4 + 2\pi/Re \quad (1)$$

Taneda [1963] studied the stability of a two-dimensional laminar flow and found, theoretically, the critical value of  $Re$ , below which all disturbances are damped, to be 3.2 as compared to the experimental value of 1.0. This discrepancy is due to the theoretical assumption of the parallel mean flow while experiments indicate that the wake widens slightly downstream for small  $Re$ .



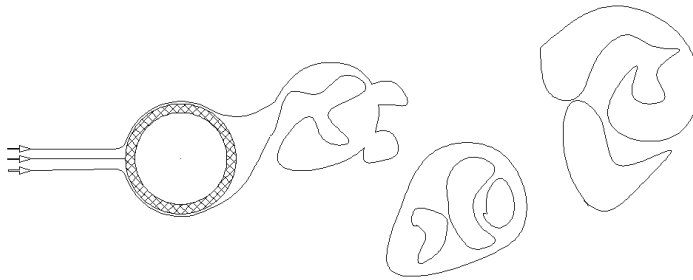
$Re \leq 5$



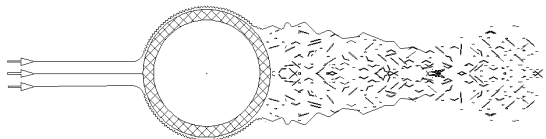
$Re \approx 45$



$Re \approx 140$



$Re \approx 400$



$Re \approx 3.4 \times 10^5$

Figure 2 Wake behind a circular cylinder

### 2.1.2 Steady separation or closed near-wake ( $4 \sim 5 < Re < 30 \sim 48$ )

Steady, symmetric and closed near-wake is observed for  $4 \sim 5 < Re < 30 \sim 48$ , the free shear layers come together at the confluence point which is at the end of the near-wake. Coutanceau and Bouard [1977] used a visualization method to investigate the detailed features for the flow passing a circular cylinder with a  $Re$  of 5 to 40 and they found the wake length increases linearly with increasing  $Re$ .

Taneda [1956] photographed the wake behind the cylinders for  $Re$  from 0.1 to 2000. He found that the rear twin vortices begin to form at  $Re \approx 5$  and they become larger as  $Re$  increases. At  $Re \approx 30$  the laminar wake starts to oscillate sinusoidally some distance downstream, and at  $Re \approx 45$  the twin vortices are asymmetrical.

Nishioka and Sato [1974] determined a circular cylinder drag coefficient for  $Re$  range of 10 to 80 and compared their results to Imai's [1951] analytical formulae which find the drag coefficient for a circular cylinder when  $Re < 5$  and  $Re > 5$  as follows:

$$C_d = \frac{8 \pi}{Re(\log \frac{D}{2} - \frac{1}{4} - \frac{4}{D^4})} \quad Re < 5 \quad (2)$$

$$C_d = (0.707 + \frac{3.42}{\sqrt{Re}})^2 \quad 5 < Re \quad (3)$$

### 2.1.3 Periodic laminar ( $30 \sim 48 < Re < 180 \sim 200$ )

A sinusoidal oscillation of the shear layers are initiated at the confluence point as a result of the instability of the elongated near-wake. As the  $Re$  increases the amplitude of the trail oscillation increases. Finally, a staggered array of laminar eddies are produced which are called the von-Karman vortex street.

Wen et al. [2004] investigated by visualization the drag force in combination with the wake patterns, which were behind a circular cylinder for  $Re$  from 35 to 560 by using both a horizontal and vertical soap tunnel. They found that when  $Re < 46$  the flow is steady and a pair of counter-rotating vortices forms symmetrically about the centerline of the wake. At  $Re \approx 46$  this configuration becomes unstable resulting in the well-known von-Karman vortex street.

#### **2.1.4 Transition of laminar eddies in the wake ( $180 \sim 200 < Re < 220 \sim 250$ )**

At Reynolds numbers higher than about 180 the laminar periodic wake becomes unstable. Zhang et al. [1995] observed through their experimental and numerical investigation, the flow over a circular cylinder with Re range of 40 to 300. Their computed Strouhal number (St) values increase from 0.13 to 0.21 over their Re range. Four physically dissimilar instabilities were observed, a hard vortex-adhesion (common in experiments as cylinder end effects always supply rise to finite localized 3-D perturbations, which initiates at either cylinder ends), and three-near wake instabilities. All four instability processes can originate in a narrow Re interval between 160 and 230. Their drag measurements were shown in Figure 1.

#### **2.1.5 Transition of an irregular eddy during its formation ( $220 \sim 250 < Re < 350 \sim 400$ )**

Eddies are formed laminar and regular but become irregular and transitional further downstream, the continuous distortion of laminar eddy leads ultimately to their breakdown. Karniadakis and Triantafyllou [1992] confirmed that a fast transition in the cylinder wake occurs, from a laminar two-dimensional state at Re close to 200 to turbulent state at Re of 400. The wake first becomes three-dimensional, as a result of a secondary instability of the two-dimensional von-Karman vortex street (at Re of 200), a harmonic state develops, in which the flow oscillates at its fundamental Strouhal number.

#### **2.1.6 Development of transition waves ( $350 \sim 400 < Re < 10^3 \sim 2 \times 10^3$ )**

If the boundary layer remains fully laminar, the transition waves appear as undulations of the free shear layer. Kwon et al. [1992] investigated the flow passing a circular cylinder over a Re range of 600 to 1600, their aim was to integrate a digital image processing technique and acquire detailed data on the drag coefficient in this range. They discussed that a small drag reduction over this range of Re ( $C_d$ -Re curve tend to decrease as Re increases) as shown in Figure 1, and this is more effective as the shear parameter (depends on the velocity gradient) increased. The value of Strouhal number is fairly constant around the value of 0.21 when  $700 < Re < 1400$ .

### **2.1.7 Formation of transition eddies ( $10^3 \sim 2 \times 10^3 < Re < 2 \times 10^4 \sim 4 \times 10^4$ )**

Transition waves roll up into discrete eddies and then roll up to alternate eddies. Lee et al. [2005] investigated experimentally the flow over a smooth and v-grooved circular cylinders in cross flow with Re range of  $2.5 \times 10^3$  to  $3.8 \times 10^4$ . Their smooth circular cylinder results confirmed that the drag coefficient over their Re range have a value of 1.1 to 1.2. Their results were with close agreement with Yeboah et al. [1997] who investigated experimentally the effect of (smooth and turbulent) flow over smooth cylinder with Re range of  $1.4 \times 10^3$  to  $4.8 \times 10^4$ , however their smooth flow  $C_d$  values were near 1 for their Re range.

### **2.1.8 Burst to turbulence ( $2 \times 10^4 \sim 4 \times 10^4 < Re < 1 \times 10^5 \sim 2 \times 10^5$ )**

A sudden burst to turbulence occurs in the free shear layer near the cylinder side and eddy formation occurs near to the rear of the cylinder. Maekawa and Mizuno [1967] classified eleven hot-wire signals near wake at  $Re = 6.5 \times 10^4$ . They found that all the signals represent one period of eddy shedding. Achenbach [1971] found that in the subcritical regime the drag coefficient is nearly constant at a value of 1.2. Sumner and Akosile [2003] conducted an experimental investigations of a circular cylinder in a uniform shear flow, with a Re range of  $4 \times 10^4$  to  $9 \times 10^4$ . Their smooth flow results confirmed that over their Re range; the drag coefficient and the Strouhal number (as shown in Figure 1 and Figure 3) have nearly constant values of 1.2 and 0.2, respectively.

### **2.1.9 Precritical ( $1 \times 10^5 \sim 2 \times 10^5 < Re < 3 \times 10^5 \sim 3.4 \times 10^5$ )**

The intrinsic three-dimensionality of the commencement of the transition disturbed the near-wake which postponed the eddy formation, the consequence was an initial fall in the drag coefficient. At certain Re this regime suddenly terminates associated with a discontinuous drag reduction as shown in Figure 1 and jump in the shedding frequency as shown in Figure 3. Thoman and Szweczyk [1969] conducted a stable finite difference method; an explicit type including a directional difference scheme used for nonlinear terms. Their method extended to high Reynolds flow around a circular cylinder ( $1 \times 10^5$  to  $3 \times 10^5$ ). The comparison of the numerical results with the experimental data

of Relf and Simmons [1925] showed good agreement when fine hybrid cell structure was used. They confirmed that excessive care was needed to select the cell mesh to avoid the artificial viscosity effect. However, their solution was limited to two-dimensional flow, so wake turbulence (three-dimension effects) could not be predicted.

Farell and Blessmann [1983] investigated experimentally the flow over a circular cylinder in the critical Re; they identified two subregimes in the lower transition. The first ( $1.5 \times 10^5$  to  $3 \times 10^5$ ), characterized by symmetric pressure distributions, intense vortex shedding, and major variations in parameters as the Re gets larger, however, the Strouhal number slightly decreases, as shown in Figure 3. The second characterized by extreme flow oscillations as a result of the formation and bursting of a single bubble on any side of the cylinder, at first intermittently on either side. As Re increased, the bubble formed in an alternating fashion. A two-bubble flow pattern alternates and it becomes steady with symmetric pressure distribution. They confirmed that the critical range can take place at the beginning of  $Re = 1.5 \times 10^5$  where  $C_d$  starts to fall, and ends when  $Re = 3.8 \times 10^5$  where a twin-bubbles flow forms. The transition between these two regimes is gradual and can be placed at  $Re = 3 \times 10^5$ .

#### **2.1.10 One-bubble ( $3 \times 10^5 \sim 3.4 \times 10^5 < Re < 3.8 \times 10^5 \sim 4 \times 10^5$ )**

The free shear layers suffered adequate transition to be able to reattach onto the surface of the cylinder. A separation bubble is a closed thin separated region. Bearman [1969] examined, experimentally, the flow over a circular cylinder for  $10^5 < Re < 7.5 \times 10^5$ . He confirmed that the strongest indications of shedding achieved by observing the output of a hot-wire probe located in the wake region (one cylinder diameter from the rear of the cylinder and half diameter from the wake center line) instead of near the cylinder surface. He observed a narrow band of vortex shedding over the range of Re. In the one-bubble Re range the shedding occurred at a Strouhal number of about 0.32 as shown in Figure 3. In the same Figure the standard curve band was plotted for six earlier researchers. His drag coefficient values with the flow pattern are shown in Table 1.

Table 1 Flow pattern & drag coefficient with Re [Bearman, 1969]

Reynolds number	Flow pattern	$C_d$	St
$2 \times 10^5$	No bubble	1.14	$\approx 0.2$
$3.7 \times 10^5$	One bubble	0.45	$\approx 0.32$
$4 \times 10^5$	Two bubbles	0.23	0.46

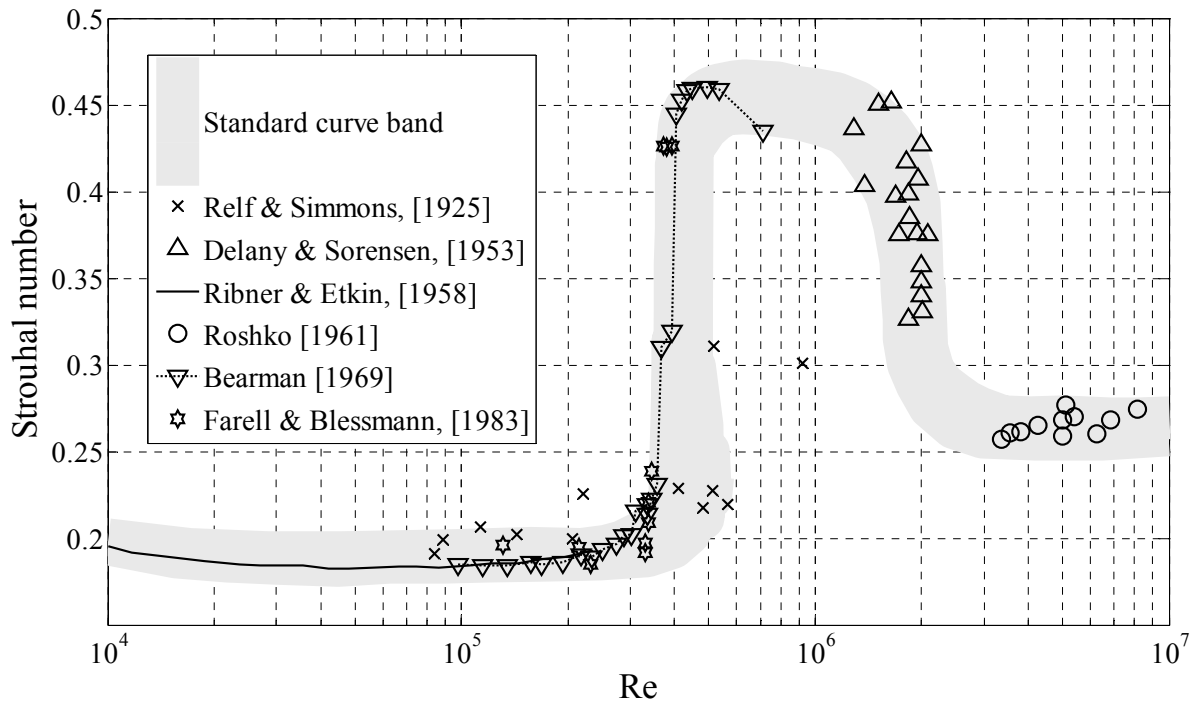


Figure 3 Strouhal number versus Reynolds number

### 2.1.11 Two-bubble ( $3.8 \times 10^5 \sim 4 \times 10^5 < Re < 5 \times 10^5 \sim 10^6$ )

Zdravkovich [1997] mentioned as Re increases, a second bubble is formed associated with another discontinuous drag reduction and jump in the shedding frequency. This regime is complicated by the combination of laminar separation, transition, and turbulent separation of the boundary layers on both sides of the cylinder. Bearman [1969] found that at the two-bubble range of Re the Strouhal number reached a value of 0.46, when the mean drag coefficient reached a minimum value as shown in Table 1.



### **2.1.12 Supercritical ( $5 \times 10^5 \sim 10^6 < Re < 3.4 \times 10^6 \sim 6 \times 10^6$ )**

Irregularly fragmented separation lines prevent periodic eddy shedding. Catalano et al. [2003] investigated numerically the flow over a circular cylinder with Re of  $5 \times 10^5$  to  $10^6$  by using a large-eddy simulation which was made possible by employing a wall model that alleviates the near-wall grid resolution requirements. Although, the solutions were inexact at high Re, they captured the boundary layer separation delay and the reduction in  $C_d$  after the drag crisis. According to their results at a Re value of  $1 \times 10^6$  the drag coefficient has a value of 0.31 and the Strouhal number value is 0.35, which are within a close agreement with the experimental results shown in Figure 1 and Figure 3, respectively.

### **2.1.13 Post-critical ( $Re > 3.4 \times 10^6$ )**

At  $Re \approx 3.4 \times 10^6$  transition in the boundary layer is located somewhere between the stagnation and separation lines. A definite vortex shedding occurs at a Re more than  $3.5 \times 10^6$  as determined by Roshko [1961], through his measurements of the flow characteristics over a circular cylinder with a Re of  $10^6$  to  $10^7$  in a pressurized wind tunnel. Turbulent boundary layers endured more pressure rises causing a shift in the separation to the rear of the cylinder. The drag coefficient increases from  $\approx 0.3$  to  $\approx 0.7$  in the range of  $1 \times 10^6 < Re < 3.5 \times 10^6$  and then becomes constant at high Re value as shown in Figure 1. At Re value of  $3.5 \times 10^6$  a vortex shedding occurs, with Strouhal number value of 0.27 as shown in Figure 3.

## **2.2 Turbulent flow**

Real engineering applications are usually accompanied with different degrees of turbulence that must be considered. In order to gain a better perspective of the freestream turbulence effects, this section provides a review of turbulent flow characteristics past over a circular cylinder in cross flow and its effect on the cylinder drag coefficient. For simplicity the review identified according to Re values as shown in Figure 4.

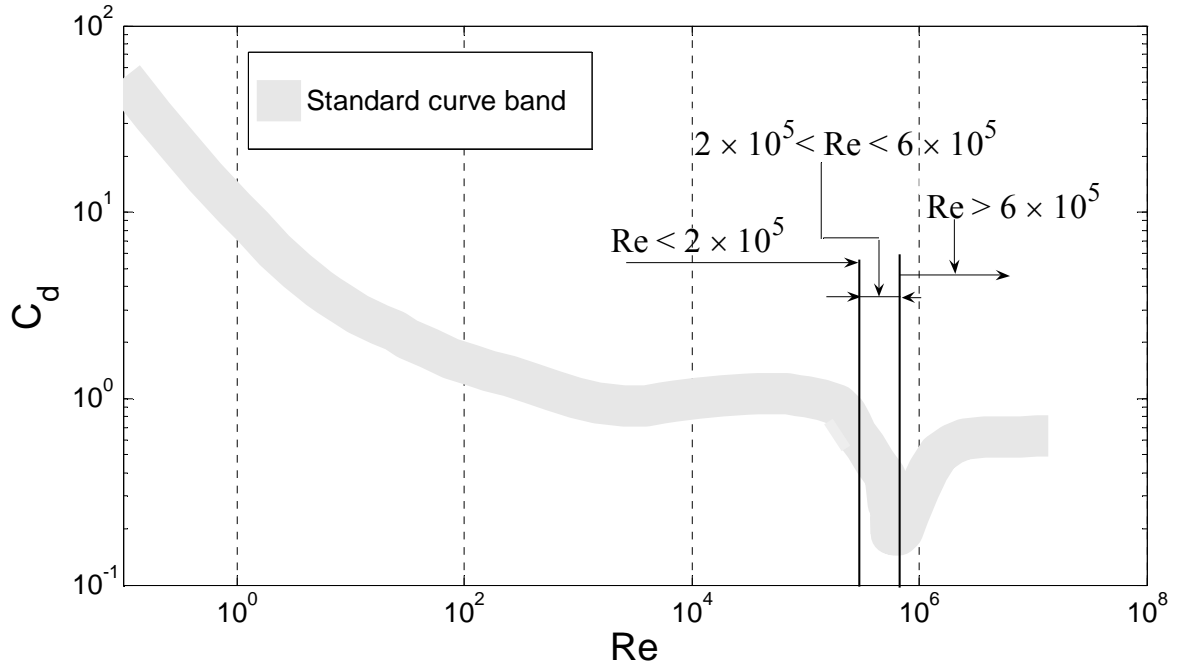


Figure 4 Standard  $C_d$ -Re band

### 2.2.1 $Re < 2 \times 10^5$

Fage and Warsap [1929] studied experimentally the influence of freestream turbulence on the drag coefficient of a circular cylinder ( $D=154.6$  mm and  $60.3$  mm) in cross flow, over a  $Re$  range of  $4 \times 10^4$  to  $2.3 \times 10^5$ . They generated artificial turbulence by using a  $6.35$  mm rope netting with a  $38.1$  mm distance meshing, located at  $968.6$  mm,  $1219.2$  mm, and  $1979.6$  mm upstream from the cylinder, but they did not calculate the turbulence intensity. They found that the shape of the drag coefficient obtained is not altered, but is shifted to the left towards a decreased  $Re$  compared with the standard curve. They concluded that the introduction of turbulence into the freestream makes the flow behave like it has a lower viscosity.

Bearman [1968] Examined a  $17.8$ cm circular cylinder in turbulent flow, with  $Tu=5.5\%$  and  $\Lambda/D=0.5$ . He examined the vortex shedding in the cylinder wake and compared the Strouhal number values with smooth flow for the critical  $Re$  range. As shown in Figure 5, in the sub-critical  $Re$  the Strouhal number agree closely with smooth flow value. However in the critical range the Strouhal number rose with  $Re$  but not to the high values recorded in smooth flow.

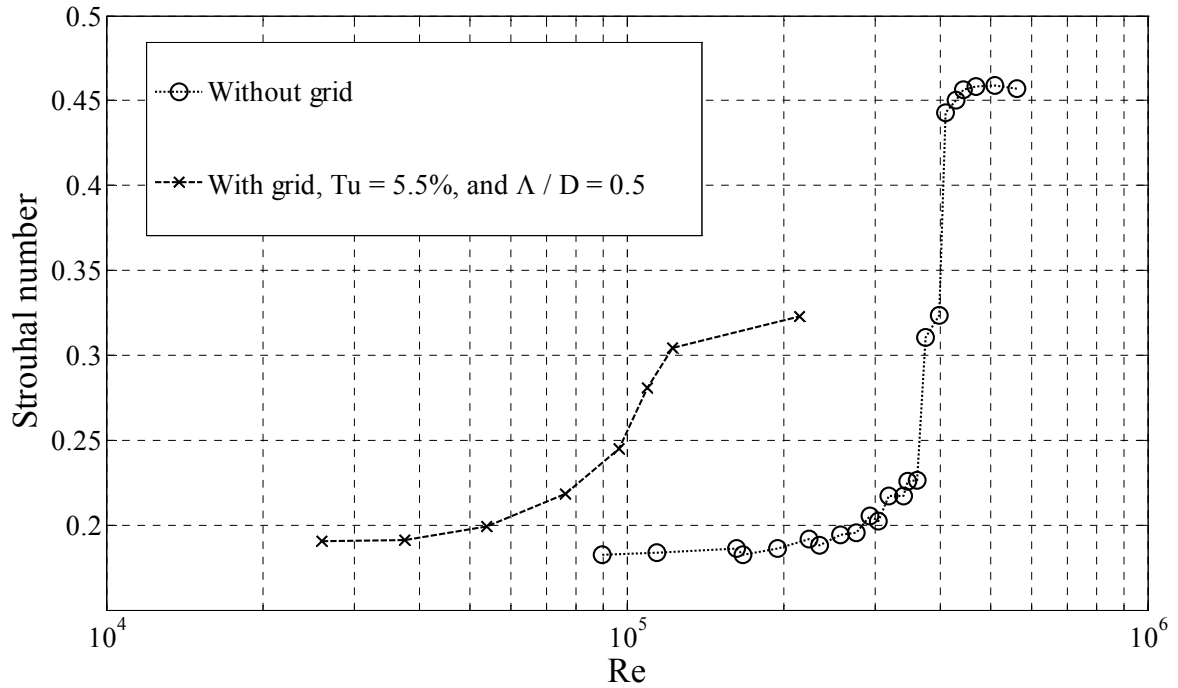


Figure 5 Strouhal number versus Re [Bearman, 1968]

Ko and Graf [1972] investigated experimentally the influence of the freestream turbulence on a circular cylinder in cross flow for a Re range of 1350 to 8000. Turbulence was generated by grids with intensities from 1.2 to 21% and  $\Lambda/D$  range of 0.5 to 3.3. They emphasized that the turbulence does influence the drag coefficient and the standard drag curve should not be employed to find the coefficient in turbulent flows. They mentioned that the turbulence intensity, together with the turbulence scale, must be considered as being associated with the Re to establish the effects of turbulence on cylinder drag coefficient. They concluded that the effect of the scale on the drag coefficient is not as pronounced if contrasted with the turbulence intensity. According to their table, they obtained the lowest drag coefficient at  $Tu = 4\%$ ,  $Re = 4056$  to  $7280$  and  $\Lambda/D \approx 0.97$ , any further increase in  $Tu$  causes  $C_d$  to increase, highest  $C_d$  value observed is 1.25 at  $Tu = 21\%$ ,  $Re = 2680$  to  $5343$  and  $\Lambda/D \approx 1.45$ .

Surry [1972] studied experimentally at Re values of  $3.38 \times 10^4$ ,  $3.54 \times 10^4$ ,  $3.62 \times 10^4$ , and  $4.42 \times 10^4$  the influence of freestream turbulence on flow over a circular cylinder ( $D = 31.5$  mm) with  $Tu$  value equal to 14.7%, 10.5%, 10% and 2.5% associated

with  $\Lambda/D$  values equal to 4.4, 0.36, 4.3, and 9.8, respectively with Re values. According to the results he concluded from the mean drag measurements and Strouhal frequency that to some extent it could be considered that even the large scale turbulence was qualitatively equivalent to an increase in the effective Re. At the examined Re the vortex shedding phenomena from the cylinder is not drastically disrupted by the turbulence intensity (up to 10%), Strouhal number values were 0.2, 0.22, 0.19, and 0.19 respectively with Re values. His drag measurements are shown in Figure 6, when  $Tu = 2.5\%$  and  $\Lambda/D=9.8$  the  $C_d$  value is outside the standard curve band (larger than the smooth flow value). While when  $Tu = 10\%$  and  $\Lambda/D=4.3$  the  $C_d$  still outside the band but is smaller than the first value. At  $Tu = 14.7\%$  and  $\Lambda/D=4.4$  the  $C_d$  value is inside the band. However, when  $Tu = 10.5\%$  and  $\Lambda/D=0.36$  the  $C_d$  value is lower than the smooth flow. His results confirm that when  $\Lambda/D$  decreases the  $C_d$  value decreases and at nearly the same value of  $\Lambda/D$  the drag coefficient decreases when  $Tu$  increases.

Dyban et al. [1974] studied the hydrodynamics of a cylinder ( $D=10$  mm) over a Re range of  $4.6 \times 10^3$  to  $7.5 \times 10^4$ , and a turbulence intensity of 0.5 to 26%. They showed that the freestream turbulence, together with the Re, control the pressure distribution around the cylinder. Increasing turbulence intensity decreases the velocity gradient at the leading surface of the cylinder and by increasing the turbulence intensity from 0.5 to 23% the separation point moves downstream from an angle of  $81^\circ$  to  $88^\circ$ . However they did not consider the effect of  $\Lambda$ .

Savkar et al. [1980] conducted a series of experiments in a small water tunnel over Re range of  $\approx 3 \times 10^4$  to  $\approx 4 \times 10^5$ , a turbulence intensity of 9.5%, various integral scale, and cylinder span. They showed that the drag increases for  $\Lambda/D > 1$  and there was limited evidence for  $\Lambda/D < 1$  effect. They confirmed that an adjustment in the mean pressure distribution and drag reduction was achieved due to freestream turbulence which promotes early transition from laminar to turbulent boundary layer and delay in flow separation. Their drag coefficient as a function of Re for different grid sizes are shown in Figure 7, their results confirmed that at the same value of  $Tu$  (9.5%) the drag coefficient decreases when  $\Lambda/D$  decreases. When  $\Lambda/D$  value is 1.3 (larger than one) the  $C_d$  value

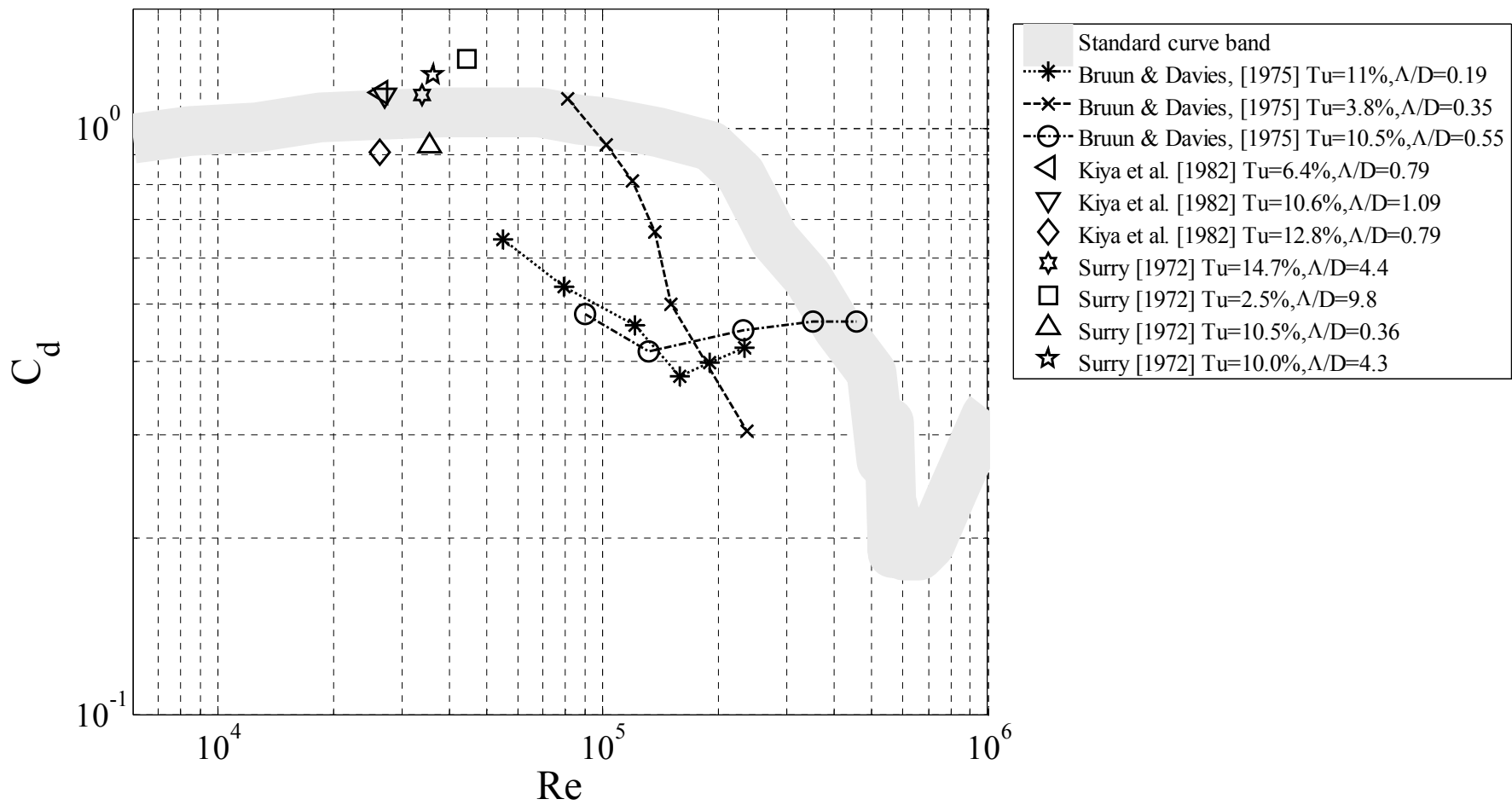


Figure 6 Turbulence intensity and  $\Lambda/D$  effects on  $C_d$ - $Re$  [Bruun & Davies, 1975, Kiya et al., 1982, Surry, 1972]

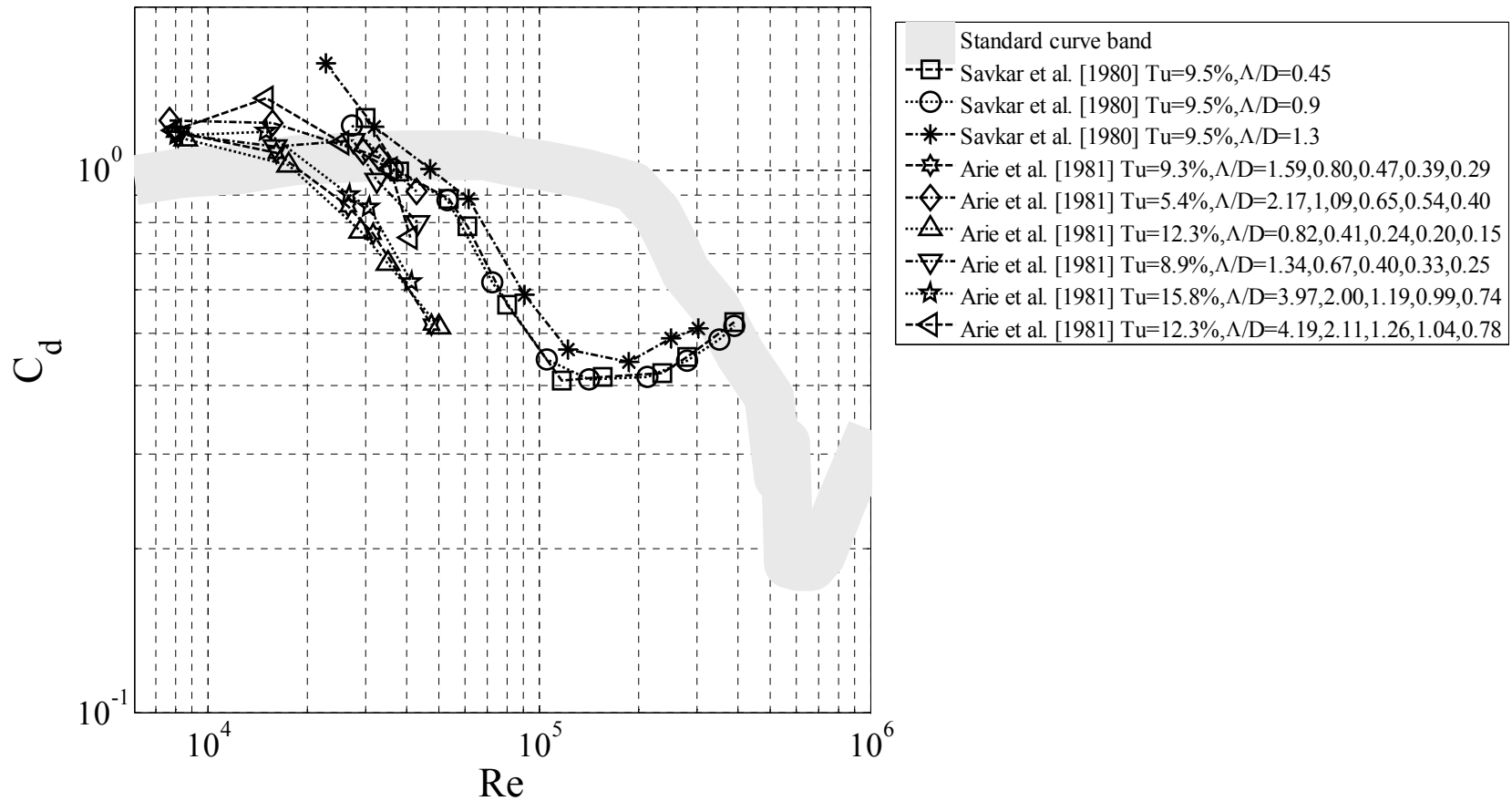


Figure 7 Turbulence intensity and  $\Lambda/D$  effects on  $C_d$ - $Re$  [Savkar et al., 1980, Arie et al., 1981]

\*\* For Arie five different cylinder diameters were used resulting in five values of  $Re$  for the same  $Tu$  and the same  $\Lambda$ , so that five different values of  $\Lambda/D$ , when dividing by five different cylinder diameter.

starts outside the standard curve band (larger than the smooth flow) and this value decreases with the increase of Re (lower than the smooth flow).

Kwok [1986] conducted wind tunnel experiments (including drag measurements) on smooth circular cylinders over a Re range of  $8.3 \times 10^4$  to  $5.5 \times 10^5$ , Tu value of 8.8%, and  $\Lambda/D=0.11$ . His tests were carried out in both smooth flow and in a rod-generated turbulent flow, in particular, small scale turbulence when  $\Lambda/D < 1$ . He concluded that an increase of freestream turbulence intensity promotes an early transition from laminar to turbulent boundary layer associated with a delay in flow separation, which result in a drag reduction. He suggested that only a small turbulence scale, with adequate length, is required to produce a reduction in the drag coefficient.

Arie et al. [1981] studied experimentally the effect of high free-stream turbulence on the flow past a rigid circular cylinder (fabricated from Brass and machined smoothly with  $D=9.55$  mm, 19 mm, 31.8 mm, 38.3 mm, and 50.8 mm) within a Re range of  $7.9 \times 10^3$  to  $5.4 \times 10^4$  and  $\Lambda$  range of 7.9 mm to 40.1 mm. They produced homogeneous turbulence by using square-meshed grids with turbulence intensity between 0.9 to 15.8%. They confirmed the importance of the consideration of the turbulence scales beside the turbulence intensity as they have an equivalent value. They found that drag force acting on the circular cylinder decreases as the turbulence intensity increases and that this drag decreases remarkably as the relative length scale  $\Lambda/D$  value falls below one. Their drag measurements are shown in Figure 7, when  $\Lambda/D > 1$  for all Tu values the drag coefficient values are outside the standard curve band (larger than the smooth flow values), while when the  $\Lambda/D$  decreases, the trend is down towards a lower value of  $C_d$  and the  $C_d$  values reach the minimum when  $\Lambda/D$  falls between 0.25 and 0.78.

Kiya et al. [1982] studied experimentally, in the range of subcritical and critical regimes, the influence of freestream turbulence on the flow past a circular cylinder ( $D$  range from 9.55 mm to 5.03 cm). To produce  $\Lambda/D$  from 0.3 to 3.65 and intensity from 1.4 to 18.5% several grids were used. They confirmed the fall in the drag coefficient measured through the critical regime occurred at a lower Re in turbulent flows, results in a shifted of  $C_d$ -Re to the side of low Re. Their drag measurements are shown in Figure 6, and confirmed that the  $C_d$  decreases when Tu increases at the same value of  $\Lambda/D$  (0.79).

Sadeh and Saharon [1982] investigated the freestream effects on the flow over a smooth circular cylinder (light aluminum alloy with  $D=158.8$  mm) at subcritical  $Re$  in the range of  $5.2 \times 10^4$  to  $2.09 \times 10^5$ . They used polished aluminum rods as turbulence manipulators to generate turbulence of intensity of 2.1 to 4.5% with  $\Lambda/D$  range 0.124 to 0.261. Their results confirmed that the presence of turbulence modifies mean surface pressure distribution characteristics, shift the separation point with a range of 5 to  $50^\circ$  beyond the laminar separation point of  $80^\circ$ , and reduce the drag coefficient in a range of 97 to 46% as compared with the laminar value. The extent of these changes directly related to  $Re$  value and the combination of turbulence parameters.

Mulcahy [1984] measured the steady drag force coefficient of a circular cylinder ( $D=25.4$  mm) located in cross flow in a water tunnel, over a  $Re$  range of  $3 \times 10^4$  to  $2 \times 10^5$ ,  $Tu$  range of 1.5 to 15%, and a  $\Lambda/D$  range of 0.5 to 15%. He concluded that the presence of turbulence reduces the  $Re$  at which the attached boundary layer undergoes a transition from laminar to turbulent flow. Thus, the critical region appears to occur over a larger  $Re$  range, and the associated wake forces are random where they would be periodic in smooth flow. He confirmed that more turbulent flow produces smaller subcritical ranges of  $Re$  (shift the critical range to smaller-up to an order of magnitude-  $Re$ ), and  $Tu$  is much more effective in lowering the critical range than  $\Lambda$  in the  $C_d$ - $Re$  curve.

Norberg [1985] studied experimentally, the influence of freestream turbulence on the flow past a circular cylinder ( $D=41$  mm) over a  $Re$  range of  $2 \times 10^4$  to  $6 \times 10^4$ ,  $Tu$  range of 1.3 to 4.1%, and a  $\Lambda/D$  values of 0.2 and 0.3. He confirmed that the variation in the pressure forces and shedding frequencies are related to the variation in different length scales in the near-wake region. He concluded that the formation distance and the separated shear layer width are important length scales in the near-wake. He concluded that into the pre transition range, the way in which coupled quantities, such as the mean drag coefficient, Strouhal number, and related length scale in the near-wake region are dependent on  $Tu$  and  $Re$  justifies a sub-division of the flow regimes.

Norberg and Sunden [1987] reported that an increase of turbulence intensity from 0.1 to 1.4% altered the launching of the critical regime from  $Re$  value around  $2 \times 10^5$  to about  $1 \times 10^5$ , through their experimental investigation concerning the flow around



circular cylinders in a Re range of  $2 \times 10^4$  to  $3 \times 10^5$ . They confirmed the increase of pressure forces when the freestream has low turbulence intensity in the subcritical regime. They suggested that a physical description of the boundary between the subcritical and the precritical regime could be served from the appearance of a turbulence zone at around  $105^\circ$  from the forward stagnation line.

Yeboah et al. [1997] investigated experimentally the influence of low freestream turbulence intensity ( $< 0.5\%$ ) and  $\Lambda/D$  varied from 0.38 to 2.25 on the mean pressure distribution, shedding frequency, and drag coefficient of a smooth circular cylinder ( $D=6.35$  mm and 25.4 mm) in cross flow at a freestream velocity of 4 to 29.5 m/s, corresponding Re range of  $1.4 \times 10^3$  to  $4.8 \times 10^4$ . They confirmed that for  $\Lambda/D > 1$  and  $Re < 10^4$  the presence of freestream turbulence has no influence on the location of the boundary layer separation, however, the mean pressure coefficients decrease with a slight increase in the drag coefficient, but when  $Re > 10^4$  the mean pressure coefficient are identical to the laminar flow and there is no effect of freestream turbulence conditions. When  $\Lambda/D < 1$  and  $Re < 10^4$  the mean pressure coefficient are higher than the laminar flow and particularly at  $\Lambda/D = 0.56$ , however, when  $Re > 10^4$  the results for all  $\Lambda/D > 1$  are opposite, the mean pressure coefficients are less than the laminar flow and this effect increase with increase Re.

Sanitjai and Goldstein [2001] investigated experimentally the role of free stream turbulence on local mass transfer from a circular cylinder ( $D=50$  mm) for a Re range of  $3 \times 10^4$  to  $8.3 \times 10^4$ , turbulence intensity varied from 0.2 to 23.7%, and with  $\Lambda/D$  range of 0.16 to 1.26. They used two sizes of metal sheet grids and one bar grid. They found that the free stream turbulence powerfully affects the flow around cylinders in a cross flow by reducing the transition Re to a smaller value so that the characteristics of subcritical flow, by means of high freestream turbulence, seems to be comparable to those with a supercritical flow.

Ohya [2004] measured the drag of the circular cylinder ( $D=23$  mm, 30 mm, and 90 mm) with a rotatable drag-measurement facility, which could orient itself perpendicular to the mean wind. His field experiment was with a very large atmospheric  $\Lambda/D$  range of 900 to 3600, when a typhoon occurred near Japan. The turbulence intensity was 17% and

Re range of from  $2 \times 10^4$  to  $2 \times 10^5$ . He found that there is no difference in drag values on a circular cylinder in a highly turbulent atmosphere and those values of the smooth flow in wind tunnel experiments (when  $\Lambda/D$  is very large, turbulence effects on the cylinder drag coefficient disappear).

Increasing the turbulence intensity leads to a decrease in the Re associated with drag coefficient drop in the  $C_d$ -Re curve, everybody agrees on this result. There is also an increase in the  $C_d$  value when  $\Lambda/D > 1$  larger than the smooth flow as shown in Figure 6 and Figure 7. However, there is a common discrepancy in the smooth flow subcritical regime ( $6 \times 10^3 < Re < 2 \times 10^4$ ) of the effect of  $\Lambda$  on the drag of a circular cylinder when the values of  $\Lambda/D < 1$ , many researches agree that the drag coefficient decreases as  $\Lambda/D$  falls below unity, however the percentage of drag change at that Re range for different values of  $\Lambda/D$  associated with different values of Tu are not clear. Therefore, we are here to clarify these discrepancies in the literature, and study the role of turbulent integral length scale, with  $\Lambda/D$  values up to nearly one, associated with constant values of Re and Tu on the cylinder drag coefficient and wake structure.

### 2.2.2 $2 \times 10^5 < Re < 6 \times 10^5$

Bruun and Davies [1975] made measurements for the mean and fluctuating pressure field on a circular cylinder ( $D=0.217\text{m}$ ) for a Re range of  $8 \times 10^4$  to  $6 \times 10^5$ , both for uniform and turbulent flows produced by a grid (two meshes were employed), the longitudinal length scale range of  $0.19D$  to  $0.55D$ . They found that when  $\Lambda/D > 1$  the pressure forces acting on the cylinder frontal area are linearly dependent on the value of the turbulence intensity and the relative length scale unlike the rear part of the cylinder which are independent of the structure of the turbulence of the incoming fluid. Their drag measurements were shown in Figure 6. When there is no grid the  $C_d$ -Re curve follows the standard curve, however, when a grid is introduced the drag coefficient value reduces with certain percentage depends on the grid characteristics and location ( $Tu$ , and  $\Lambda/D$  value). Their measurements in the subcritical regime demonstrated that the amplitude of the pressure fluctuation on the cylinder frontal area was strongly dependent on incoming wind Tu.

Blackburn and Melbourne [1996] examined experimentally the grid-generated turbulence influence on the forces of a circular cylinder for a Re range of  $1 \times 10^5$  to  $5 \times 10^5$  associated with turbulence intensity range of 0.6% to 18% and  $\Lambda/D = 0.5$ . They concluded that turbulence promoted early transition to a supercritical flow and the turbulence length scale is an essential parameter for finding out the fluctuating lift when Re values are high.

### 2.2.3 $Re > 6 \times 10^5$

So and Savkar [1981] experimentally measured steady and unsteady forces induced by a cross flow over a smooth cylinder ( $D=38.1$  mm and  $76.2$  mm) with a range of Re  $2 \times 10^4$  to  $2 \times 10^6$  and a freestream turbulence intensity of 9.5%. They concluded the shift of the smooth flow transition region to a lower Re range as a result of the existence of turbulence.

Cheung and Melbourne [1983] obtained experimental data from force and pressure measurements for diverse levels of turbulence intensity at critical and supercritical regimes ( $7 \times 10^4 < Re < 1 \times 10^6$ ). As shown in Figure 8, they illustrated that increasing Tu causes the minimum pressure, mean and fluctuating drag to decrease in the subcritical regime. On the other hand, opposite influence takes place in the supercritical regime (increasing Tu causes the minimum pressure, mean and fluctuating drag to increase). They confirmed that varying turbulence as well as Re affects the changes in the wake characteristics and the strength of the vortices. As shown in Figure 9, they confirmed that as the Tu increases the Strouhal number increases and reaches a maximum at a lower Re.

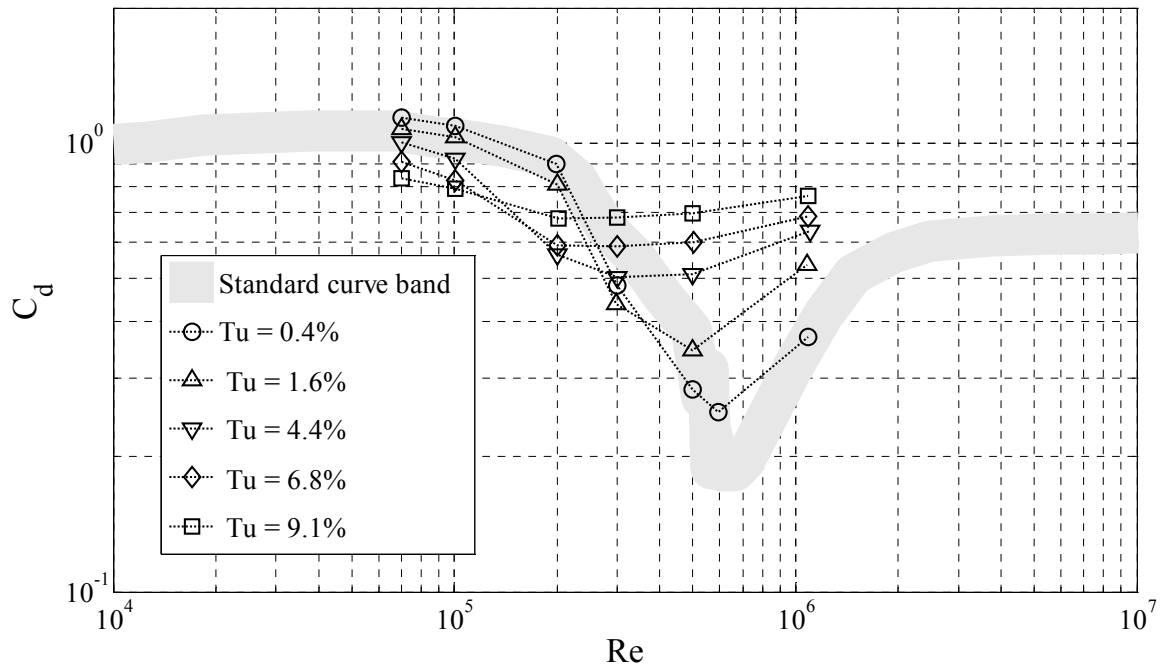


Figure 8  $C_d$ - $Re$  For different turbulence intensities [Cheung & Melbourne, 1983]

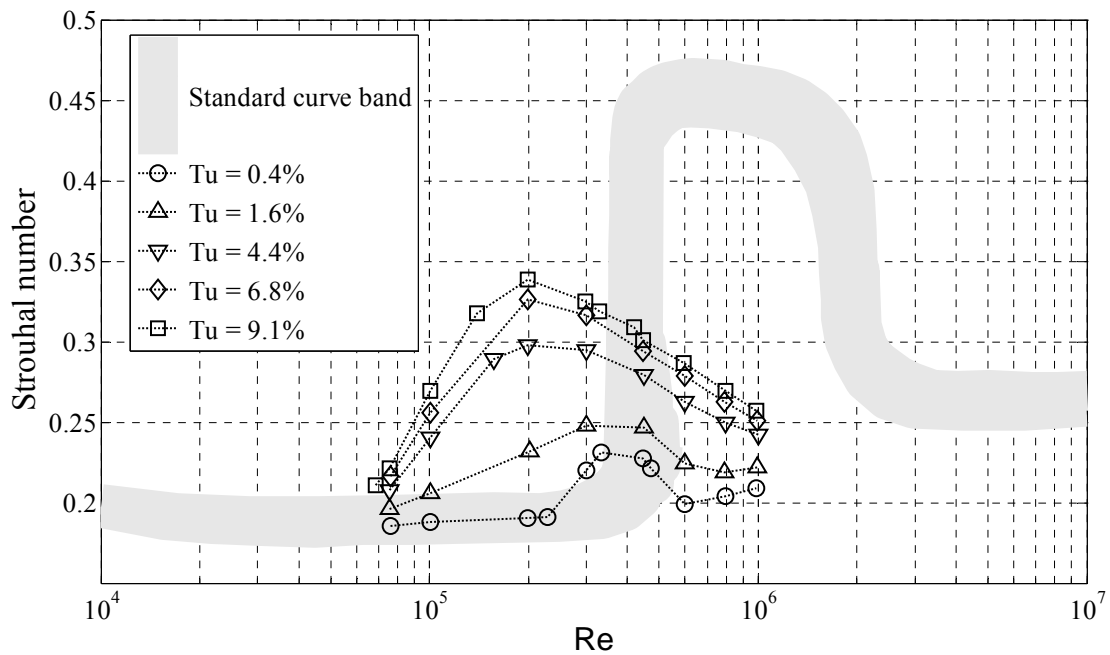


Figure 9  $St$ - $Re$  For different turbulence intensities [Cheung & Melbourne, 1983]

### 2.3 End plate effect

Three-dimensional effects are significant from both a fundamental and practical point of view and should be properly considered. Cross flow tubes and pipes, although they are long, will produce three-dimensional effects. In the practical applications significant effects can come from the three-dimensional behavior. Basically, the mean and fluctuating forces could change and this can cause an important influence on the overall design of the structure and its performance. Cylinders with free ends also present a case of strong three dimensional flows.

Boundary layer build up on the wind tunnel walls could affect the cylinder; mainly the pressure in the base region. Adding properly designed plates at the end of the cylinder make the boundary layer at the cylinder end thin, though it tends to reduce the aspect ratio (cylinder length to cylinder diameter).

Stansby [1974] established the basic requirements for a suitable design for the end plate to obtain a nearly two-dimensional flow. The experiments were conducted with a turbulence intensity of 0.25%, a cylinder diameter of 25.4 mm, and  $Re$  of  $4 \times 10^4$ . He located the end plates at a distance of 51 mm from the wind tunnel roof and floor, to be outside the boundary layers, the center of the end plate coincided with the longitudinal cylinder center. The plate was rectangular with  $4.5D$  between the trailing edge and the cylinder center as shown in Figure 10. He found that the distance between the end plate leading edge and the cylinder center should be sufficiently large to isolate the horseshoe vortex, and yet should be small enough to avoid a substantial boundary layer which may build up on the plate itself. When this distance is equal to  $2.5D$  or  $3.5D$  the base pressure was steady and gave the nearest approach to a two-dimensional flow.

Szepessy [1993] performed an experimental study concerning the effect of the end plate boundaries on the flow past a circular cylinder with  $Re$  range of  $4 \times 10^3$  to  $4.8 \times 10^4$  and cylinder length to diameter ratio of 0.25 to 27.6. He confirmed the strong effects of the end plate design on the base pressure variation along the cylinder span wise, the trailing edge distance has the essential role to obtain as much uniform pressure distribution as possible along the cylinder (should be larger than 3.5 cylinder diameter), also, the leading edge is important (1.5 diameter is enough, however, 2.5 to 3.5 has no negative effects). As a result, he concluded that an optimized end plate design for a

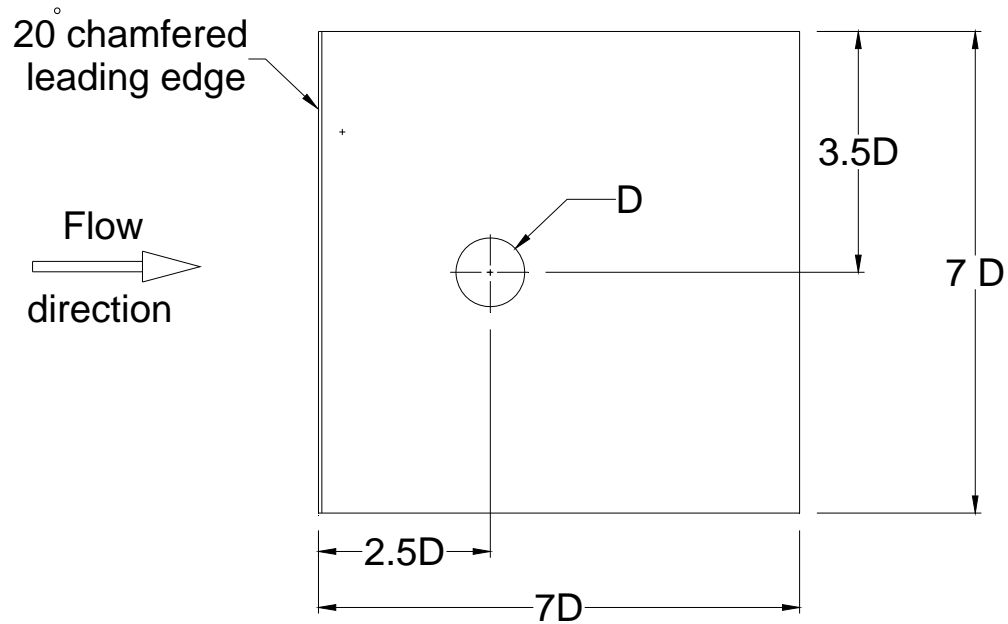


Figure 10 End plate design as recommended by Standby [1974] and confirmed by Fox [1992]

large cylinder to diameter ratio should have a leading distance of 3.5 cylinder diameters, as reported by Stansby [1974], and a trailing edge distance of 4.5  $D$  within his  $Re$  range.

Fox and West [1990] determined the effect of the end plates spacing on the mean pressure, fluctuating lift and drag for a smooth cylinder at a  $Re$  range of  $3.3 \times 10^4$  to  $13.2 \times 10^4$  (subcritical regime), by using the same end plate recommended by Stansby [1974]. They found that when the length of the two-dimensional region is linearly correlated to the aspect ratio, the cylinder aspect ratio fitted between two end plates must be greater than 7 to achieve a region of two-dimensional flow, however, when the ratio is above 30 the need of fitting the end plates vanished. They also confirmed that the interference associated with each plate expands over a distance of  $3.5D$  from the end plate leading edge to confirm the existence of two dimensional flow conditions.

Fox [1992] investigated the interference effects related to the commonly used end plates to simulate a two dimensional circular cylinder (the cylinder infinitely long) at a  $Re$  of  $4.4 \times 10^4$ . His results revealed that the end plate disturbance expands to a distance equal to 3.5 times the cylinder diameter from end plate leading edge. His study confirmed Stansby's [1974] end plate as shown in Figure 10.

Szepessy and Bearman [1992] studied the influence of circular cylinder aspect ratios (cylinder span length to diameter) on the vortex shedding by using moveable end plates with the same end plates designed and optimized by Standby [1974]. The experiments were carried out over a  $Re$  range of  $8 \times 10^3$  to  $1.4 \times 10^5$ ; they determined that an aspect ratio range of 0.25 to 12 do have a great influence on the fluctuating lift. The influence of changing the aspect ratio was found to be dependent strongly on  $Re$ . An 80% increase in fluctuating lift occurred when the aspect ratio was 0.8 at a  $Re$  of  $1.7 \times 10^4$ ; on the contrary, a decrease in the fluctuating lift was found for  $Re < 1.7 \times 10^4$ . Their end plate design is shown in Figure 11.

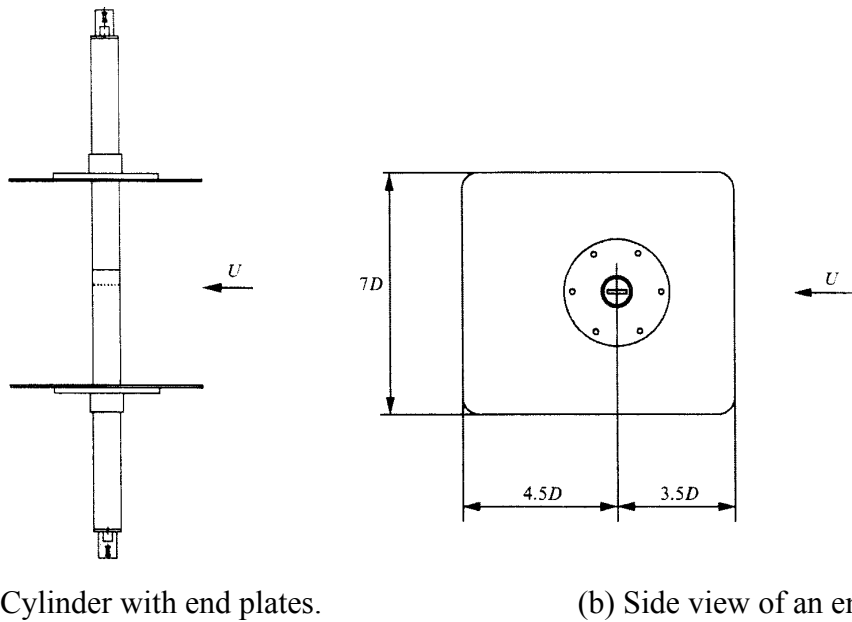


Figure 11 End plate design used by Szepessy and Bearman [1992] (a) Cylinder with end plates (b) Side view of an end plate

For minimizing these effects and to have a flow that is close to two-dimensional a rectangular ( $7D$  by  $8D$ ) end plate is located at  $51$  mm from the left and right wind tunnel walls, with a leading edge distance is  $3.5 D$  and its center coincidence with the wind tunnel midpoint and the cylinder center as well. The aspect ratios for the three cylinders are  $13.5$ ,  $19.5$ , and  $24.5$  so all of them are beyond the minimum critical value of  $7$ , also less than  $30$  which ensure the need of the end plates. For this reason the aspect ratio expected to has a negligible effect on the  $C_d$  measured.

## 2.4 Blockage effect

Richter and Naudascher [1976] investigated the effects of various blockage percentages on the fluctuating lift and drag forces acting on a firmly supported circular cylinder located in a rectangular duct around the critical  $Re$ . Results for different values of blockage ratios were compared to the Wieselsberger [1922] results for very low blockage ratio (unconfined circular cylinder  $B \approx 0$ ). Their results showed that an increasing blockage percentage leads to an increase in the mean drag coefficient, as illustrated in Figure 12, and they confirmed that this increase is undoubtedly a consequence of the lower base pressure which is brought about by higher separation velocities in situations with increasing blockage ratio.

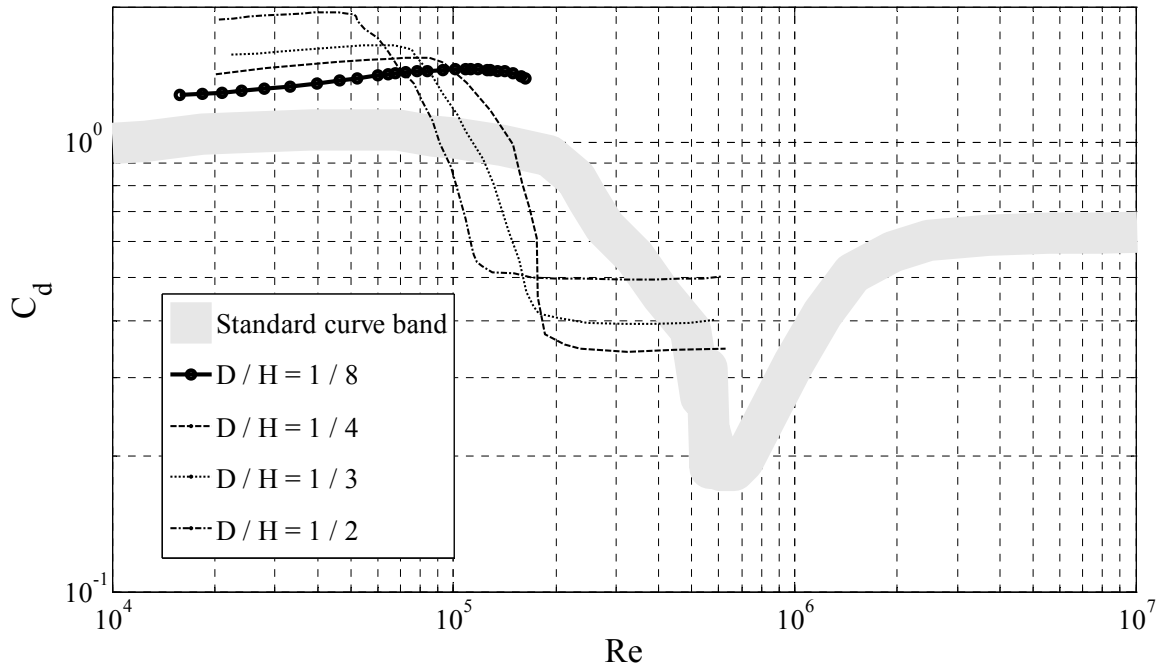


Figure 12 The effect of blockage on  $C_d$ - $Re$  [Richter and Naudascher, 1976]

West and Apelt [1982] conducted an experimental study on a circular cylinder in cross flow with blockage ratios between 2 to 16%, aspect ratios from 4 to 10 and a  $Re$  range of  $10^4$  to  $10^5$ . They concluded that there are no effects on the drag coefficient, pressure distribution, and Strouhal number when the blockage ratio is below 6%. However, there is significant flow distortion when the blockage ratio is above 6% to 16%, the pressure distribution is distinctly different, and the Strouhal number changes with



blockage ratio (as the blockage increased up to 6%, the separation point is moved slightly downstream, however, as the blockage increased between 6 and 9% the separation point shifted rapidly upstream, and remains unchanged as the blockage increased up to 16%). The reduction in aspect ratio and the increase in blockage ratio have similar effects on the drag coefficient and base pressure coefficient.

This study ensured that this parameter is satisfied. The large cylinder diameter used in the experiments has a blockage of 6.06%, therefore, no correction is needed for blockage effects.

## **2.5 Surface roughness effect**

Achenbach [1971] investigated experimentally, the effect of surface roughness on the flow over a circular cylinder ( $D=150$  mm), mainly on the drag coefficient over a Re range of  $4 \times 10^4$  to  $3 \times 10^6$  and Tu of 0.7%. Surface roughness effects on the  $C_d$ -Re curve of a circular cylinder are shown in Figure 13. He divided the  $C_d$ -Re curve from earlier investigations for smooth cylinders to four regimes; the subcritical (up to Re of  $2 \times 10^5$ ), where over a large range of Re the drag coefficient is nearly constant at a value of 1.2. The critical flow regime ( $2 \times 10^5 < \text{Re} < 5 \times 10^5$ ), with increasing Re, the drag coefficient suddenly drops to a lower value. The third regime is the supercritical ( $5 \times 10^5 < \text{Re} < 6 \times 10^6$ ) where the drag coefficient grows up again till nearly a constant value in the transcritical range ( $\text{Re} > 6 \times 10^6$ ). He concluded that increasing the roughness parameters caused a decrease in the critical Re, the subcritical regime is not influenced by the surface roughness, while in the supercritical regime the drag coefficient increases with rising roughness.

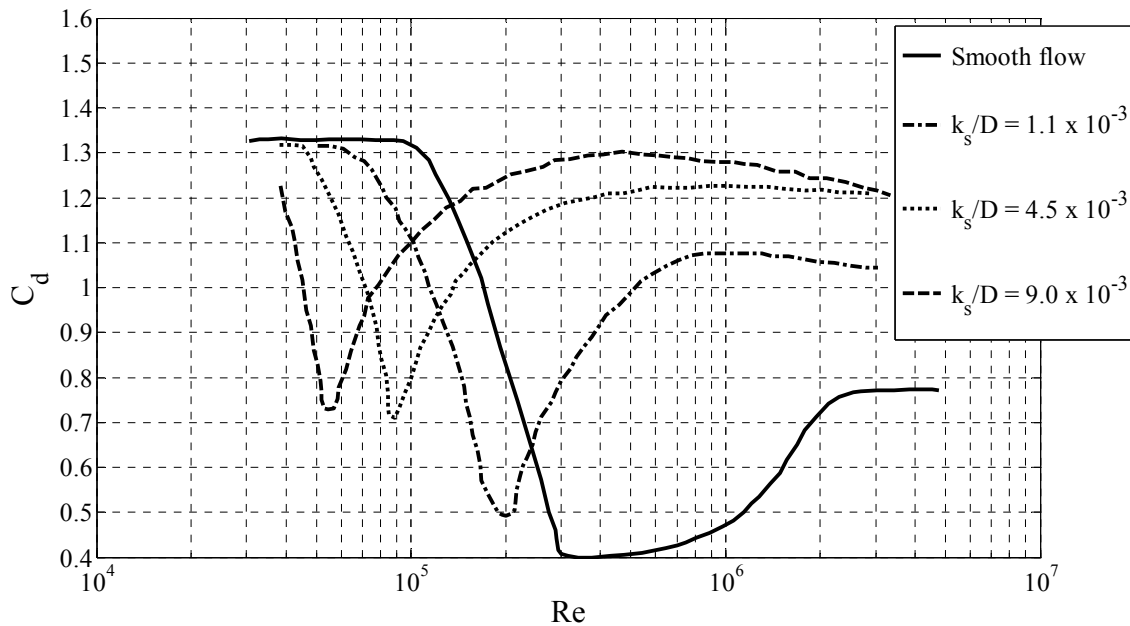


Figure 13 Effect on surface roughness on the drag of a circular cylinder  
 [Achenbach, 1971],  $k_s$  is Nikuradse sand-grain roughness

Guven et al. [1980] described the effects of increasing the surface roughness on the flow characteristics passed a circular cylinder ( $D=270.5$  mm) concerning mean drag coefficient, the mean pressure distribution and the boundary layer development. Five sizes of distributed sandpaper roughness were carefully wrapped around the cylinder (relative roughness which is the average sandpaper particle size to the smooth cylinder diameter range of  $1.59 \times 10^{-3}$  to  $6.21 \times 10^{-3}$ ), over a Re range of  $7 \times 10^4$  to  $5.5 \times 10^5$ . They concluded that there is a significant influence of surface roughness on the mean pressure distribution even at Re value around  $5.5 \times 10^5$ . They confirmed Achenbach's [1971] work that the drag coefficient becomes independent on Re as Re increases instead it shows a definite dependence on the relative roughness. They explained that large surface roughness leads to a thicker boundary layer which separates earlier and is associated with higher drag coefficient.

The relative surface roughness for the three cylinders used in the current experiments is  $1 \times 10^{-5}$ , which is less than the values considered by Achenbach [1971] as rough cylinders, therefore, this parameter is expected to have minimal impact on the  $C_d$ -Re curve.

## **2.6 Moist air density**

The air density can be an important parameter in this study; air density is needed to find the freestream velocity via the Pitot-static tube, to deduce the Reynolds number, and to determine the drag coefficient. For this reason the air density should be determined as accurately as possible and the effect of buoyancy can be negligible. Davis [1992] derived the equation which required input values for the air temperature, pressure, and relative humidity (or dew-point temperature), the equations and the MatLab program are in Appendix A. In addition to these variable parameters, the equation includes a number of parameters which are assumed to be constant. The value of air density for all cases was checked and an accuracy of 0.7% in the calculated density between considering the moist air density than the dry air. Although this accuracy value is small, the equation was employed in this study.

## **CHAPTER 3: Experimental Details**

Available equipment and their limitations are:

1. The wind tunnel dimensions especially the wind tunnel height, which affects the choice of cylinder diameter to avoid the need of the blockage correction factor as mentioned before should be less than 6%. This limits the largest Re value which is detected by the cylinder diameter.
2. In the presence of the perforated plates, the maximum achievable velocity was about 11 m/s.
3. Three orificed perforated plates were available and ready to use.
4. The length of the test section over which the turbulence is nearly isotropic. This is approximately 2m beyond which Tu drops below the desirable level.

### **3.1 Wind tunnel and test model**

The experiments were conducted in a closed-loop wind tunnel with a 4 m long test section as shown in Figure 14. The cross section of this wind tunnel at the entrance is square with dimensions of 0.762m by 0.762m. The cross-sectional area increases gradually downstream to overcome the boundary layer buildup on the wind tunnel ceiling and the floor. Consequently, the dimensions of the end portion of the working section are

(width is 0.762m and height is 0.800m). There is a platform with stairs giving access to the working test section. This platform is on the test section side that has eight service windows, while the other side has only four windows. These windows facilitate adding and removing test instruments within the entire working section. There is one removable support between two adjacent windows to facilitate the handling of the perforated plates. The maximum achievable mean velocity is approximately 20 m/s in the empty working section. The turbulence intensity for the entire velocity range of this wind tunnel is less than 0.5%. Before doing any experiment, a period of two hours is needed to warm up the wind tunnel in order to have stable wind speed.

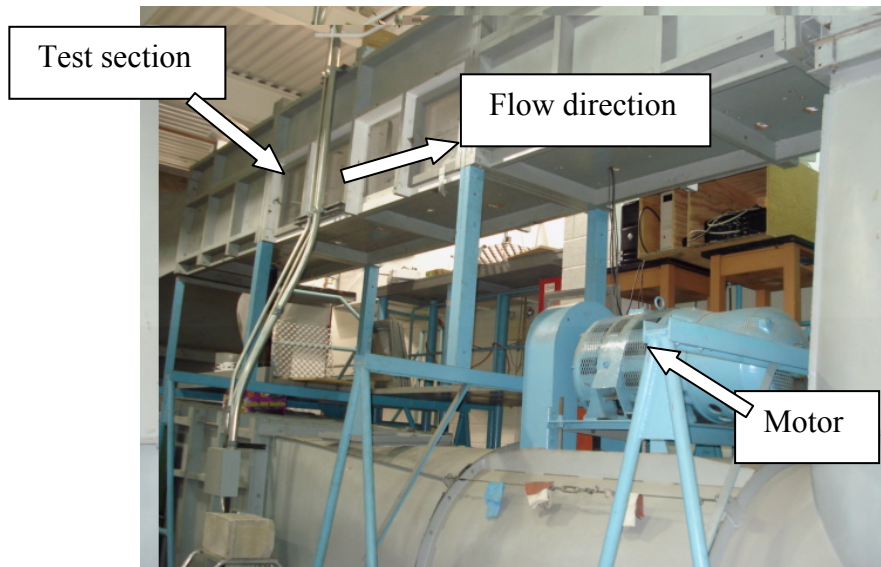


Figure 14 The overall view of the wind tunnel

The freestream velocity in the wind tunnel is measured by a Pitot-static tube, which is connected to a digital manometer (Dwyer series 475 mark III), as illustrated in Figure 15(a); Figure 15(b) illustrates the end plate location relative to the cylinder. Twenty to thirty seconds is needed to allow the manometer to stabilize. In all the conducted experiments the Pitot-static tube was removed after checking the freestream velocity and the small opening in the wind tunnel was closed by using duct tape.

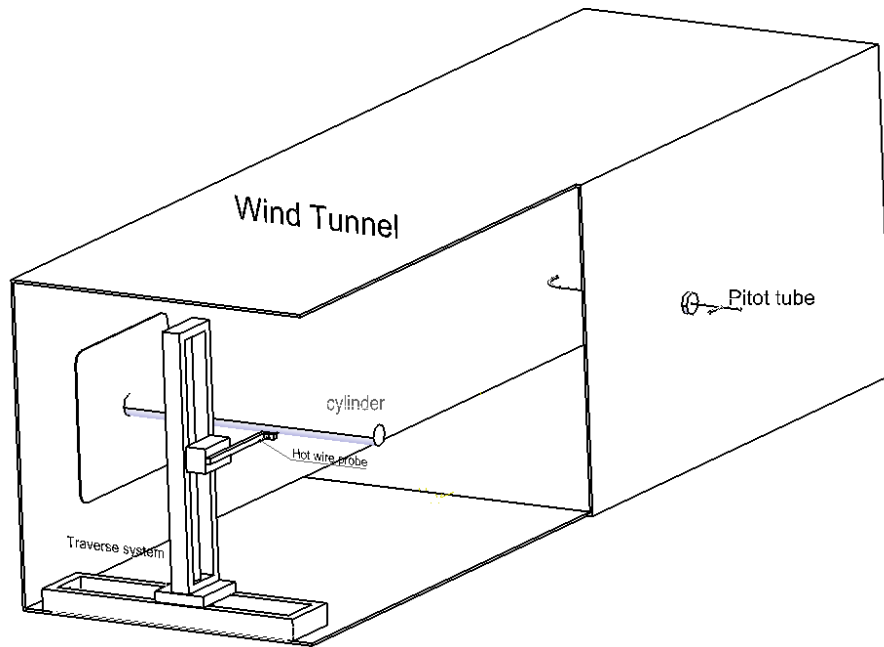
Two facing windows were replaced by two 9.5 mm acrylic plates, with the same window opening dimensions, five holes were made in each plate, the diameter of the hole in the center was 14 mm and its center coincides with the wind tunnel center, while the

diameter of the other 4 holes (2 holes upward and 2 downward of the first hole) were 4 mm as shown in Figure 16. The last holes were used to connect the end plates, the first and last hole were used to connect the end plate related to 48.5 mm and 26.7 mm cylinders, while the second and fourth hole were used to connect the end plate related to 33.6 mm cylinder. The 6 mm shaft attached to the load cell passes the acrylic plate through the hole in the center. These plates were connected to the wind tunnel by 4 screws at the bottom of each plate; however, a transparent tape was used to close the small gap between the other three edges with the wind tunnel. At the same time this tape helped to fix the acrylic plate in place.

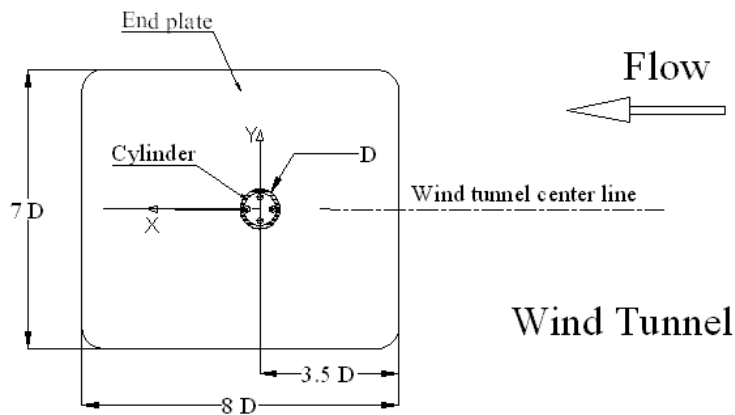
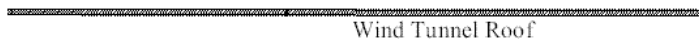
The actual end plate connection assembly with a 48 mm part is shown in Figure 16(a), on the same hand the load cell connection is shown in Figure 16(b). The cylinder was located at the wind tunnel center line by one load cell from one side and one dummy end from the other side; both of them are fixed to the wind tunnel by two (12.5 mm thickness) aluminum angles. A 48 mm length, piece of the same corresponding cylinder size (a spacer) was located between the end plate and the wind tunnel side walls (the acrylic plates) with two 60 mm long screws (the end plates were fixed to the acrylic plates). A countersunk hole for the screw location in the end plate was arranged. At each cylinder end a flange with the same inside cylinder diameter was fitted with a thread in the center, a small aluminum piece with the same thread size was fitted to this flange to connect the cylinder to the shaft attached to each load cell by a set screw. A distance of approximate 1.5 mm was maintained between the end of the cylinder and the end plates. So the load cell is connected to the cylinder through a shaft, an aluminum piece and the flange.

Three cylinders with diameters of 26.7 mm, 33.6 mm, and 48.5 mm fabricated from ABS and subjected to the same level of surface roughness were employed (all the cylinders were sanded and polished). The cylinders surface roughness was tested in the material laboratory of the University of Windsor and the root mean square roughness value was  $3.23 \mu\text{m}$ ; relating this to the smallest cylinder diameter (26.7 mm), the relative roughness was less than 0.0001. This value is significantly smaller than the values ( $1.1 \times 10^{-3}$  to  $9 \times 10^{-3}$ ) considered by Achenbach [1971], as shown previously in Figure 13 for rough cylinders. Moreover, according to the Moody chart this value, together with

the  $Re$  range, indicate that the cylinders can be considered as hydrodynamically smooth cylinders.

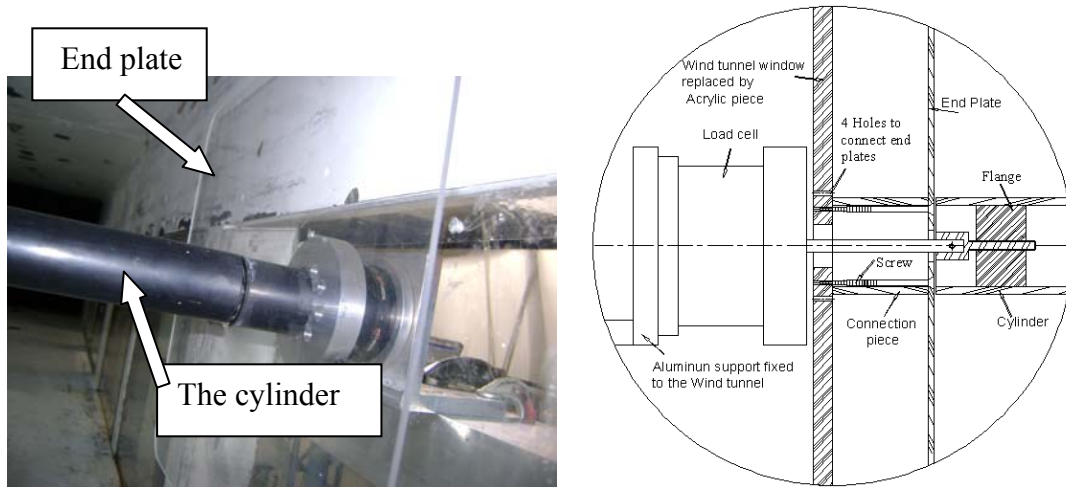


(a) Wind tunnel experiment setup

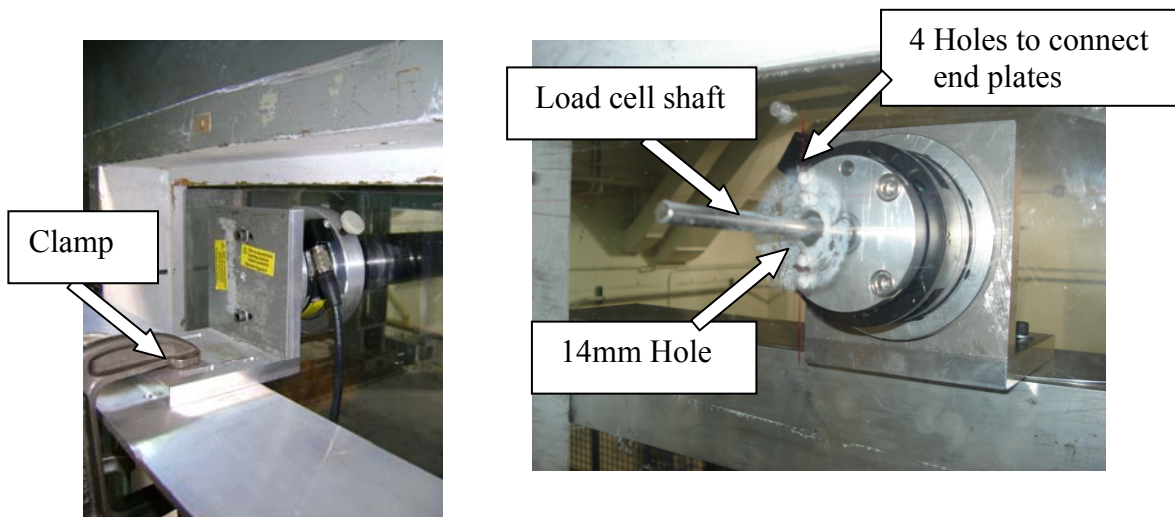


(b) End plate location

Figure 15 Cylinder in cross flow with end plate (a) Wind tunnel experiment setup (b) End plate location



(a) End plate connection assembly with a 48 mm length connection piece



(b) Load cell connection

Figure 16 Actual setup with the end plate in the wind tunnel (a) End plate connection assembly with a 48 mm length connection piece (b) Load cell connection

### **3.2 Hot-wire anemometer**

For flow velocity measurements, a 1D hot-wire probe of DISA type 55p11 was connected to a DANTEC Streamline 55C90 with a constant temperature hot-wire anemometer CTA Module installed within a Dantec 90N10 Frame. It was kept in balance across the Wheatstone bridge diagonal so that the probe resistance, and hence its temperature, was kept constant independent of the cooling from the flowing medium. The bridge output voltage was thus always a function of the effective cooling velocity acting on the probe. The output signal was sent to a desktop computer through a National Instrument ATMIO-16E-10 multifunction data acquisition board with a 12-bit resolution.

The complete measuring system consists of the following:

1. Hot-wire probe 55P11, probe support 55H21, and 4-m BNC probe cable 9055A1863.
2. The Frame including two 55C90 CTA Modules contain a constant temperature anemometer (includes the 1:20 Wheatstone Bridge and the servo loop), and the signal conditioner (includes the Filter and the Gain), together with a calibration Module 90H10, controller, and the power supply.
3. Output BNC cable.
4. Connector box with cable to A/D board.
5. An A/D board (National Instruments) mounted in a computer.
6. Computer.
7. Advanced software application package which include the streamware (hot-wire) and the smart motor software (traverse system).

Appendix B includes the procedure followed for selection of the sampling number and sampling frequency. Appendix C includes the hot-wire probe calibration procedure.

### **3.3 Traversing mechanism**

The 1 D hot-wire probe, together with the temperature probe, were mounted on a light-duty 2-D traversing system, as shown in Figure 17. The horizontal and vertical traverse lengths are 558 mm and 520 mm, respectively. The entire system is supported by a frame made of aluminum sheets. Two servomotors are responsible for the horizontal and vertical motions. The traversing system works as either a fully 2-D system or only as a 1-D system. A computer program related to the hot-wire software was used to control



the traverse system movement in an array of x rows and y columns together with the period needed to collect the required data and the movement time from one point to another.

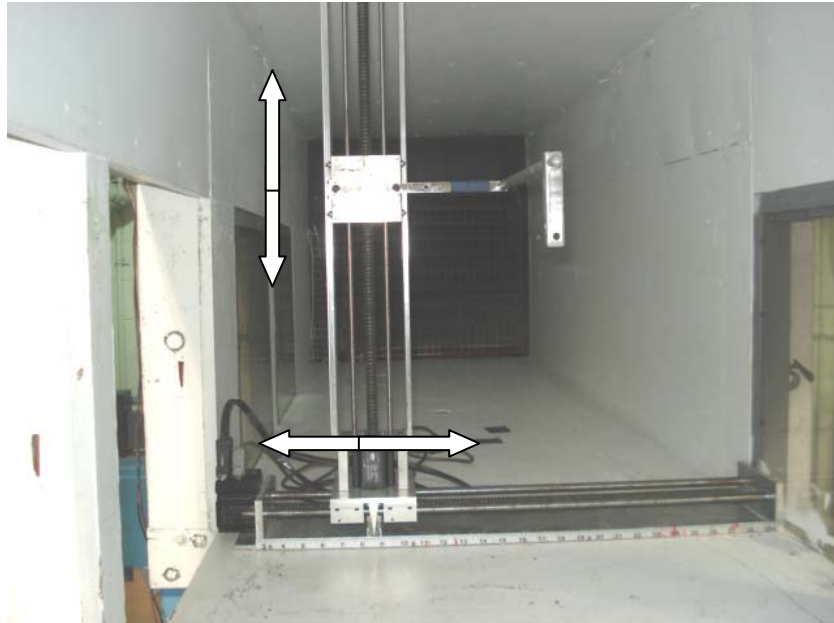


Figure 17 The light-duty 2-D traversing mechanism

### 3.4 Load cell

A six-axis force/torque sensor system made by ATI Industrial Automation including F/T data acquisition (DAQ) and F/T transducer, Gamma version SI-32-2.5, with a maximum load of 32N was employed as shown in Figure 18. The reading from this load cell was multiplied by two to give the total load on the cylinder. The compact, rugged, and monolithic structure transducer converts force and torque into analog strain signals (three force/torque values were stored in the same file). The transducer was connected to the interface power supply box through a separate high-flex life transducer cable which was electrically shielded to protect transmission from power supply box. The interface power box supplies power to the transducer and electronics as well as conditioning the transducer signals to be used with a data acquisition system. The power supply interface box connected to the National Instruments data acquisition hardware by a robust power supply cable through a connector on the data acquisition end. The data acquisition system

converts the transducer signals from analog voltage into data that can be identified by the ATI Industrial Automation CD installed in the computer.

To have a better alignment, the load cell was attached with a shaft, while the other dummy end was attached with a ball and socket. Extreme care was taken to check that the rod connecting the load cell to the cylinder was not touching the end plate/wind tunnel wall openings.

After installing all the parts, the load cell was aligned horizontally and vertically. The load cell was connected to the angle by a clamp while the other dummy end was connected by normal bolts.

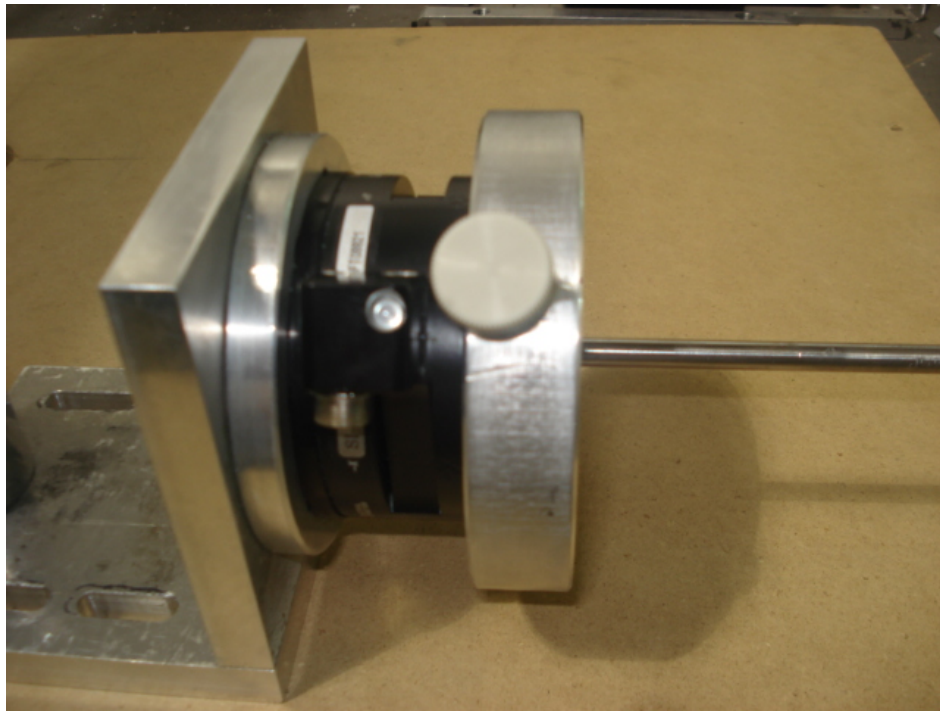


Figure 18 Load cell attached to the aluminum angle

To check the load cell manufacturer calibration and the reading from only one load cell was accurate (not for recalibrating the load cell), a weight was placed at the center of the cylinder vertically, only half of the weight was recorded by the load cell (y direction - lift value). To further ensure that the load measurement setup is viable, this weight relocated to around 1-2 mm from the cylinder end toward the load cell, in this case the load cell read full load, however it read zero when relocating the load at the other end of

the cylinder. For the drag value the same procedure was repeated (x direction –drag value), as shown in Figure 19. Three weights were checked (25g, 50g, and 100g) for both lift and drag values. The results were consistent with the manufacturer data sheet.

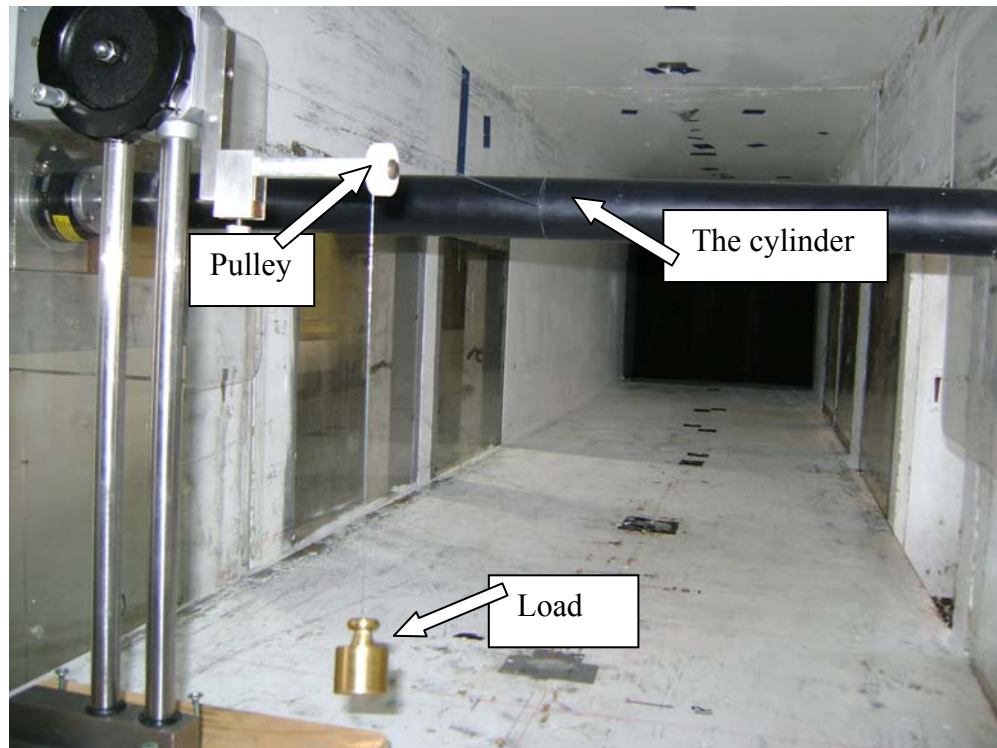
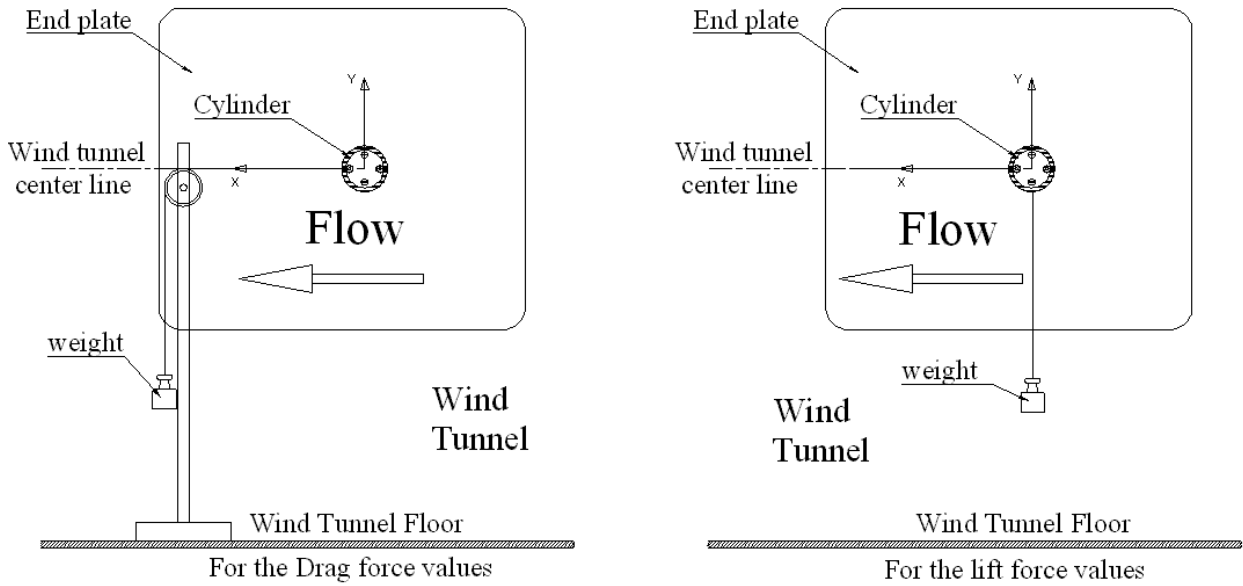
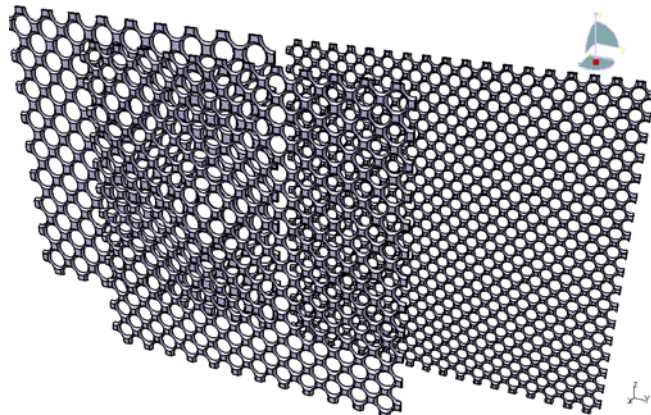


Figure 19 Load cell, calibration check

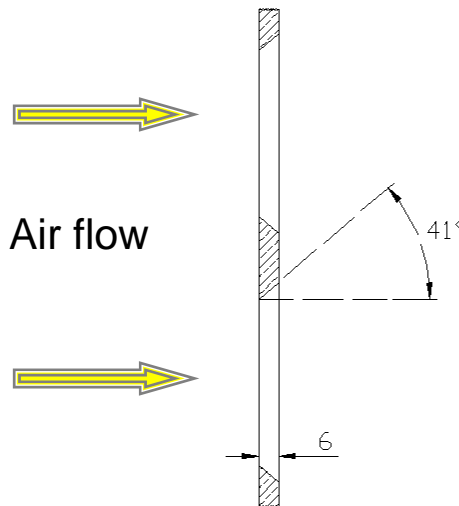
### 3.5 Orificed perforated plates

The turbulence is generated by inserting one of the three orificed perforated plates in the wind tunnel; see Figure 20(a). The thickness of these aluminum plates is 6 mm with hole diameters of  $d = 25$  mm, 37.5 mm, and 50 mm, respectively. The three perforated plates have the same solidity ratio of 43%. All holes were machined into an orifice with a  $41^\circ$  angle through the whole thickness; see Figure 20(b). Liu et al. [2007] showed that a quasi-isotropic turbulence is generated when using these orificed perforated plates. To make it easy to identify the plates it is favorable to number them as d25, d37.5, and d50, respectively.

(a) d25, d37.5, and d50



(b) Looking upstream to the plates



(c) Cross section of the plate

Figure 20 The orificed perforated plates (a) d25, d37.5, and d50 (b) Looking upstream to the plate (c) Cross section of the plate

### 3.6 End plate design

The end plate dimensions are  $7D$  by  $8D$  according to the design suggested by Szepessy [1993] as shown in Figure 21. The leading edge is chamfered  $20^\circ$  according to Fox [1992]; the distance between the leading edge and the center of the cylinder is  $3.5 D$  and between the trailing edge and the cylinder center is  $4.5 D$ . The end plate was located at a distance of  $51 \text{ mm}$  from the tunnel wall according to Stansby [1974], the center of the end plates together with the cylinder center were coincidental with the vertical midpoint of the wind tunnel left and right walls. The end plate was made of acrylic and all the edges were smoothed by fine sand paper

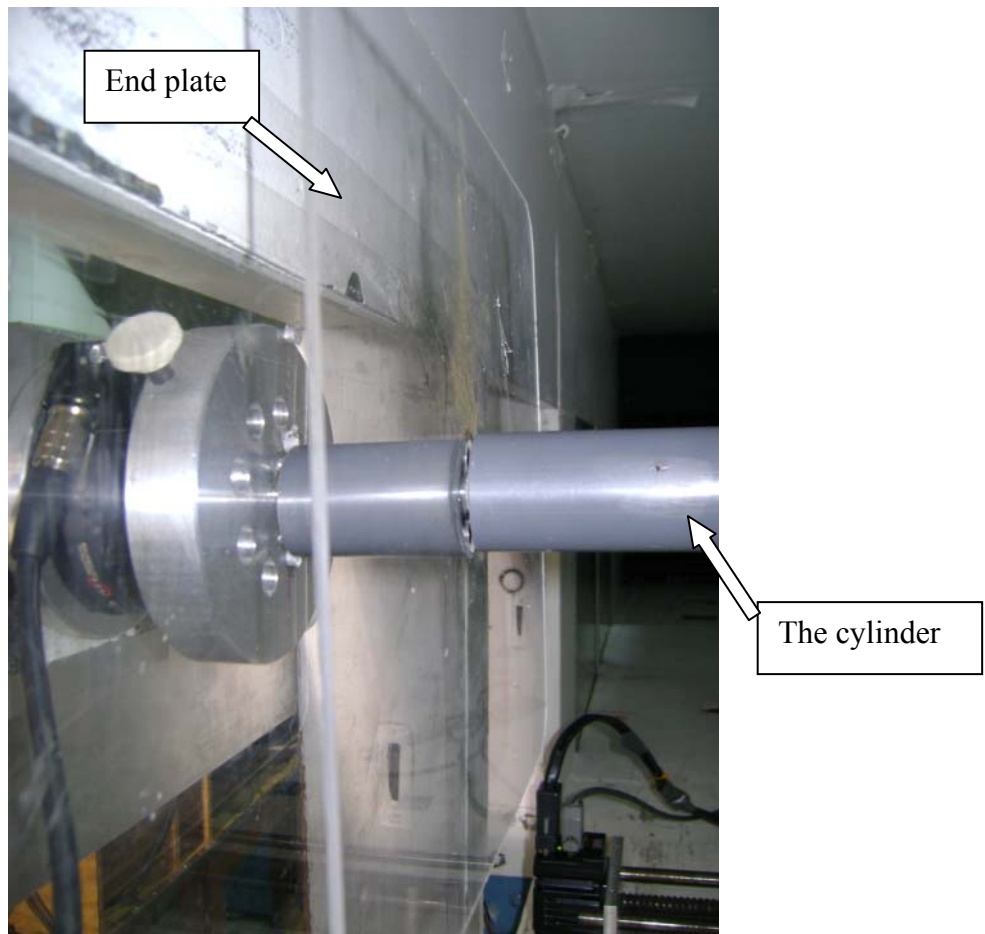


Figure 21 End plate

## CHAPTER 4 Data Analysis

### 4.1 Hot-wire data analysis

The Dantec hot-wire provided voltage values which could be converted to flow velocities according to the calibration data. All flow characteristics could be found from corresponding flow velocities which were stored in the computer that was connected with the CTA, by transferring the files of all measuring points to the MatLab program. The value of the time-averaged velocity ( $\bar{U}$ ) was calculated by using

$$\bar{U} = \sum_{i=1}^N \frac{U_i}{N} \quad (4)$$

where,  $U_i$  is the instantaneous velocity (m/s),  $N$  is the sample size.  $N$  is equal to  $10^7$  with a sampling frequency of 80 kHz in this experiment.

The difference between the instantaneous velocity and the time-averaged velocity is the instantaneous fluctuating ( $u$ ) value. The root mean square value for the velocity at any location was deduced via

$$u_{\text{rms}} = \sqrt{\sum_{i=1}^N \frac{(U_i - \bar{U})^2}{N-1}} \quad (5)$$

The relative turbulence intensity,

$$Tu = \frac{u_{\text{rms}}}{\bar{U}} \times 100\% \quad (6)$$

The integral length scale represents the scale of the energy containing eddies. The magnitude of integral length scale is largely dependent on the dimensions of the size of the holes and the spacing between them in each perforated plate. It is evaluated from the area under the curve of the correlation function of the fluctuation velocity ( $u$ ) value in the stream wise direction.

The integral time scale for discrete samples was found by using,

$$\tau_{\Lambda} = \frac{\frac{1}{N-M} \sum_{i=1}^{N-M} (u_i \times u_{i+m})}{\frac{1}{N} \sum_{i=1}^N u_i^2} \quad (7)$$

Here  $M$  varies from 0 to  $N-1$ .

The integral length scale was found by multiplying the integral time scale by the time averaged velocity

$$\Lambda = \bar{U} \times \tau_{\Lambda} \quad (8)$$

The autocorrelation between the instantaneous velocities fluctuations were plotted, the autocorrelation started at a value of 1 and became zero when it hit the x axis (the MatLab program stopped when the autocorrelation first reached a zero value) as shown in Figure 22. The integral length scale value represents the area under the autocorrelation function. Different numbers of iterations for the autocorrelation were obtained from one location to another and from one velocity to another.

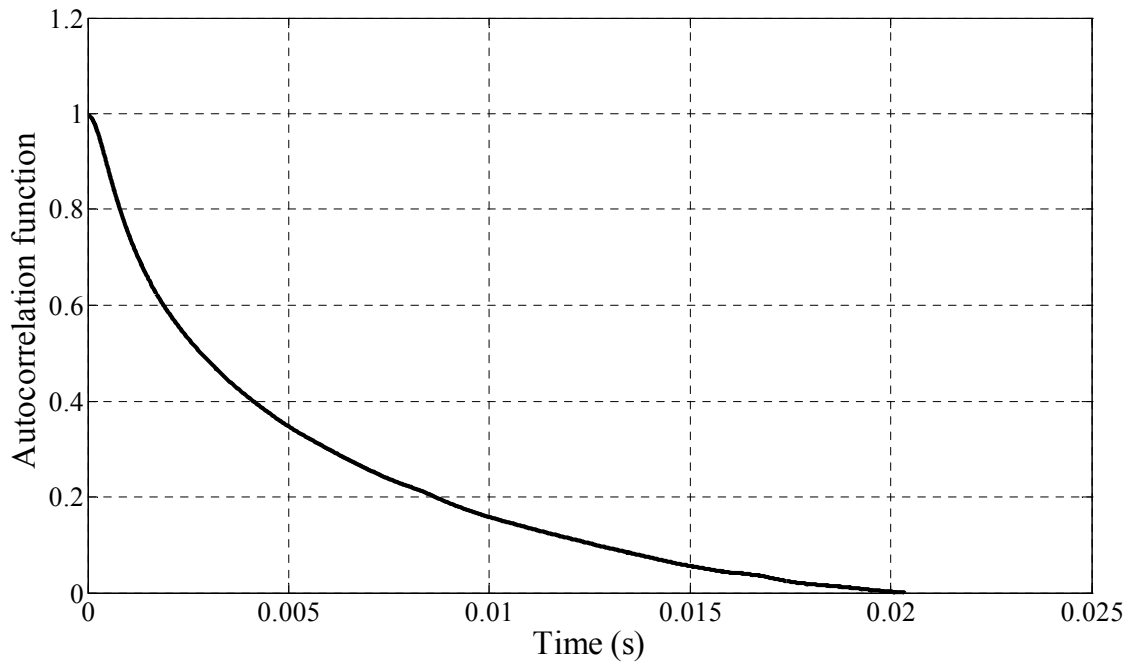


Figure 22 Integral length scale for d37.5 plate @ 20 x/d and  $U_0 = 5.51$  m/s

## 4.2 Drag coefficient

The load cell calibration was done by the company and the calibration accuracy report was available. To initialize the load cell reading the bias button was pressed every time the wind tunnel was switched on or off (the zero value was reset).

The drag force coefficient was calculated using the following equation:

$$C_d = \frac{2 \times F_d}{\rho \times U_0^2 \times A} \quad (9)$$

Here  $\rho = 1.2 \text{ kg/m}^3$  for standard air at  $20^\circ \text{C}$  and  $101325 \text{ Pa}$ . This density was calculated according to air atmospheric pressure, temperature and relative humidity every time before any experiment. The frontal area of the cylinder,

$$A = 0.654 \times 0.485 = 0.03178 \text{ m}^2 \text{ for cylinder with 48.5 mm diameter.}$$

$$A = 0.654 \times 0.336 = 0.02197 \text{ m}^2 \text{ for cylinder with 33.6 mm diameter.}$$

$$A = 0.654 \times 0.267 = 0.01746 \text{ m}^2 \text{ for cylinder with 26.7 mm diameter.}$$

As the matter concerning the frontal area calculations for the three cylinders the length of the cylinder considered only and the length of the dummy piece with the end plate was disregarded. For all experiments a few minutes were required to stabilize the wind tunnel, after that 10000 load cell data were recorded at a sampling frequency of 1 kHz, resulting in a 10s data recording period. Figure 23 shows that a sample of approximately 9000 was adequate for deducing the time-averaged drag. A sample size of 10000 was chosen. The MatLab program used to calculate Fast Fourier Transform (FFT) along with a sample load cell FFT plot are given in Appendix D.

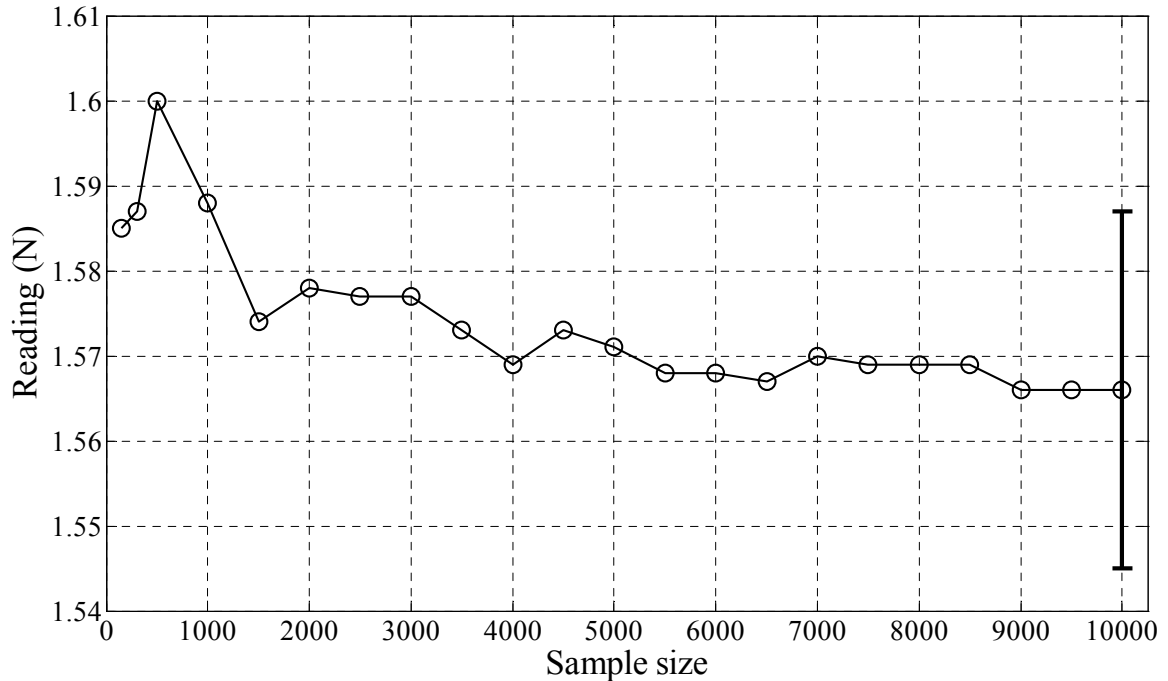


Figure 23 Load cell sample size check, 26.7 mm cylinder,  $Tu=5\%$ , and  $U_0=10.7 \text{ m/s}$

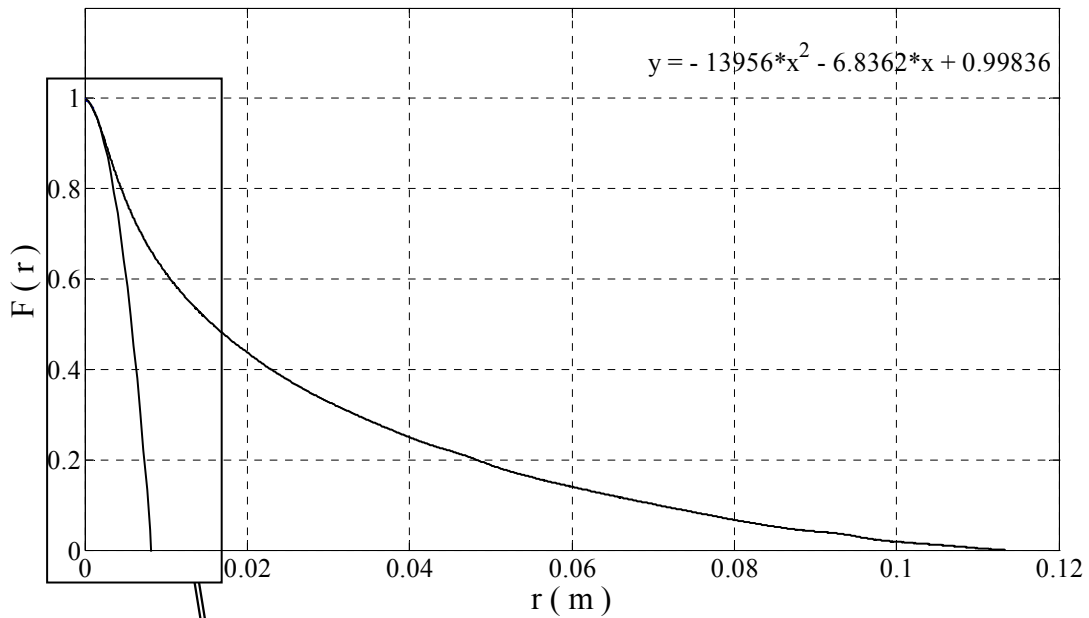


### 4.3 Taylor microscale procedure

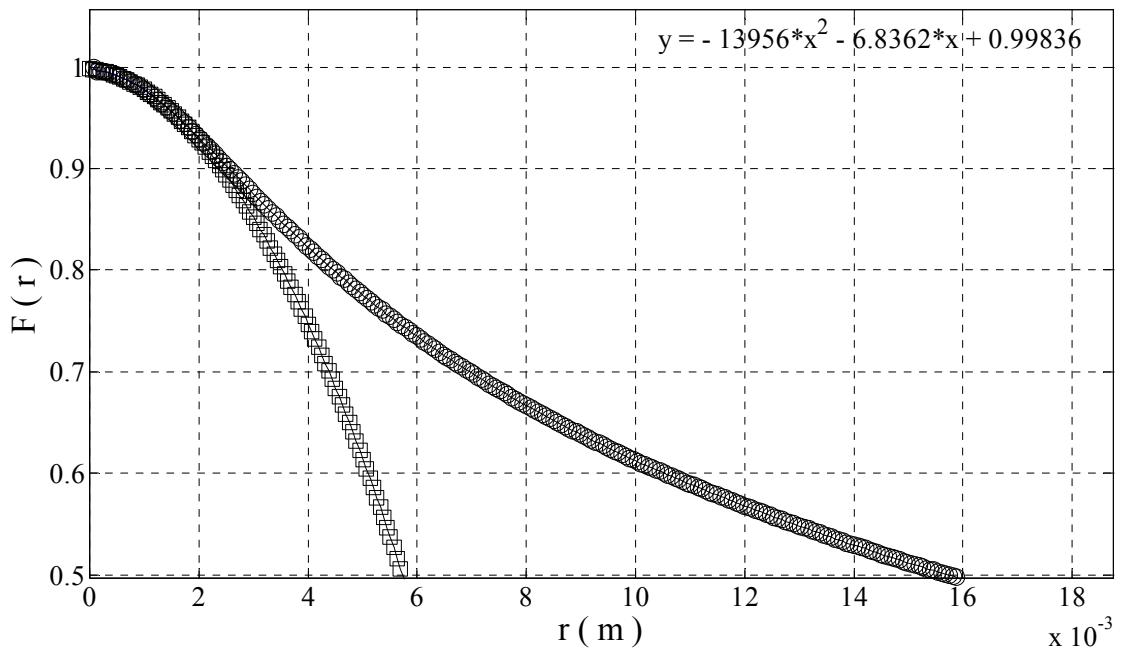
A second characteristic length scale associated with turbulence flow is the Taylor microscale (characteristic of the mean spatial extension of the velocity gradient). This Taylor microscale is always much smaller than the integral length scale (small-scale structure of turbulence tends to be approximately isentropic at large  $Re$ ). Tennekes and Lumley [1972] mentioned that the Taylor microscale is also associated with the curvature of spatial velocity autocorrelation, since the small-scale structure of turbulence at large  $Re$  is always approximately isotropic. The microscale can thus be deduced from the intercept of the parabola that matches the autocorrelation at the origin.

For each autocorrelation curve, the x axis (time) is converted to length by multiplying this axis by the freestream velocity. The best parabola that fits the first three autocorrelation points was plotted on the same curve. The intersection point of this parabola with the x axis is the value of Taylor microscale over the square root of 2 as mentioned by Davidson [2004]. The objective was to find the number of points in addition to the first three, which can provide the best fit for the parabola. A MatLab program was produced to calculate the minimum number of point required to have a parabola curve fit facing downward for each condition. The curve fitting was examined individually; Figure 24(a) shows a typical case for d25 plate curve by zooming in the contact between the autocorrelation and the parabola, such as that shown in Figure 24(b). If a three-point fit led to an upward facing parabola, additional point(s) was employed in the curve fitting until the parabola faced downward and the fitting was good physically. The number of points that required a nearly optimum intersection between the parabola and the autocorrelation was found to be equal to one and a half of the minimum points plus one (in other words, the number of points that was considered, is equal to the multiplication of the minimum number of points by one and a half plus one more point). This number of points was applied for the other two plates (all cases). A total of 120 curves associated with 120 parabola equations were obtained, all the equations were solved to find the value for the Taylor microscale. Liu et al. [2007] mentioned that for their range of plate locations (similar to the current study) the estimated value of the Taylor microscale was approximately 2 mm to 7 mm for d37.5 plate and at a velocity equal to 10.5 m/s, which was similar to the results obtained in the current study. The

somewhat different Taylor microscale estimation procedure used by Liu et al. [2007] is given in Appendix E.



(a) Taylor microscale

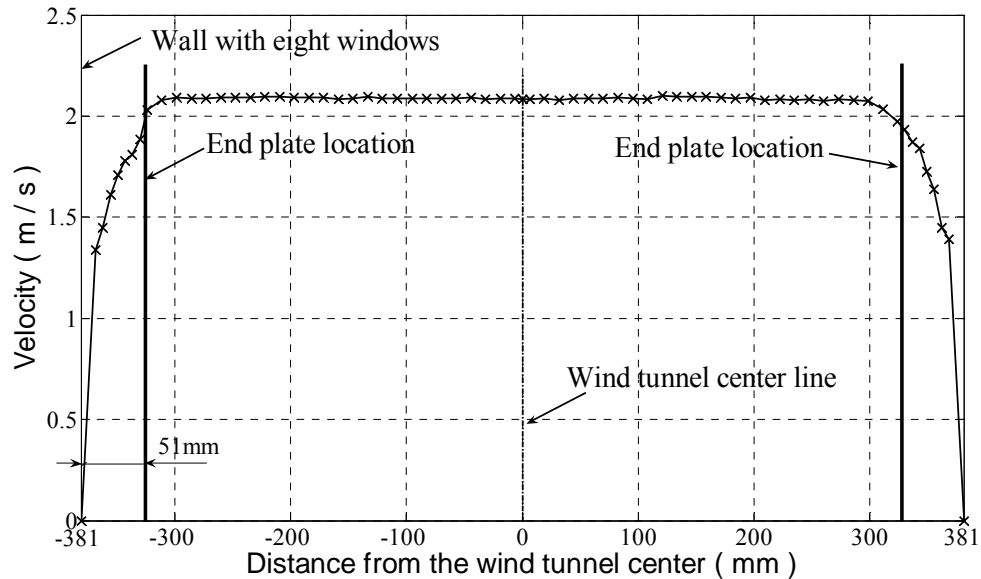


(b) Zoom in the contact between the autocorrelation and the parabola

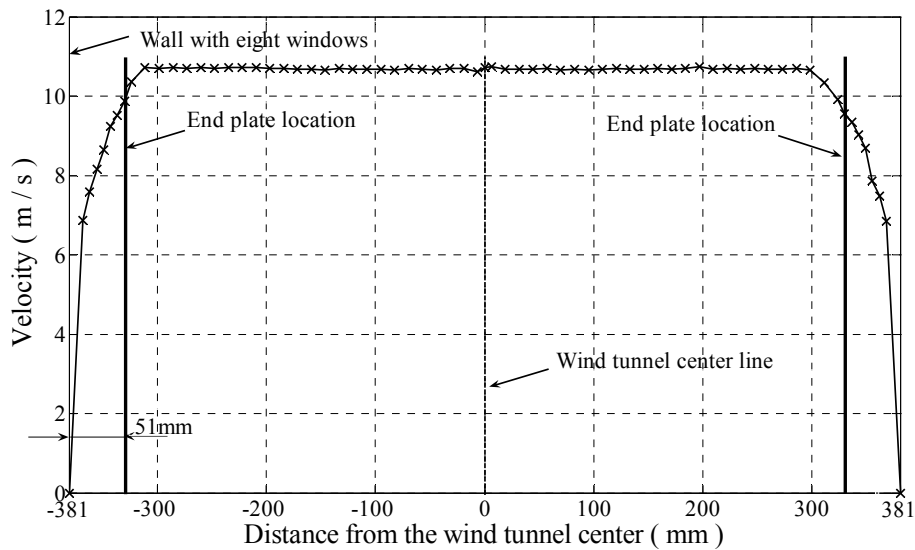
Figure 24 Taylor microscale for  $d37.5$  plate @  $20 \times/d$  and  $U_0 = 5.51$  m/s (a) Taylor microscale (b) Zoom in the contact between the autocorrelation and the parabola

#### 4.4 Boundary layer effect

To minimize the boundary layer effect, end plates were used. For this reason the boundary layer thickness from the left and right walls were checked. Figure 25 shows that the boundary layer was around 8 cm, over the range of velocity considered. Placing the end plates 51 mm from the walls led to roughly 10% reduction in the velocity near the ends, over a cylinder span of less than 8%.



(a)  $U_0 = 2.1$  m/s



(b)  $U_0 = 10.7$  m/s

Figure 25 Wind tunnel boundary layer check (a)  $U_0 = 2.1$  m/s (b)  $U_0 = 10.7$  m/s

#### 4.5 End plate effects on $C_d$

The drag forces with and without the end plates were deduced over the range of  $Re$  studied. To determine the effect of the presence of the end plates, a similar 48 mm long piece that was used with the end plate (to locate the end plate 51mm from the wind tunnel walls) and a disc from the same end plate material, thickness, and with identical holes were fabricated. The disc was glued to the piece to act like a dummy end as shown in Figure 26. As soon as the experiment with the end plates was done, the end plates were removed and these dummy pieces were placed on both sides, and the drag coefficient were measured and plotted. Figure 27 clearly depicts that  $C_d$  is reduced in the absence of end plates. The drag coefficient is higher with end plate case for the range of  $Re$  under consideration. By adding the end plates to the cylinder the wind tunnel boundary layer is minimized and the flow passing the cylinder was nearly two dimensional, also the 3.5D distance from the leading edge minimized the interference of the end plate itself with the cylinder. This result is consistent with those obtained by Stansby [1974] and Fox [1992] who confirmed the recovery of some drag in the presence of the end plate. The end plates utilized here have the same dimensions (based on the cylinder diameter) over a range of aspect ratios (above 7 and below 30), the aspect ratios concerned in this study (13.5, 19.5, and 24.6) were within this range.

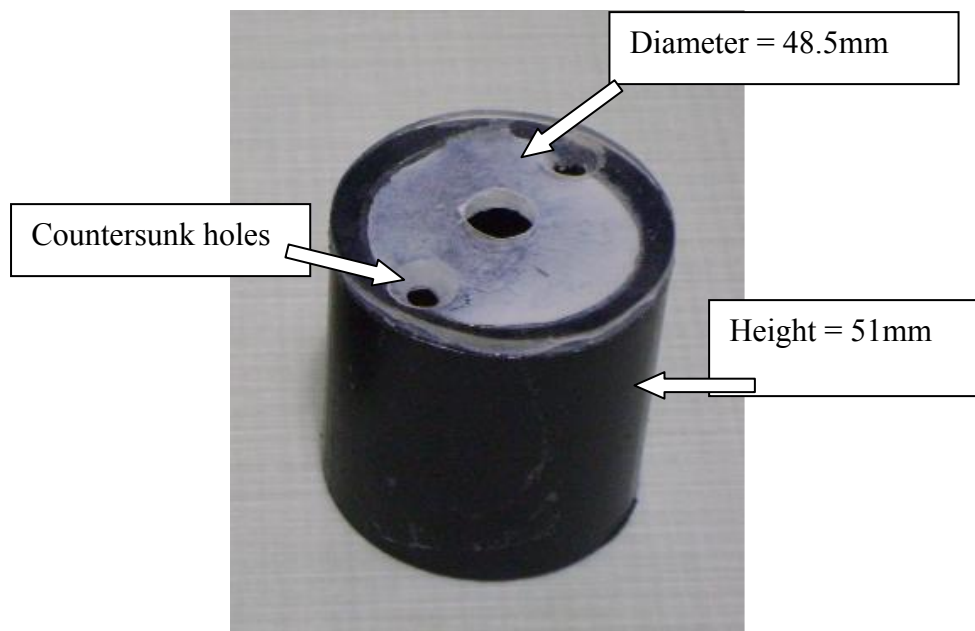


Figure 26 Dummy piece to check the effect of end plate

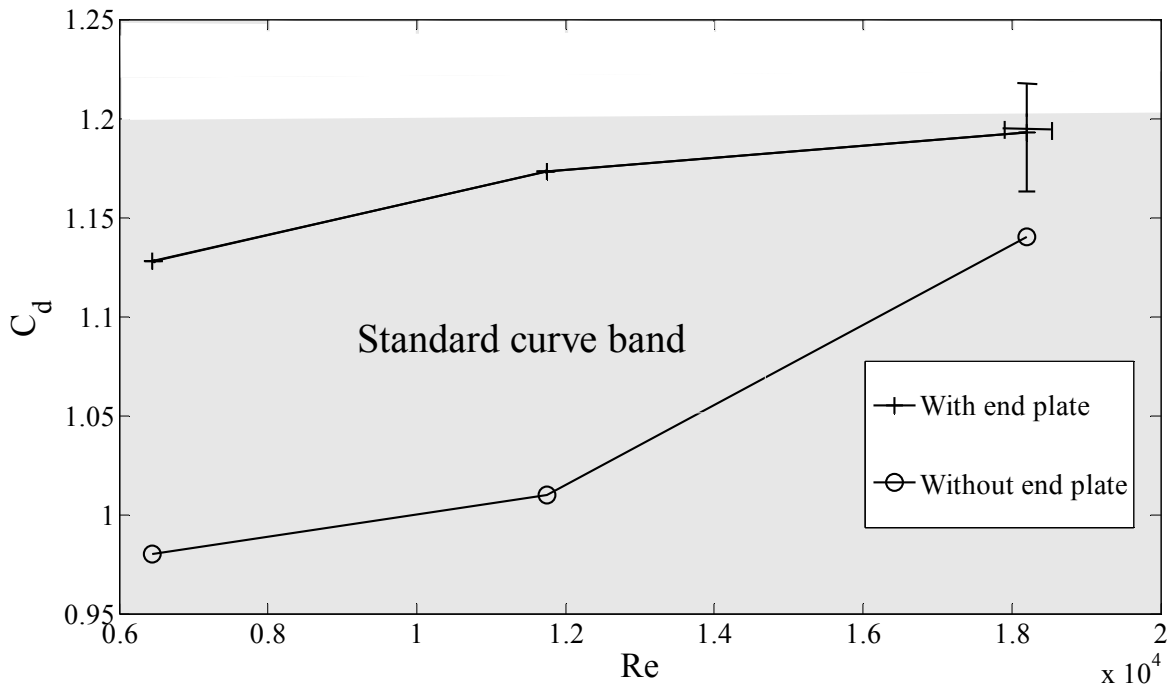


Figure 27 End plate effects on  $C_d$

#### 4.6 Blockage effects on $C_d$

As the cylinder spanned the wind tunnel test section, the blockage ratio is defined as the ratio between the cylinder diameter to the test section height. The blockage ratio in this experiment for the three cylinders used are less than 6%, which is the critical maximum value, reported by West and Apelt [1982], beyond which significant flow distortion, changes in pressure distribution, and varying the Strouhal number occur with increasing blockage ratio. To ensure that blockage is not an issue in the current experiment, the three cylinders with the corresponding end plates were tested for blockage effect. Figure 28 portrays that the drag coefficient value varied less than 0.02 (which is around 1.7%), which is way smaller than the uncertainty limits for  $Re=6450$  (uncertainty is 0.32), and within the uncertainty limits for  $Re=18200$  (uncertainty is 0.03). Thus no blockage correction factor was applied to the results obtained in this study.

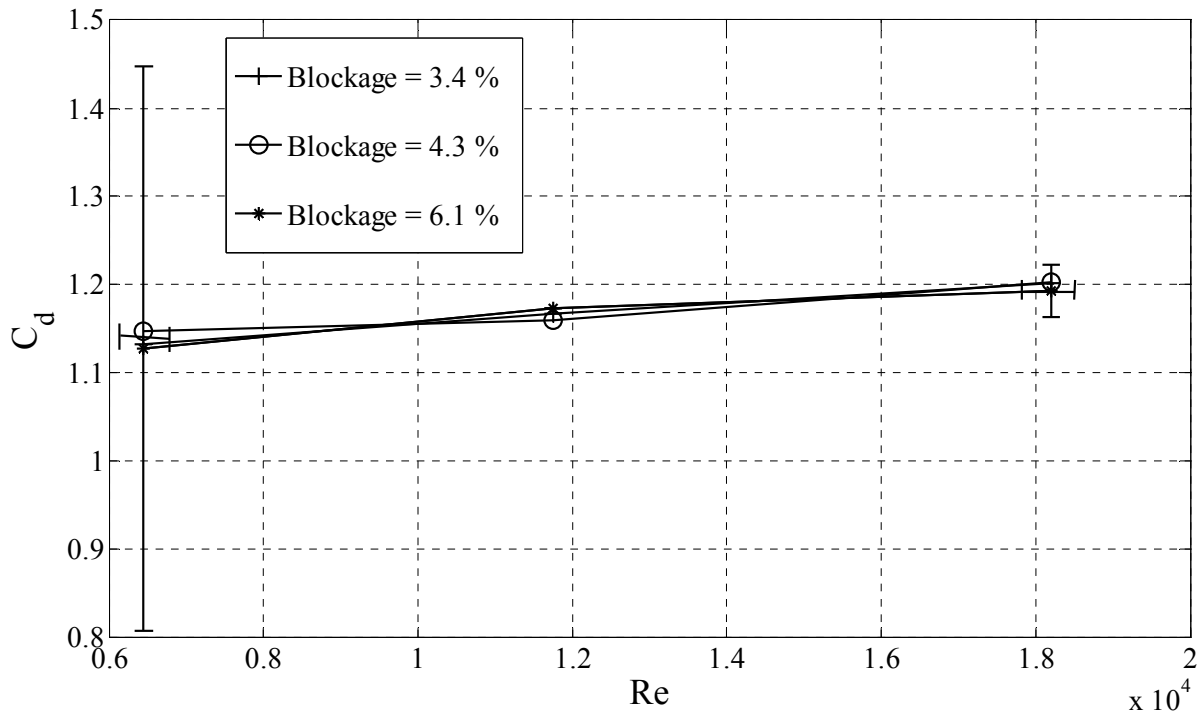


Figure 28 Blockage effects on  $C_d$

#### 4.7 The decay of turbulence downstream of the orificed perforated plate

The freestream turbulence intensity  $Tu$  and flow integral length scale  $\Lambda$  were produced by the utilization of orificed perforated plates. To properly study the independent effects of  $Re$ ,  $Tu$ , and  $\Lambda/D$ , the parameter under investigation was varied over three different values while holding the other two parameters fixed. Thus, a test matrix of  $3 \times 3 \times 3$  was generated. Eight different freestream velocities were chosen, and the characteristics of the orificed perforated plates for these eight velocities were found. For each velocity a power curve fit was employed over five turbulence intensity values, each value at one location downstream of the orificed perforated plate in the wind tunnel (10, 15, 20, 30, and 40), and the equations corresponding to this fit were obtained.

Downstream of the orificed perforated plate, turbulence decays and this is known to be in a power law manner as mentioned by Liu et al. [2007], as shown in Figure 29. The turbulence intensity is a weak function of the wind speed, but it is a strong function of the location downstream of the orificed perforated plate. The value of the turbulence intensity reduced dramatically in the range of  $(x/d = 10)$  to  $(x/d = 20)$  and more slowly after this

location. The characteristics of the incoming fluid, type of grid/its solidity ratio, shape of the opening, and the thickness of the grid are some of the factors affecting the intensity of the turbulence generated, and the rate it decays. The turbulence intensity values and the intensity decay trend in the curves obtained in this study concurred with the earlier researchers, including Bearman [1971] who used mesh (3.81cm by 1.9 cm wooden slats spanning the wind tunnel, the distance between the slats centers was 19cm), and also Moradian et al. [2009] who used the same perforated plates. The Re uncertainty as calculated in Appendix F is equal to  $\pm 348$  for  $Re=6450$  and  $\pm 261$  when  $Re=18200$ . Turbulence intensity uncertainty was estimated in the same Appendix to be  $\pm 0.5\%$  (absolute).

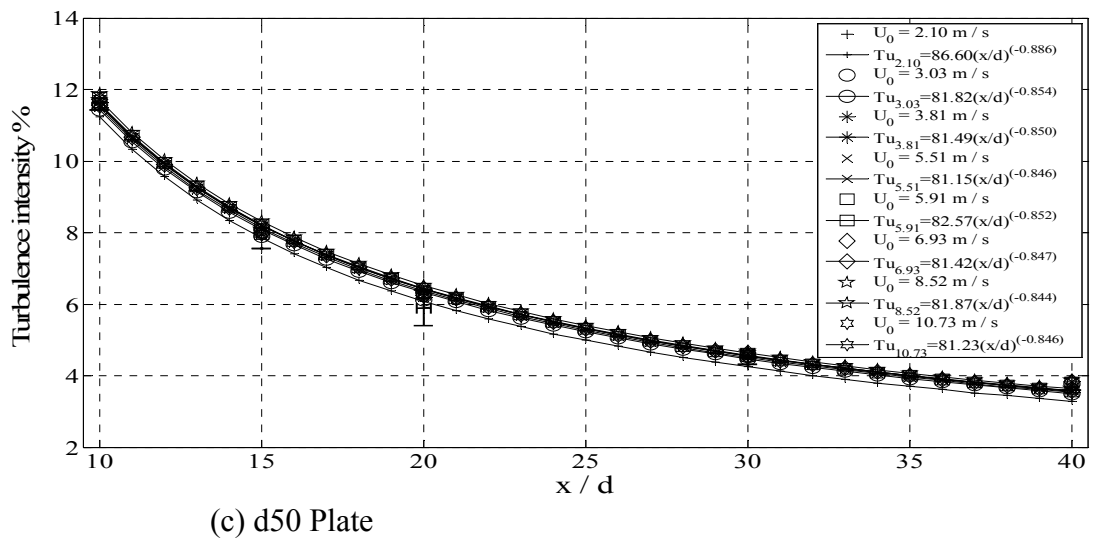
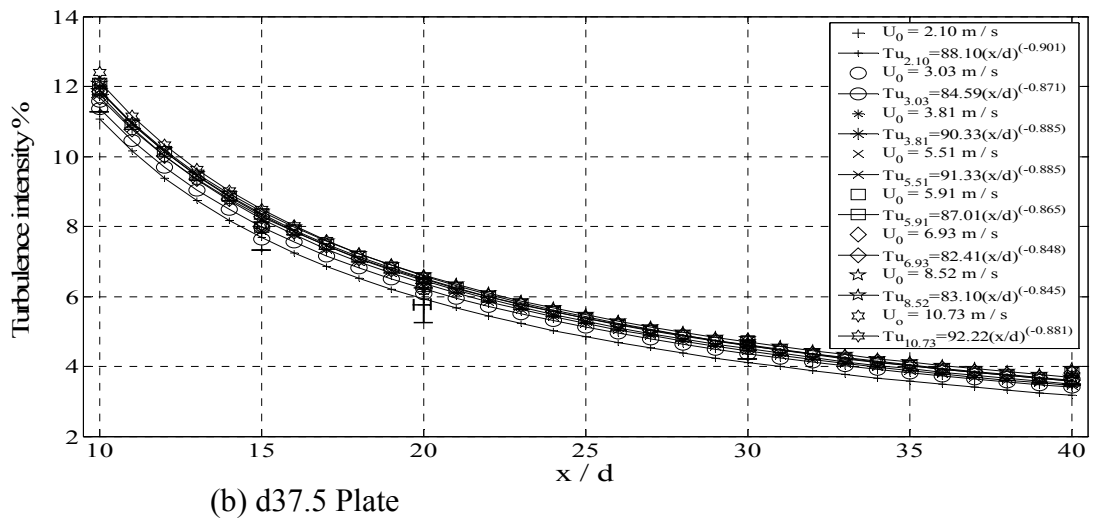
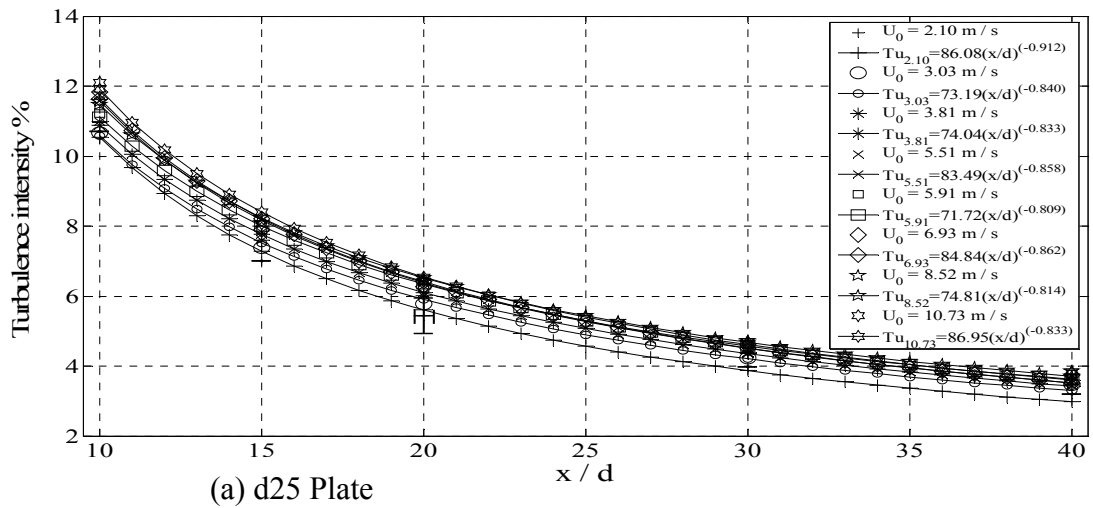


Figure 29 Turbulence intensity downstream of (a) d25 Plate (b) d37.5 Plate (c) d50 Plate

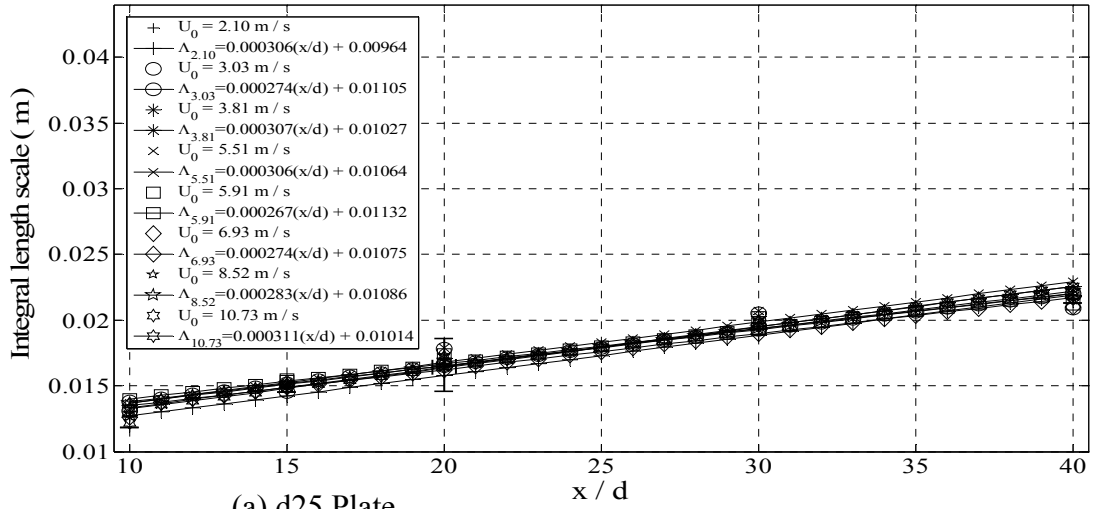


#### **4.8 Integral length scale**

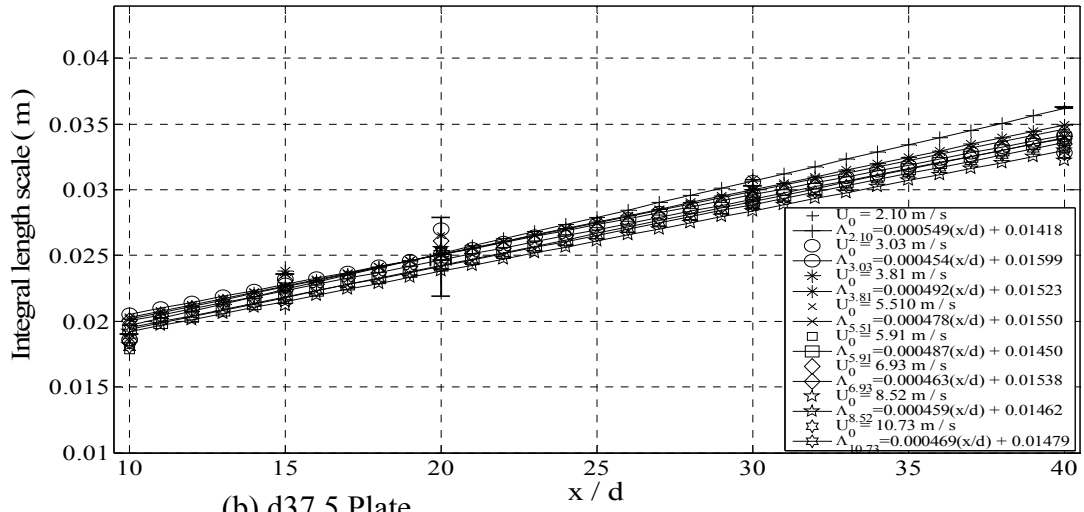
Integral length scale signifies the average size of the energy containing eddies. The magnitude of integral length scale is mainly dependent on the size of perforated plate holes and the spacing between them. As for the turbulence intensity for each plate the integral length scale values associated with the five locations downstream of the orificed perforated plates were plotted. The variation in integral length scale downstream of the perforated plate is nearly linear, for this reason a linear curve fit is employed with an equation associated with each velocity. As shown in Figure 30, the integral length scale slightly depends on  $Re$  and it is a strong function of the location downstream of the orificed perforated plate. The integral length scale values and the length scale trend (integral length scale values increased linearly downstream of the perforated plate) in the curves obtained in this study are consistent with those obtained by Bearman [1971] and Moradian et al. [2009]. The relative integral length scale uncertainty was calculated in Appendix F to be 12%.

#### **4.9 Taylor microscale**

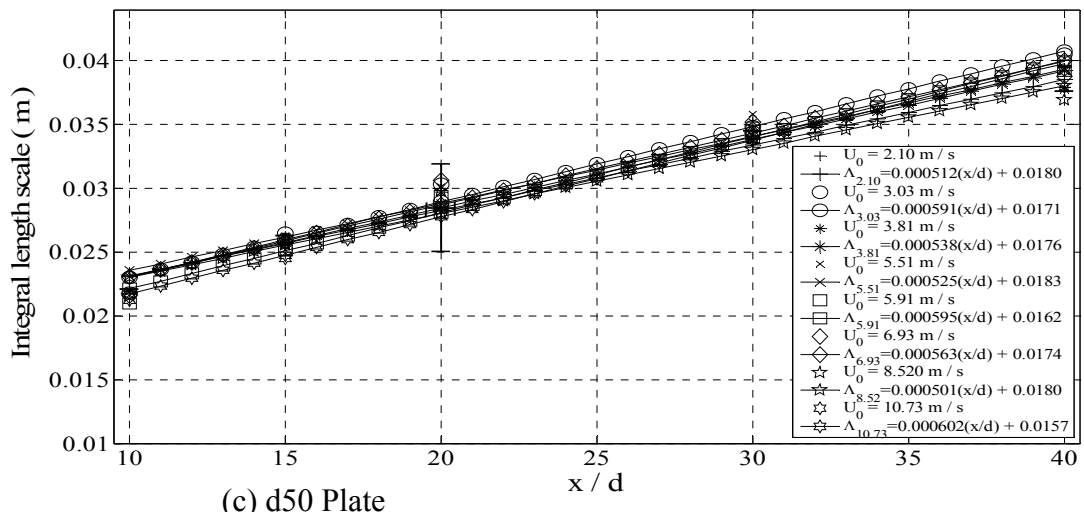
Following the procedure given in section 4.3, Taylor microscale results are obtained and plotted in Figure 31. Taylor microscale decreases as the freestream velocity increases (opposite behavior compared to the integral length scale). The Taylor microscale values within the range of plate locations considered in this study and their trend (Taylor microscale values increase linearly downstream of the perforated plate) of the curves obtained in this study are consistent (within 5%) with those results obtained by Liu et al. [2007] based on the same orificed perforated plates (d37.5 plate with 10.5m/s).



(a) d25 Plate



(b) d37.5 Plate



(c) d50 Plate

Figure 30 Integral length scales downstream of (a) d25 Plate (b) d37.5 Plate

(c) d50 Plate

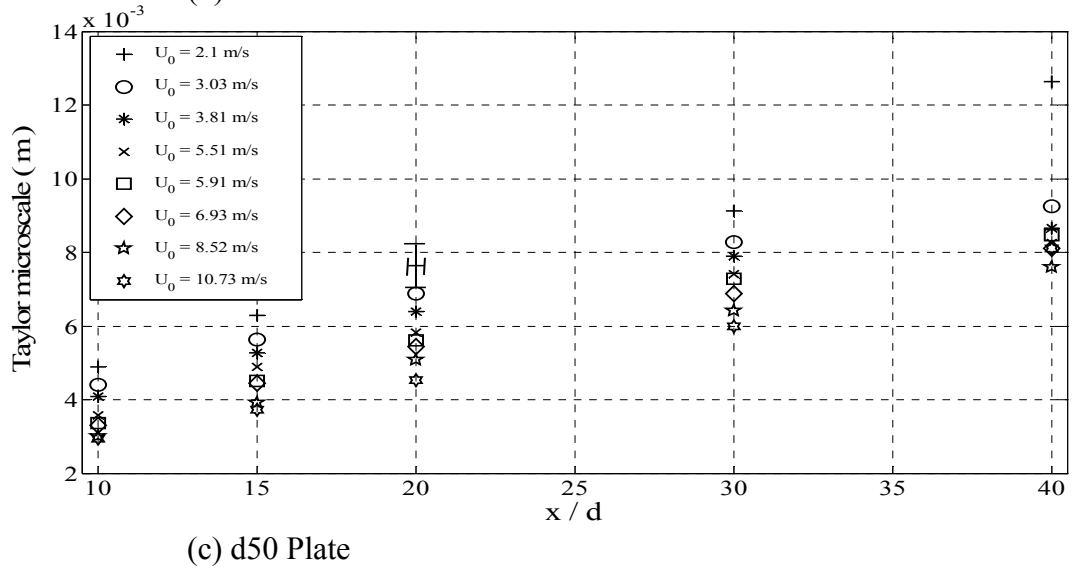
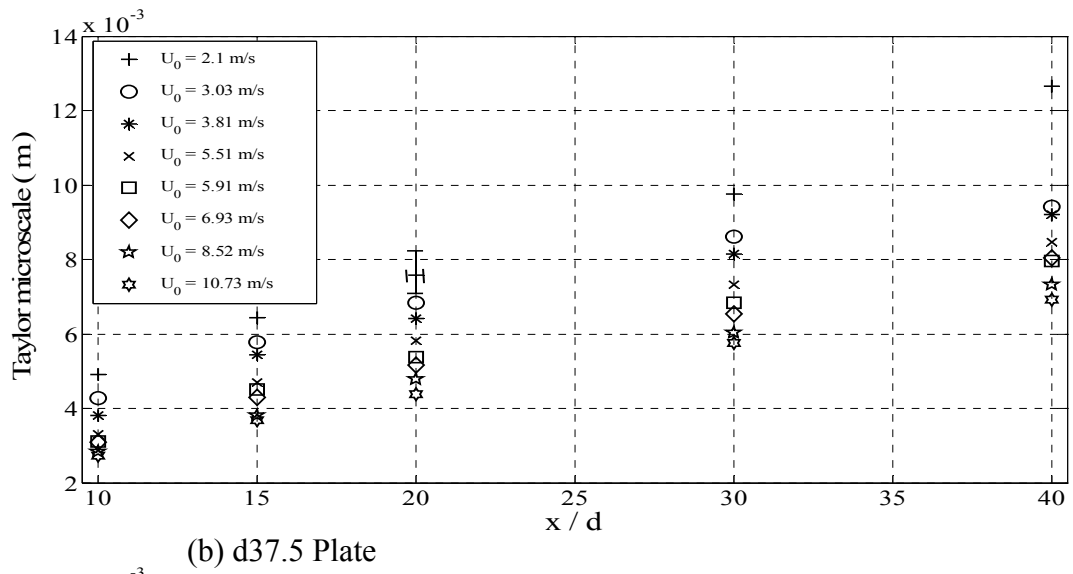
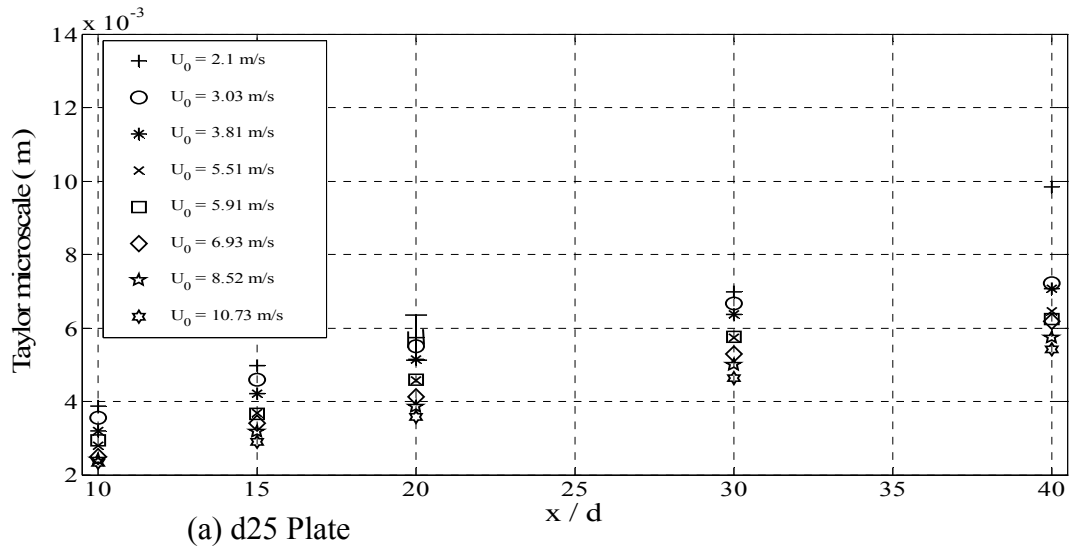


Figure 31 Taylor microscale downstream of (a) d25 Plate (b) d37.5 Plate  
(c) d50 Plate

A linear curve fit for Taylor microscale was employed for two velocities (similar to the integral length scale) corresponding to d25 plate as shown in Figure 32. These two velocities are associated with maximum/nearly the same drag coefficient value change as compared to the smooth flow scenario found in the current study.

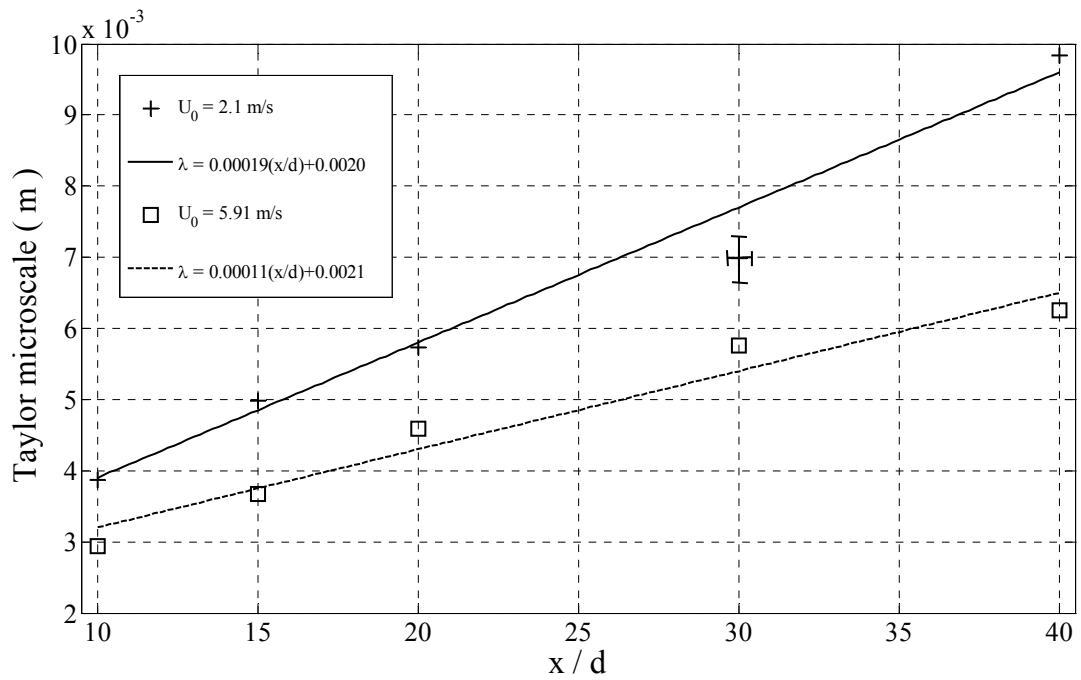


Figure 32 Sample curve fits for  $\lambda$  versus  $x/d$  (d25 plate)

#### 4.10 Re matrix

The Re value was based on the cylinder diameter, as shown in Table 2, to achieve three repeating Re values, eight velocities were needed. Only 3.81 m/s velocity is repeated twice to generate two values of Re which are 6450, and 18200 based on cylinder diameter of 26.7mm, and 48.5mm respectively.

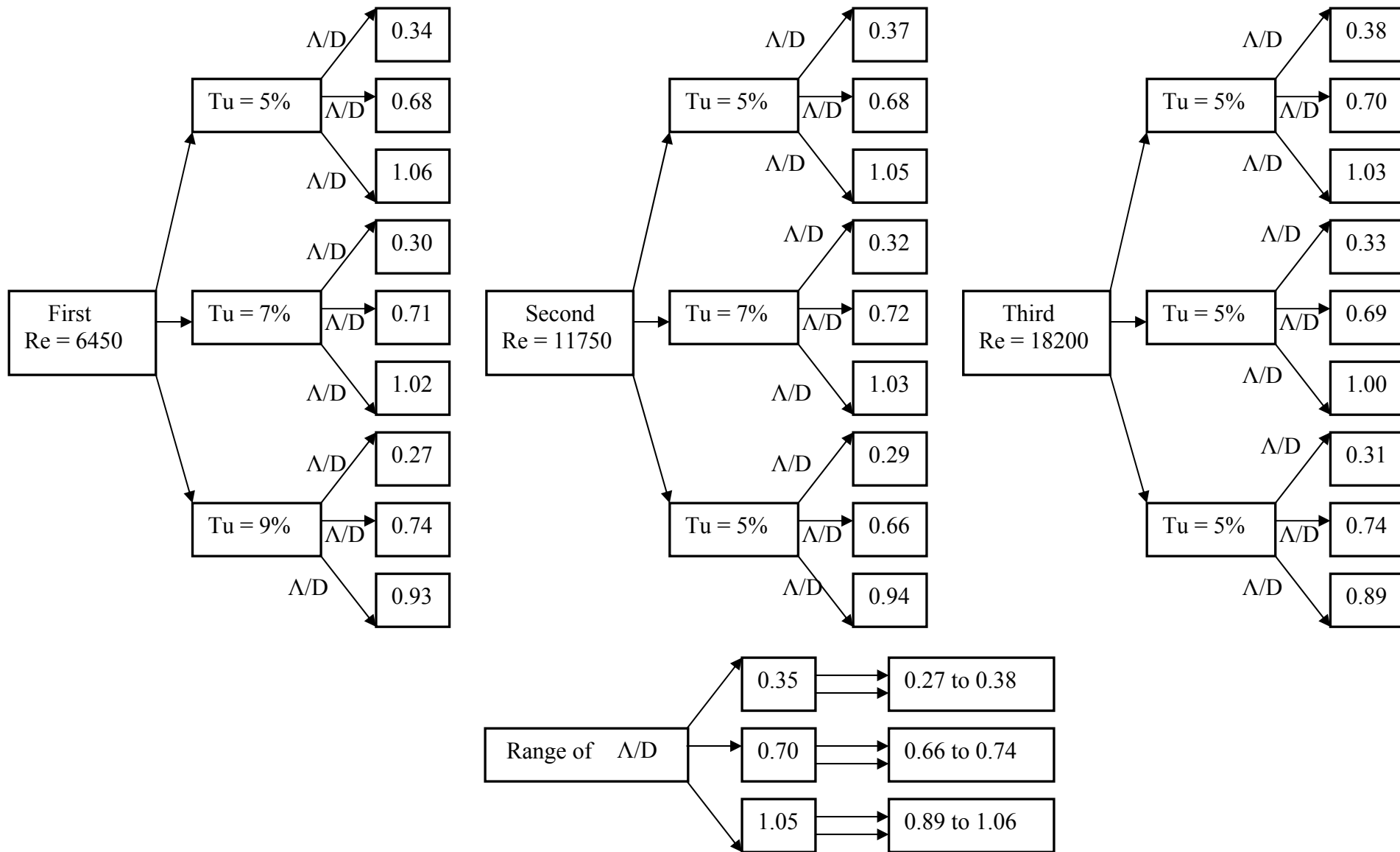
To fix Tu at 5%, 7%, and 9%, the corresponding distance between the orificed perforated plates and the center of the cylinder were selected based on both the power curve fit for Tu and the linear curve fit for  $\Lambda$  equations. When Tu equals to 5% the corresponding plate location was found from the Tu equation. Consequently the corresponding value of  $\Lambda$  for this plate location was found from the  $\Lambda$  equation.

Table 2 Freestream velocity selection to achieve 3 repeating values of Re

Velocity No.	Velocity (m/s)	Cylinder (mm)	Re
1	2.10	48.5	6450
2	3.03	33.6	6450
3	3.81	26.7	6450
4	3.81	48.5	11750
5	5.51	33.6	11750
6	5.91	48.5	18200
7	6.93	26.7	11750
8	8.52	33.6	18200
9	10.73	26.7	18200

The selections for  $\Lambda/D$  values are shown in Table 3, for each velocity, three values of Tu were considered associated with each plate, so each velocity has nine different values of  $\Lambda/D$  (three plates were available). For nine velocities there were 81 different values of  $\Lambda/D$ , only twenty seven values were considered. Results in a range for  $\Lambda/D$  associated with each value of  $\Lambda/D$  under consideration, which were 0.35, 0.7, and 1.05. This range was the nearest values of  $\Lambda/D$  that can be obtained, each value of  $\Lambda/D$  was related to a certain plate located at a certain distance upstream from the cylinder.

Table 3 The selection of the relative integral lengths by three turbulence intensities by three Res



## CHAPTER 5: Results and Discussion

Efforts were made to identify conditions (wind velocity, orificed perforated plate, orificed perforated plate-cylinder distance, and cylinder diameter) which would supply at least three data points based on the independent effects of  $Re$ ,  $Tu$ , and  $\Lambda/D$  on  $C_d$ . To compare the turbulence results with those in the 'no turbulence' scenario, drag measurements were also taken in the absence of the orificed perforated plate. It is found that in the smooth flow case, the freestream turbulence intensity was less than 0.5 %.

### 5.1 Results Table

Table 4 summarizes all drag results obtained in this study. It details the condition associated with each data point in terms of cylinder diameter (and hence, the associated blockage and aspect ratio), plate and plate-cylinder distance (and thus, the free-stream turbulence parameters), and the atmosphere (pressure, temperature and relative humidity, from which the density of air is deduced). The drag results are casted with respect to the corresponding "smooth flow" values, that is, in percentage drag change.

Table 4 Summary of drag results, with the percentage change in the turbulent  $C_d$  value

Tu %	Cylinder diameter(m)	Velocity (m/s)	Re	Plate No.	x/ d	Plate location (in)	Plate location (m)	Integral length scale (m)	$\Lambda/D$	Density $kg/m^3$	Load cell reading (N)	Drag (N)	$C_d$	Drag change %
< 0.5	0.0485	2.10	6467							1.16	0.046	0.092	1.128	
	0.0485	3.81	11732							1.16	0.157	0.314	1.173	
	0.0485	5.91	18199							1.16	0.384	0.768	1.193	
5	0.0485	2.10	6467	25	22.7	22.7	0.575	0.01660	0.34	1.16	0.043	0.086	1.059	-6.1
7	0.0485	2.10	6467	25	15.7	15.7	0.398	0.01440	0.30	1.16	0.037	0.074	0.908	-19.5
9	0.0485	2.10	6467	25	11.9	11.9	0.302	0.01330	0.27	1.16	0.023	0.046	0.563	-50.1
5	0.0485	3.81	11732	25	25.4	25.4	0.646	0.01810	0.37	1.16	0.133	0.266	0.994	-15.3
7	0.0485	3.81	11732	25	17.0	17.0	0.431	0.01550	0.32	1.16	0.104	0.208	0.777	-33.8
9	0.0485	3.81	11732	25	12.6	12.6	0.319	0.01410	0.29	1.16	0.086	0.171	0.641	-45.3
5	0.0485	5.91	18199	25	26.8	26.8	0.682	0.01850	0.38	1.16	0.159	0.318	0.494	-58.6
7	0.0485	5.91	18199	25	17.7	17.7	0.450	0.01610	0.33	1.16	0.162	0.325	0.505	-57.7
9	0.0485	5.91	18199	25	13.0	13.0	0.330	0.01480	0.31	1.16	0.097	0.194	0.302	-74.7
< 0.5	0.0336	3.03	6464							1.17	0.068	0.136	1.148	
	0.0336	5.51	11755							1.17	0.226	0.453	1.160	
	0.0336	8.52	18176							1.17	0.561	1.123	1.203	
7	0.0336	3.03	6464	37.5	17.4	26.2	0.665	0.0239	0.71	1.17	0.063	0.127	1.074	-6.5
9	0.0336	3.03	6464	50	13.2	26.5	0.672	0.0249	0.74	1.17	0.064	0.128	1.088	-5.3
7	0.0336	5.51	11755	37.5	18.2	27.3	0.694	0.02420	0.72	1.17	0.208	0.416	1.067	-8.1
9	0.0336	5.51	11755	37.5	13.7	20.6	0.522	0.02210	0.66	1.17	0.222	0.443	1.136	-2.1
7	0.0336	8.52	18176	37.5	18.7	28.0	0.712	0.02320	0.69	1.17	0.527	1.055	1.130	-6.0
9	0.0336	8.52	18176	50	13.7	27.3	0.693	0.02480	0.74	1.17	0.519	1.039	1.147	-4.7
< 0.5	0.0267	3.81	6459							1.16	0.083	0.166	1.133	
	0.0267	6.93	11748							1.16	0.283	0.567	1.167	
	0.0267	10.73	18190							1.16	0.700	1.400	1.202	
5	0.0267	3.81	6459	25	25.4	25.4	0.646	0.01810	0.68	1.16	0.086	0.171	1.165	2.8
5	0.0267	3.81	6459	37.5	26.3	39.4	1.001	0.02820	1.06	1.16	0.076	0.152	1.035	-8.6
7	0.0267	3.81	6459	50	17.9	35.8	0.910	0.02730	1.02	1.16	0.073	0.146	0.994	-12.2
9	0.0267	3.81	6459	50	13.3	26.6	0.677	0.02490	0.93	1.16	0.067	0.133	0.906	-20.0
5	0.0267	6.93	11748	25	26.6	26.6	0.677	0.01810	0.68	1.16	0.285	0.571	1.175	0.7
5	0.0267	6.93	11748	37.5	27.2	40.8	1.037	0.02800	1.05	1.16	0.335	0.671	1.381	18.4
7	0.0267	6.93	11748	50	18.1	36.2	0.918	0.02760	1.03	1.16	0.288	0.577	1.187	1.7
9	0.0267	6.93	11748	50	13.4	26.9	0.683	0.02500	0.94	1.16	0.268	0.536	1.103	-5.4
5	0.0267	10.73	18190	25	27.3	27.3	0.694	0.01860	0.70	1.16	0.707	1.414	1.214	1.0
5	0.0267	10.73	18190	37.5	27.3	41.0	1.042	0.02760	1.03	1.16	0.776	1.553	1.333	10.9
7	0.0267	10.73	18190	50	18.1	36.2	0.920	0.02660	1.00	1.16	0.750	1.500	1.288	7.2
9	0.0267	10.73	18190	50	13.5	26.9	0.684	0.02380	0.89	1.16	0.693	1.385	1.190	-1.0
no end plate	0.0485	2.10	6467							1.17	0.040	0.080	0.98	-13.0
	0.0485	3.81	11732							1.17	0.136	0.273	1.01	-13.7
	0.0485	5.91	18199							1.17	0.369	0.737	1.14	-4.7



## 5.2 Cylinder drag under 'no turbulence' condition

The turbulence intensity in the wind tunnel in the absence of the orificed perforated plate was measured to be less than 0.5%, therefore the measured drag is expected to be close to the standard  $C_d$ -Re data curve obtained by the earlier researchers. The  $C_d$ -Re results obtained in this study are plotted in Figure 33. The variation of drag coefficient of a smooth cylinder versus Reynolds number in the standard curve over the Re range under consideration was between 1 and 1.2. The current results fall within the 'no turbulence'  $C_d$  versus Re standard curve limits. The uncertainty in the drag coefficient measurement as detailed in Appendix F is  $\pm 0.32$  when  $Re=6450$  and  $\pm 0.03$  when  $Re=18200$ . The reason for this difference in the uncertainty value for different Re range was due to the fact that the absolute uncertainty remains roughly unchanged, and hence, the relative uncertainty decreases with increasing Re.

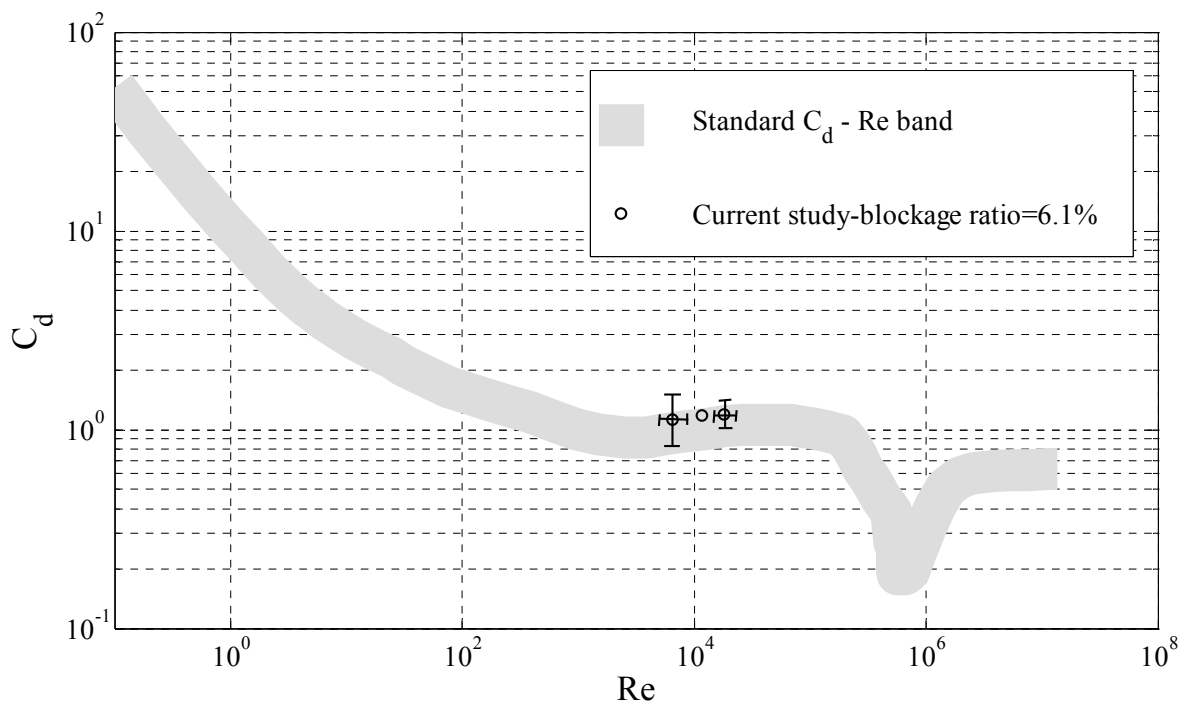


Figure 33 Results for smooth flow on the standard curve

### 5.3 The general effect of freestream turbulence

It is well known that when the flow becomes turbulent, the drop in drag coefficient occurs at lower progressively Re. Increasing the turbulence intensity leads to a decrease in the drag coefficient, however the value of  $C_d$  reduces when  $\Lambda/D$  fall below one. Bruun and Davies [1975] confirmed that turbulence reduces the critical Re. Savkar et al. [1980] confirmed that a drag reduction is achieved due to freestream turbulence which promotes early transition from laminar to turbulent boundary layer and delay in flow separation. The results for both the smooth flow and turbulence are reflected on the standard  $C_d$ -Re band for three turbulence intensities and  $\Lambda/D=0.35$  as shown in Figure 34. Consistent with other researchers (with nearly the same value of  $\Lambda/D$ ), the trend of the first two curves (5% and 7%) were down as Re increases, however when  $Tu=9\%$ , it increased first and then dropped down.

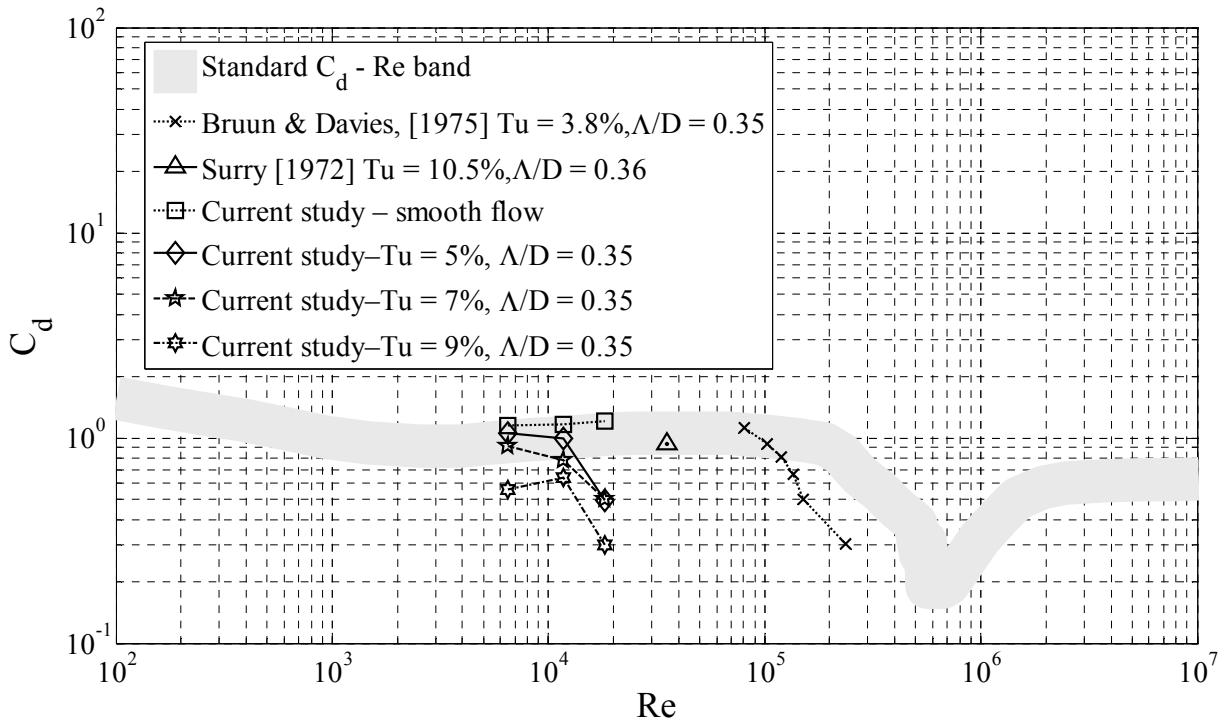


Figure 34  $\Lambda/D=0.35$  Current study results with respect to [Brunn & Davies, 1975, Surry, 1972]

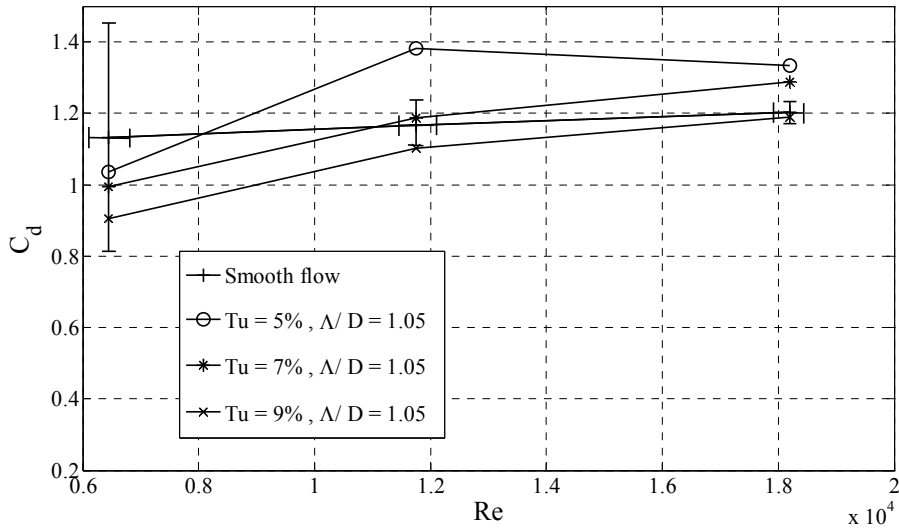
#### 5.4 Effect of turbulent Reynolds number

When  $\Lambda/D=1.05$ , as shown in Figure 35(a), as the Re value increases the  $C_d$  value increases. The  $C_d$ -Re curve is lowered when the Tu value increases, the Tu curve appears to be just above the smooth flow one.

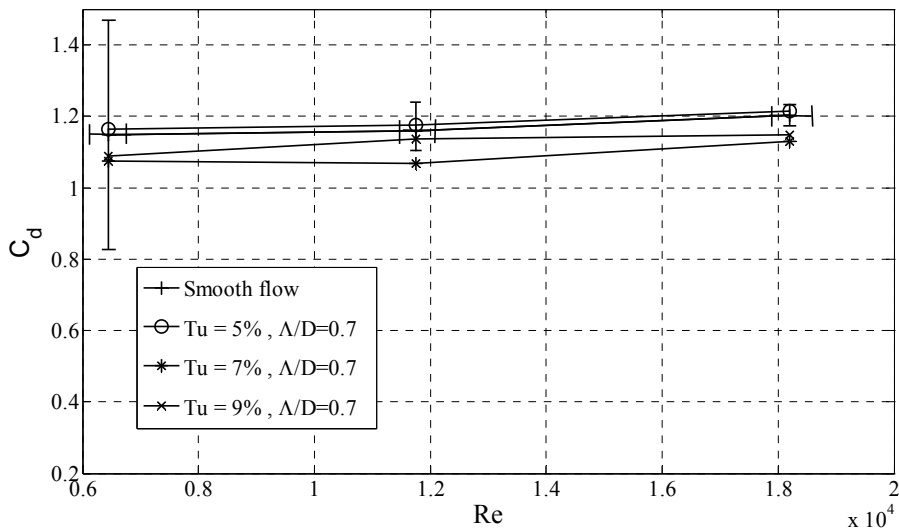
Figure 35(b) shows that at  $\Lambda/D \approx 0.7$ , the drag coefficient is roughly constant and Re effect is negligible.

Finally, and more interestingly when  $\Lambda/D \approx 0.35$ , as shown in Figure 35(c), as the Re value increases the  $C_d$  value decreases. The  $C_d$ -Re curve is lowered when the Tu value increases, the Tu curve appears to be just below the smooth flow one.

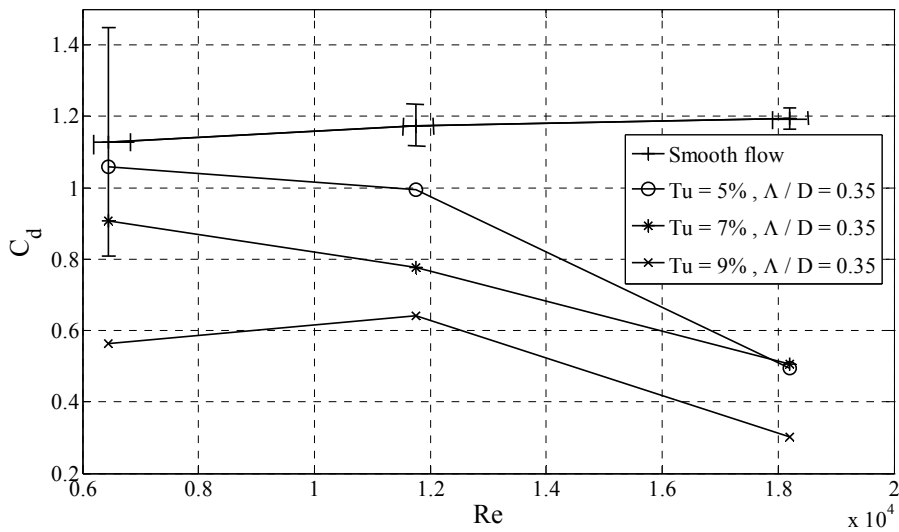
Savkar et al. [1980] confirmed that when  $\Lambda/D$  value is 1.3 (larger than one) and Tu is 9.5% the  $C_d$  value starts outside the standard curve band (larger than the smooth flow) and this value decreases with the increase of Re (lower than the smooth flow). At the same value of Tu and different values of  $\Lambda/D$  the drag coefficient decreases when Re increases. Arie et al. [1981] found when  $\Lambda/D > 1$  for all Tu values the drag coefficient values are outside the standard curve band (larger than the smooth flow values), while when the  $\Lambda/D$  decreases, the trend is down towards a lower value of  $C_d$  when Re increases. Ko and Graf [1972] mentioned that the turbulence intensity, together with the turbulence scale, must be considered. At the same Tu value, with Re value increasing the effect of Re on  $C_d$  depends on  $\Lambda/D$  value. The drag coefficient value increases if  $\Lambda/D > 1$  and starts decreasing when  $\Lambda/D < 1$ .



(a)  $\Lambda/D = 1.05$



(b)  $\Lambda/D = 0.7$



(c)  $\Lambda/D = 0.35$

Figure 35 Re Effects (a)  $\Lambda/D = 1.05$  (b)  $\Lambda/D = 0.7$  (c)  $\Lambda/D = 0.35$

## 5.5 Effect of turbulence intensity

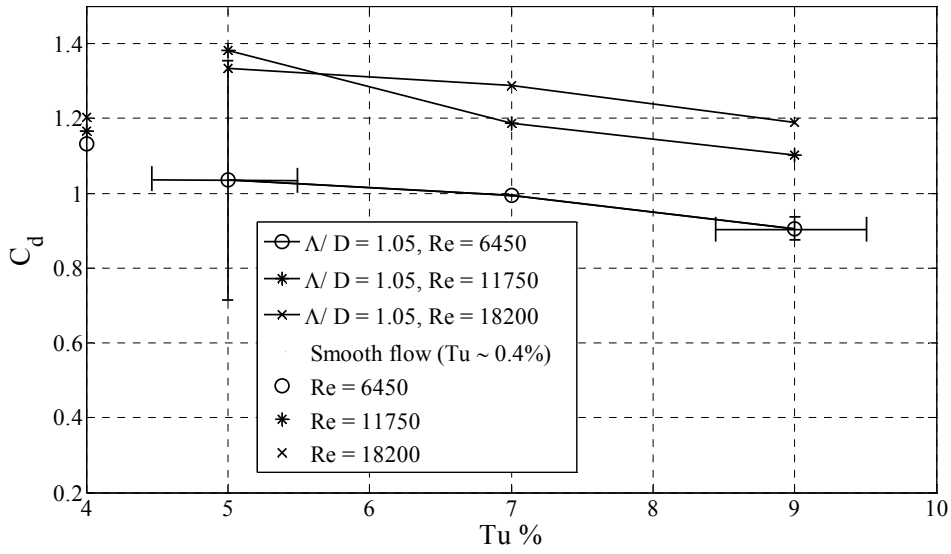
Increasing the turbulence intensity leads to a decrease in the drag coefficient, these results are in agreement with the results obtained by Arie et al. [1981]. Bearman [1968] confirmed that increasing the turbulence intensity leads to reduced drag. Fage and Warsap [1929] found that turbulence shifts the  $C_d$ -Re curve to the left towards a lower critical Re. Dyban et al. [1974] confirmed that turbulence shifts the start of the boundary layer separation point from  $81^\circ$  to  $88^\circ$  downstream as Tu increases from 0.5 % to 25 %. They showed that increasing the flow turbulence reduces the velocity gradient at the cylinder leading surface. Mulcahy [1984] confirmed that more turbulent flow produces a smaller subcritical range of Re. Savkar et al. [1980], So and Savkar [1981], Blackburn and Melbourne [1996], and Sanitjai and Goldstein [2001] concurred the shift of the transition region to a lower Re due to the presence of turbulence. Bruun and Davies [1975] confirmed that when a grid is introduced to disturb the flow, the drag coefficient reduces with values depending on the grid characteristics and grid-cylinder distance.

Figure 36(a) shows that when  $\Lambda/D=1.05$ , the curves generally take the standard trend down with increasing Re for all values of Re considered. It is clear from the curves that at any Re value, increasing the turbulence intensity causes a reduction in the drag coefficient.

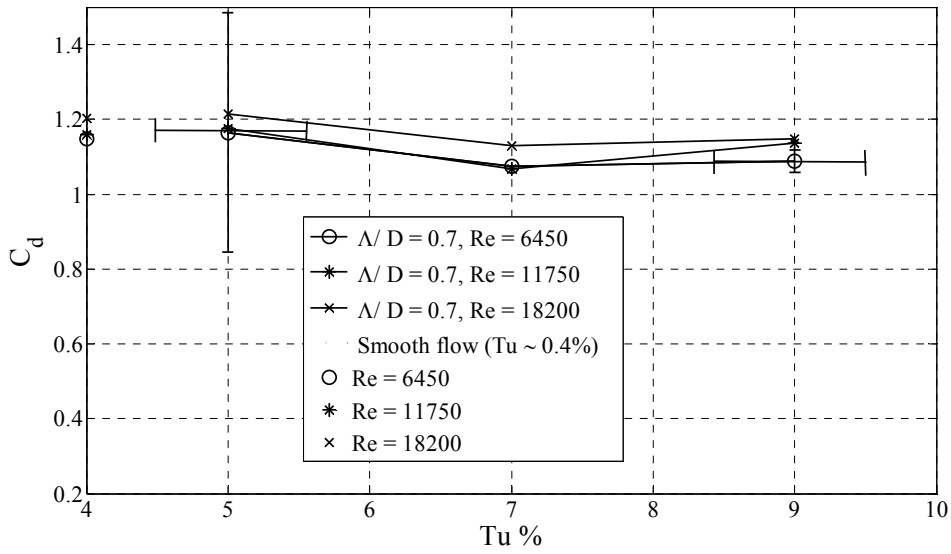
As shown in Figure 36(b) at  $\Lambda/D=0.7$ , the drag coefficient decreases slightly with increasing Tu, especially from 5% to 7%.

Figure 36(c) illustrates that when  $\Lambda/D=0.35$  the drag coefficient decreases most significantly with increasing Tu. This is particularly the case for Re values of 6450 and 11750.

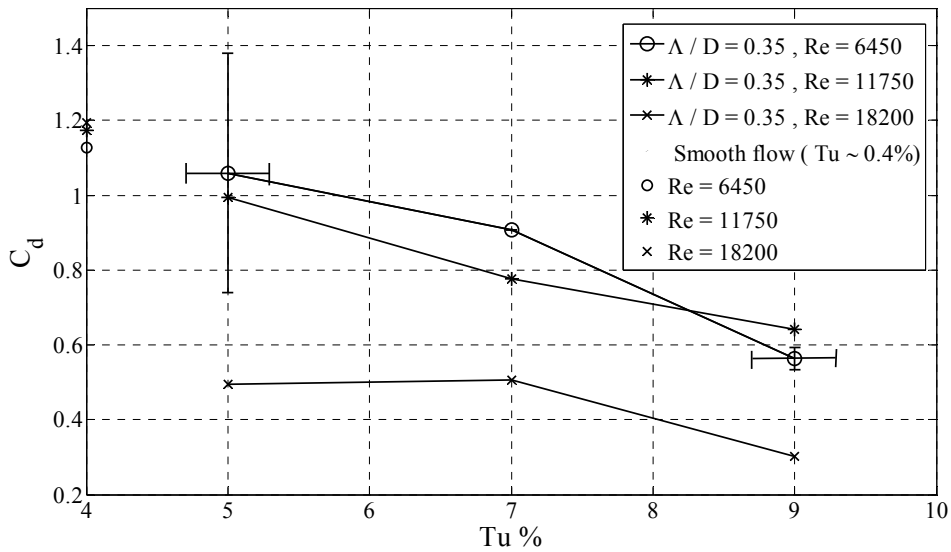
The current results have confirmed the general trend of decreasing drag coefficient while increasing turbulence intensity of the flow past a circular cylinder.



(a)  $\Lambda/D = 1.05$



(b)  $\Lambda/D = 0.7$



(c)  $\Lambda/D = 0.35$

Figure 36 Tu Effects (a)  $\Lambda/D = 1.05$  (b)  $\Lambda/D = 0.7$  (c)  $\Lambda/D = 0.35$

## 5.6 Effect of integral length scale

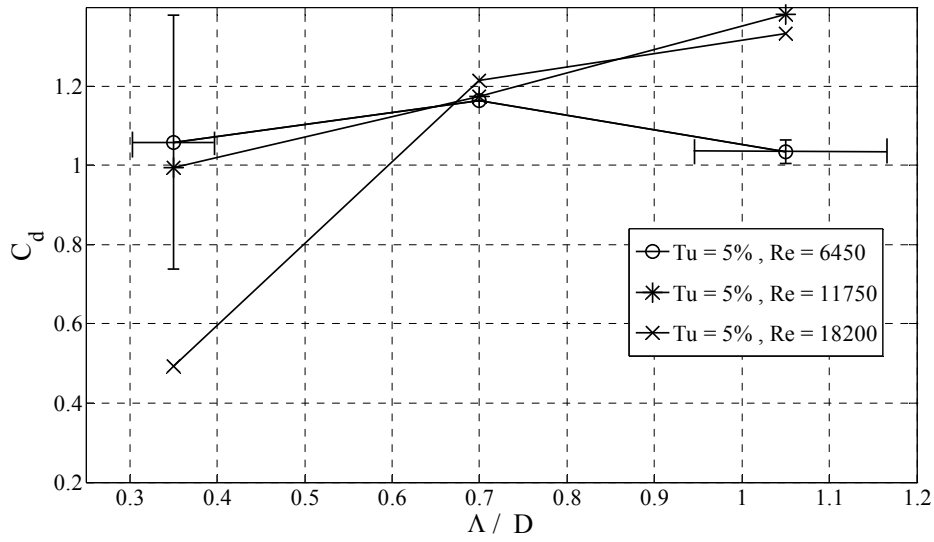
Surry [1972] showed the significant role that the integral length scale plays at constant turbulence intensity. He suggested that the turbulence scale has a couple of effects; a direct effect on the change of the position of the boundary layer separation points and the effect on the flow outside the boundary layer, including the wake. As shown in Figure 6, concerning Surry's [1972] results, when having the Tu value around 10%, the  $C_d$  value reduces by 25% when the  $\Lambda/D$  reduces from 4.3 to 0.35. Savkar et al. [1980] showed that the drag increases for  $\Lambda/D > 1$ , however they had limited evidence for the effect when  $\Lambda/D < 1$ . Arie et al. [1981] confirmed that drag decreases as  $\Lambda/D$  decreases. Kwok [1986] suggested that just a small turbulence scale (when  $\Lambda/D < 1$ ) with adequate length is required to produce a reduction in the drag coefficient, as the boundary layer promotes the early transition from laminar to turbulent associated with a delay in flow separation. Ohya [2004] found that turbulence effects on the circular cylinder drag coefficient disappear when  $\Lambda/D \gg 1$ .

As shown in Figure 37(a), for Re values of 11750 and 18200 associated with  $\Lambda/D$  value is 1.05 the drag coefficient values are higher than the drag values for smooth flow.

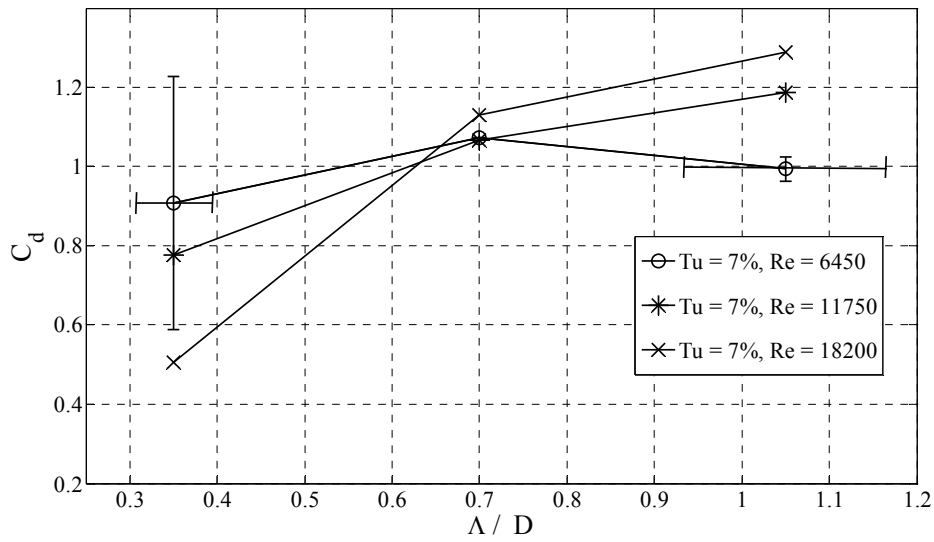
As shown in Figure 37(a) and 37(b) at Tu=5%, and Tu=7%, respectively, the drag coefficient value increases when the value of  $\Lambda/D$  increases from 0.35 to 1.05 for Re values of 11750 and 18200. However, when Re = 6450 the drag value increases until  $\Lambda/D$  hits a value of 0.7, any further increase in  $\Lambda/D$  causes a decrease in the drag coefficient value.

Figure 37(c) shows that when Tu=9%, the drag coefficient value increases when the value of  $\Lambda/D$  increases from 0.35 to 1.05 for Re value 18200. However, when Re=6450 and Re=11750 the drag value increases until  $\Lambda/D$  reaches a value of approximately 0.7, any further increase in  $\Lambda/D$  causes a decrease in the drag coefficient value.

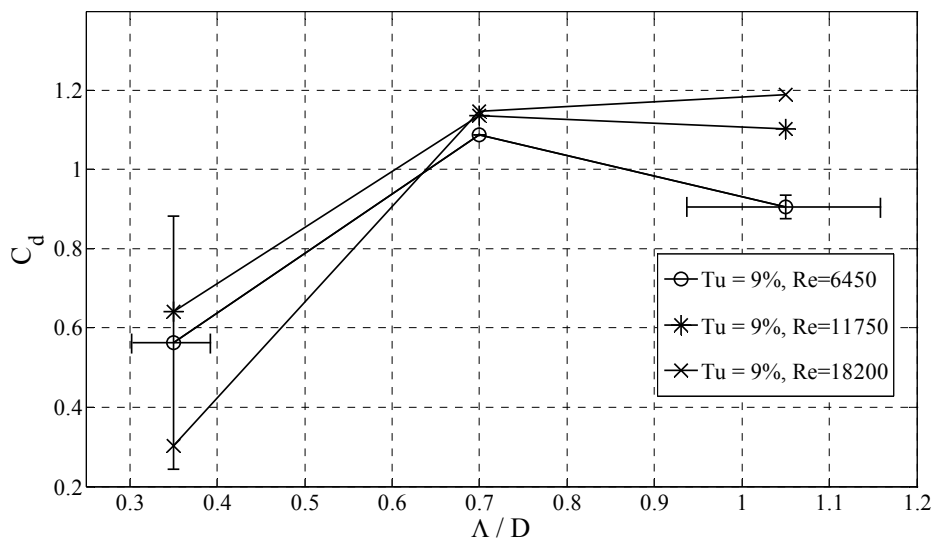
The current results have confirmed the general trend of decreasing drag coefficient while decreasing  $\Lambda/D$ .



(a) Tu = 5%



(b) Tu = 7%



(c) Tu = 9%

Figure 37  $\Lambda / D$  Effects (a) Tu = 5% (b) Tu = 7% (c) Tu = 9%



### 5.7 Taylor microscale with drag coefficient

From the current experiment drag results (Table 4) and for the 48.5 mm cylinder the drag coefficient changes as compared to the smooth flow scenario at  $\Lambda/D$  value of 0.35 is -6.1%, and -74.7% when the freestream velocities are 2.1 m/s and 5.91 m/s, respectively. The corresponding plate size, and location from Table 4, can be substituted in the Taylor microscale linear curve fit equation to find the value of Taylor microscale related to that drag coefficient change. As shown in Figure 38, reducing  $\Lambda$  value from 16.6mm to 14.8mm cause the drag coefficient to reduce from 1.06 to 0.30 (-6.1% to -74.7% drag reduction as compared to the smooth flow scenario), associated with a reduction in Taylor microscale from 6.3 mm to 3.5 mm.

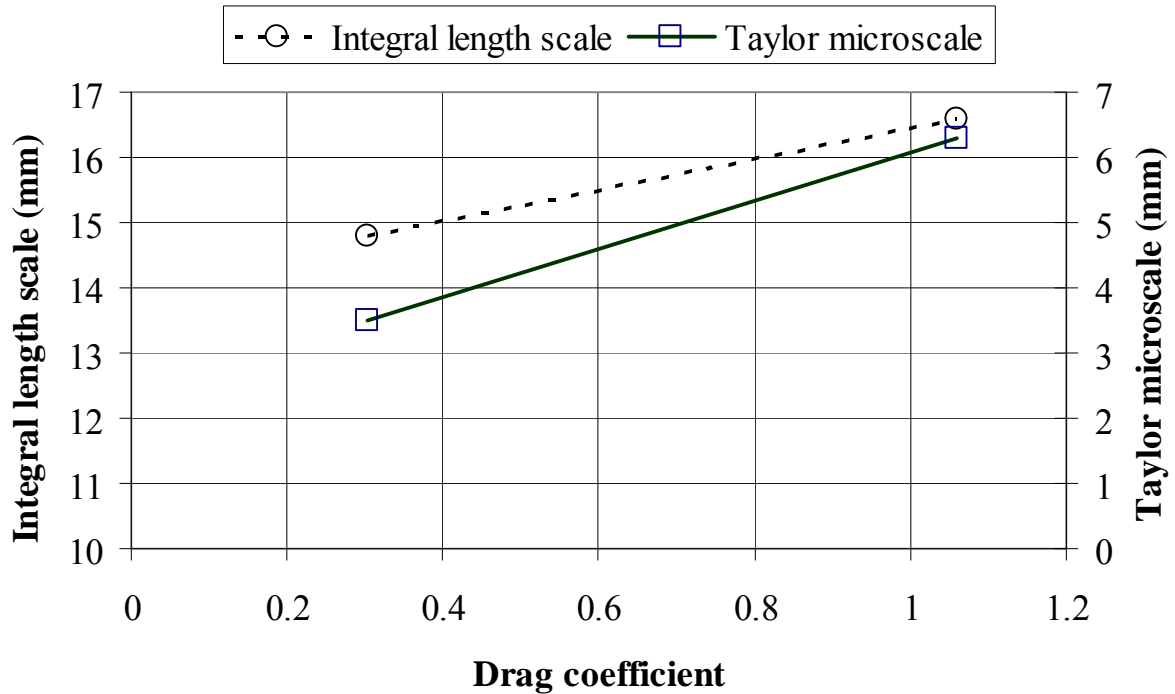


Figure 38 Integral length scale/Taylor microscale versus  $C_d$ ,  $D = 48.5\text{mm}$

From Table 4 and for the 26.7 mm cylinder, the drag coefficient changes as compared to the smooth flow scenario at  $\Lambda/D$  value of 1.05 are 18.4%, and -1%, when the freestream velocities are 6.9 m/s and 10.7 m/s, respectively. The corresponding plate size, and location from Table 4, can be substituted in the Taylor microscale linear curve fit equation to find the value of Taylor microscale related to that drag coefficient change. As shown in Figure 39, increasing  $\Lambda$  value from 23.8mm to 28mm causes the drag coefficient to increase from 1.19 to 1.38, associated with an increase in Taylor microscale from 3.49 mm to 6.15 mm.

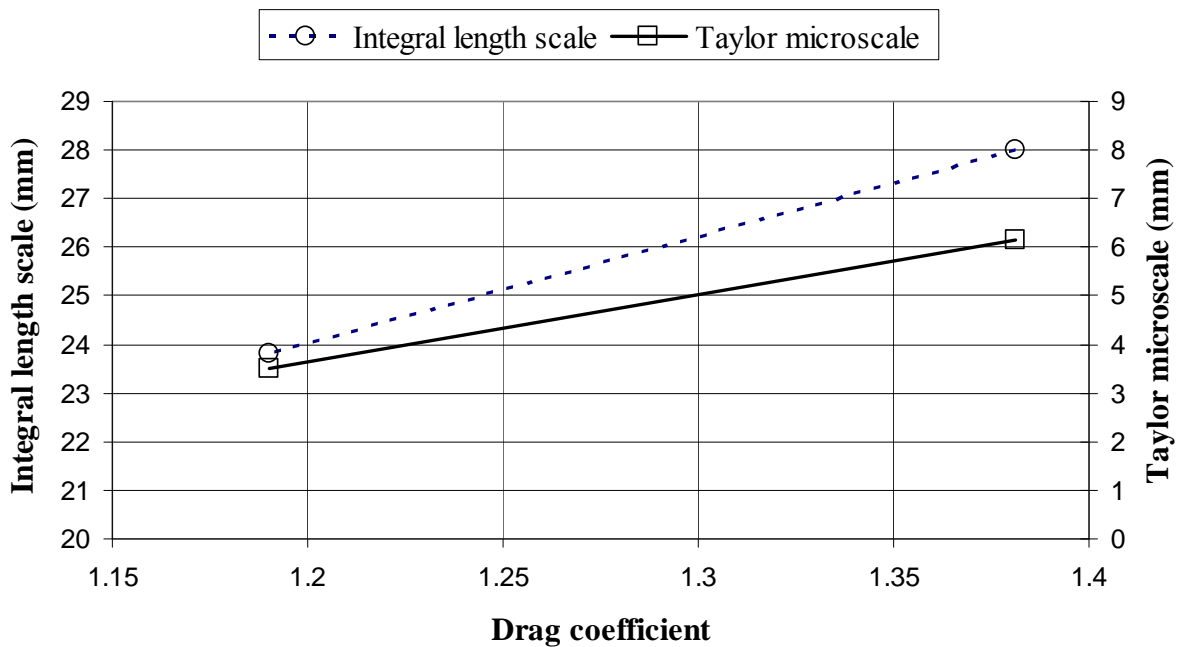


Figure 39 Integral length scale/Taylor microscale versus  $C_d$ ,  $D = 26.7\text{mm}$

From these two cases, the change in  $\lambda$  indicate a larger change in  $C_d$ , when there is a drag reduction, and the change in  $\Lambda$  indicate a larger change in  $C_d$  when there is a drag increase. If this is consistent true, then  $\Lambda/D$  or  $\lambda/D$  is a more appropriate scale depending on the trend of drag change.

### 5.8 Drag results on a three dimensional curve

The results obtained in the current study were plotted together in a three dimensional curve as illustrated in Figure 40 (three values of  $Re$ , 6450, 11750, and 18200 versus three values of  $\Lambda/D$ , 0.35, 0.7, and 1.05 associated with three values of  $Tu$  5%, 7%, and 9%). The results have confirmed the general trend of decreasing drag coefficient with increasing turbulence intensity at the same value of  $Re$  and  $\Lambda/D$ . These results are in agreement with the results obtained by Arie et al. [1981], Bearman [1968]. Moreover, results has confirmed the trend of decreasing drag coefficient as either the value of  $Re$  or  $Tu$  increases, as well when the value of  $\Lambda/D$  decreases, and the trend of increasing drag coefficient as the value of  $\Lambda/D$  increases, which are in agreement with the results obtained by Surry [1972], Savkar et al. [1980] and Arie et al. [1981]. Yeboah et al. [1997] showed that when  $\Lambda/D < 1$  and  $Re < 10^4$  the mean pressure coefficient are higher than the laminar flow, they showed that the drag increases when  $\Lambda/D > 1$ .

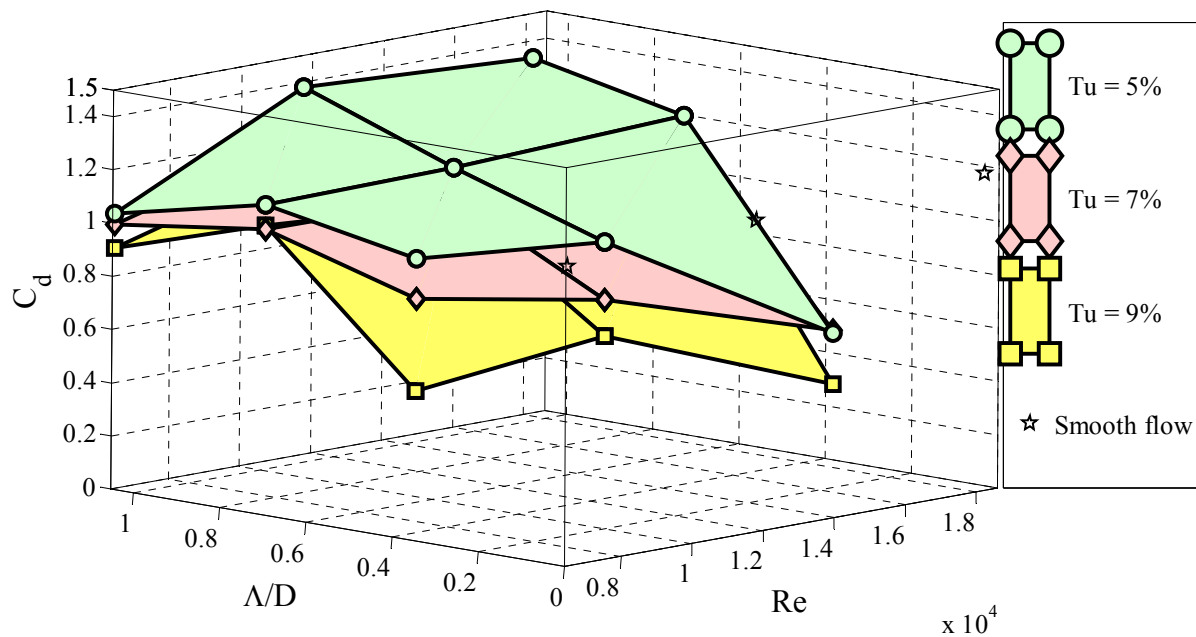
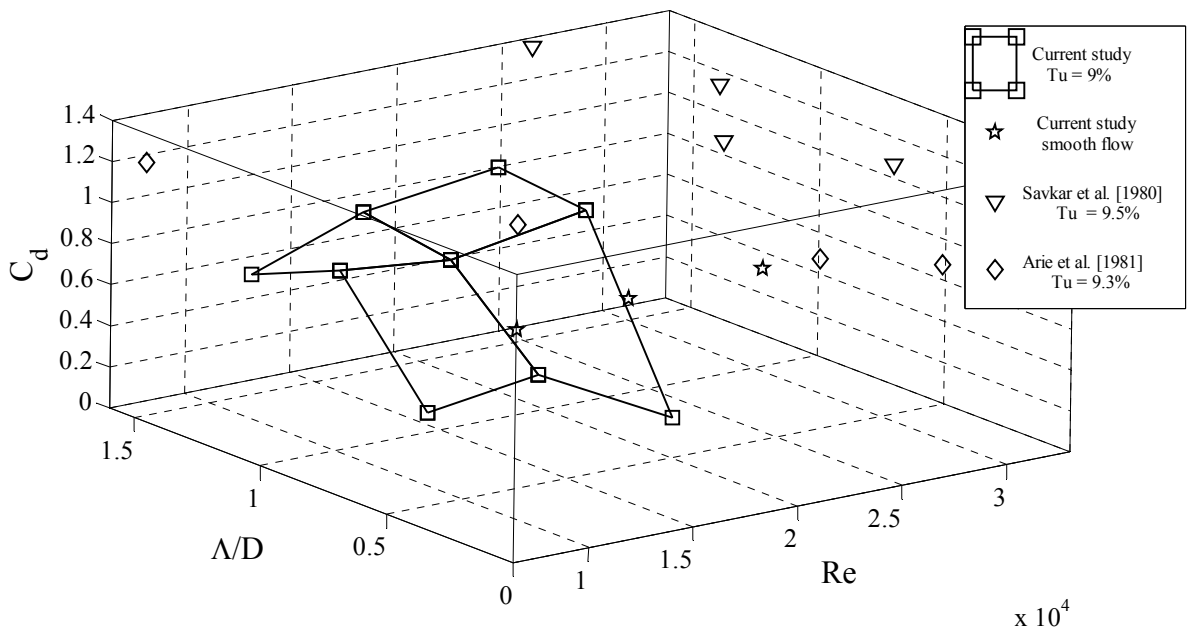


Figure 40 Drag results for the current study

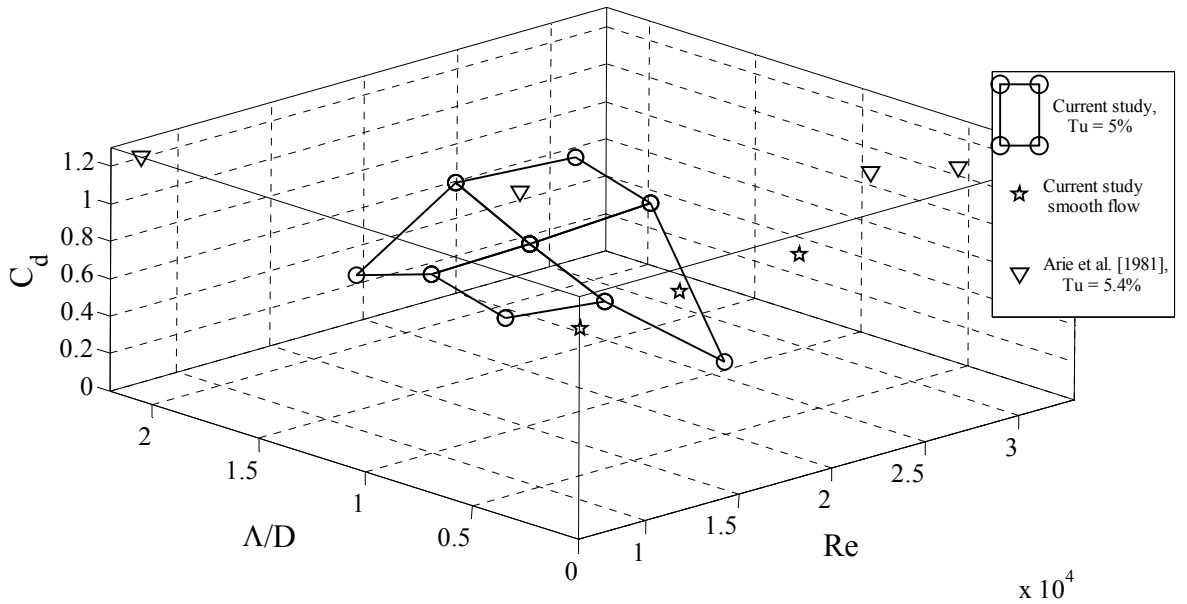
## 5.9 Current drag results comparison

As shown in Figure 41(a), Savkar et al. [1980] and Arie et al. [1981] confirmed that when  $\Lambda/D > 1$  and  $Tu \approx 9\%$ , the drag coefficient value is higher than the smooth flow, however as  $\Lambda/D$  decreases the value of drag decreases. As shown in Figure 41(b), Arie et al. [1981] confirmed that when  $\Lambda/D$  equal to 2.17 and  $Tu \approx 5\%$ , the drag coefficient value is higher than the smooth flow, however as  $\Lambda/D$  decreases the value of drag decreases.

As shown in Figure 42, Arie et al. [1981] agreed that when  $\Lambda/D$  is 2.11 and  $Tu$  is relatively high at 12.3%, the drag coefficient value is nearly equal to the smooth flow value. This confirms that increasing  $Tu$  can lead to an increased drag when  $\Lambda/D$  is large. In other words, certain higher-than-unity  $\Lambda/D$  conditions tend to compromise the drag reduction effect of freestream turbulence. At lower  $\Lambda/D$  values, however, the general trend of decreasing drag coefficient with increasing turbulence intensity prevails. Surry [1972] found that when  $\Lambda/D$  is 9.8 and  $Tu$  is relatively low at 2.5%, the drag coefficient value is higher than that obtained in smooth flow; however, as  $\Lambda/D$  decreases to a value of 0.36 the value of drag decreases below the smooth flow value. Kiya [1982] found that when  $\Lambda/D$  equals to 1.09 and  $Tu$  is relatively high at 10.6%, the drag coefficient value is higher than that when  $\Lambda/D$  equals to 0.79 with  $Tu$  of 12.8%. Bruun and Davies [1975] confirmed that for the same value of  $\Lambda/D$  and  $Tu$ , the drag coefficient decreases with increasing  $Re$ .



(a) Current drag results when  $Tu = 9\%$  compared to Savkar et al. [1980],  $Tu = 9.5\%$  Arie et al. [1981],  $Tu = 9.3\%$



(b) Current drag results when  $Tu = 5\%$  compared to Arie et al. [1981],  $Tu = 5.4\%$

Figure 41 Drag results comparison (a) Current drag results when  $Tu = 9\%$  compared to Savkar et al. [1980],  $Tu = 9.5\%$ , and Arie et al. [1981],  $Tu = 9.3\%$  (b) Current drag results when  $Tu = 5\%$  compared to Arie et al. [1981],  $Tu = 5.4\%$

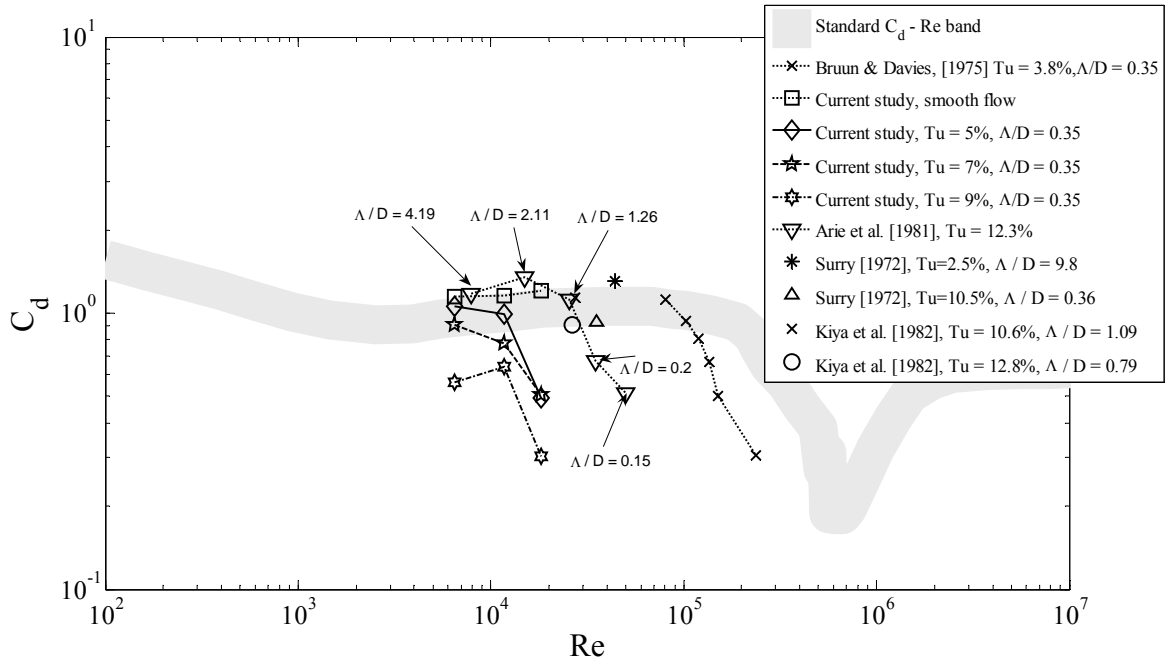


Figure 42 Current drag results compared to Bruun & Davies, [1975], Arie et al. [1981], Surry [1972], and Kiya et al. [1982]

## CHAPTER 6: Conclusions and Recommendations

The independent effects of freestream Reynolds number ( $Re$ ), turbulence intensity, and the integral length scale/cylinder diameter ratio ( $\Lambda/D$ ) on the drag coefficient of a circular cylinder were experimentally investigated. The investigation was conducted in a closed-loop wind tunnel over a Reynolds number, based on the cylinder diameter, range of  $6.45 \times 10^3$  to  $1.82 \times 10^4$ . The proper combination of orificed perforated plate holes diameter, and cylinder location with respect to the orificed perforated plate and the wind speed in the wind tunnel enabled the quasi-independent alterations of Reynolds number, turbulence intensity, and relative integral length scale.

### 6.1 Conclusions

1. The current results have confirmed the general trend of decreasing the drag coefficient while increasing turbulence intensity of the flow past a circular cylinder.
2. The current results have confirmed that the drag coefficient decreases when  $\Lambda/D$  falls below one.

3. At the same value of  $Re$  and  $\Lambda/D$  the drag coefficient of a circular cylinder typically increases as the turbulence intensity decreases.

4. The drag coefficient increases as  $\Lambda/D$  increases, and this increase reaches a maximum value of 18.4% as compared to the smooth flow case, when  $\Lambda/D \approx 1.05$ ,  $Re=11750$ , and  $Tu=5\%$ .

5. More interestingly, the role of  $\Lambda/D$  on the circular cylinder drag coefficient is revealed, as shown by the current experiment results, the drag coefficient can be reduced dramatically by 74.7% compared to the smooth flow case, by decreasing  $\Lambda/D$  to a value of 0.35, associated with a high level of turbulence intensity (9%).

## 6.2 Recommendations

One of the challenges in the current experiments was the perforated plate placement in the wind tunnel (it was time consuming to confirm the exact location of the plate, as the wind tunnel has to be switched off and on every time) according to the facilities and equipment available an appropriate project for future work can be suggested:

1. Test the influence of the conveyor belt, one closed loop belt moves by a motor (the motor is located outside the wind tunnel). This belt moves horizontally with a different number of layers back and forth, with a certain distance apart between one layer and another. Two belts can be employed and the movement can be both horizontal and vertical. This conveyor belt is a turbulence manipulator alternative, compared to the orificed perforated plates. The test includes the conveyor belt ability to generate a nearly isotropic turbulence along the test section.

2. Make surface pressure measurements for the ABS cylinders and compare them with the drag measurements by performing pressure taps in appropriate locations in a fixed cylinder or via one tap and the cylinder can rotate with accurate angle measurements to measure the pressure at different angles.

3. Perform tuft flow visualization behind the cylinder to visualize the wake structure for different  $Re$ .

## REFERENCES

- Achenbach, E., 1971, "Influence of roughness on the cross-flow around a circular cylinder," *Journal of Fluid Mechanics*, v 46, pp. 321-335
- Arie, M., Kiya, M., Suzuki, Y., Hagino, M., Takahashi, K., 1981, "Characteristics of circular cylinders in turbulent flows," *Bulletin of the Japan Society of Mechanical Engineers*, v 24, n 190, pp. 640-647
- Bearman, P. W., 1968, "Some effects of turbulence on the flow around bluff bodies," National Physical Laboratory, Aerodynamics division, Report 1264
- Bearman, P. W., 1969, "On vortex shedding from a circular cylinder in the critical Reynolds number regime," *Journal of Fluid Mechanics*, v 37, pt. 3, pp. 577-585
- Bearman, P. W., 1971, "An investigation of the forces on flat plates normal to a turbulent flow," *Journal of Fluid Mechanics*, v 46, pt. 1, pp. 177-198
- Blackburn, H.M., Melbourne, W. H., 1996, "The effect of free-stream turbulence on sectional lift forces on a circular cylinder," *Journal of Fluid Mechanics*, v 306, pp. 267-292
- Bruun, H. H., Davies, P. O. A. L., 1975, "An experimental investigation of the unsteady pressure forces on a circular cylinder in a turbulent cross flow," *Journal of Sound and Vibration*, 40, 4, pp. 535-559
- Catalano, P., Wang, M., Iaccarino, G., Moin, P., 2003, "Numerical simulation of the flow around a circular cylinder at high Reynolds number," *International Journal of Heat and Fluid Flow*, v 24, n 4, pp. 463-469
- Cheung, J. C. K., Melbourne, W. H., 1983, "Turbulence effects on some aerodynamic parameters of a circular cylinder at supercritical Reynolds numbers," *Journal of Wind Engineering and Industrial Aerodynamics*, v 14, n 1-3, pp. 399-410
- Coutanceau, M., Bouard, R., 1977, "Experimental determination of the main features of the viscous flow in the wake of a circular cylinder in uniform translation. I. Steady flow," *Journal of Fluid Mechanics*, v 79, pt. 2, pp. 231-256
- Davidson, P. A., 2004, Turbulence, Oxford University
- Davis, R. S., 1992, "Equation for the determination of the density of moist air (1981/91)," *Metrologia*, v 29, n 1, pp. 67-70



Delany, N. K., Sorensen, N. E., 1953, "Low-speed Drag of cylinders of various shapes," National Advisory Committee for Aeronautics, Technical Notes, 22 pages

Dyban, Y. P., Epik, E. Ya., Kozlova, L. G., 1974, "Effect of free stream turbulence on the flow past a circular cylinder," Fluid Mechanics-Soviet Research, v 3, No. 5, pp. 75-78

Fage, A., Warsap, J. H., 1929, "The effects of turbulence and surface roughness on the drag of a circular cylinder," Aeronautical Research Committee, Reports and Memoranda No. 1283

Farell, C., Blessmann, J., 1983, "On critical flow around smooth circular cylinders," Journal of Fluid Mechanics, v 136, pp. 375-391

Fox, T. A., 1992, "End plate interference effects on the aerodynamics of a circular cylinder in uniform flow," Aeronautical Journal, v 96, n 951, pp. 10-14

Fox, T. A., West, G. S., 1990, "On the use of end plates with circular cylinder," Experiments in Fluids, v 9, n 4, pp. 237-239

Güven, O., Farell, C., Patel, V. C., 1980, "Surface-roughness effects on the mean flow past circular cylinders," Journal of Fluid Mechanics, v 98, n 4, pp. 673-701

Imai, I., 1951, "Theory of bluff bodies," University of Maryland, Institute for Fluid Dynamics and Applied Mathematics, Technical Note - BN-104, 87 pages

Jones, G., Cinotta, J., Walker, R., 1969, "Aerodynamic forces on a stationary and oscillating circular at high Reynolds number," NACA TR R-300

Karniadakis, G. M., Triantafyllou, G. S., 1992, "Three-dimensional dynamics and transition to turbulence in the wake of bluff objects," Journal of Fluid Mechanics, v 238, pp. 1-30

Kiya, M., Suzuki, Y., Arie, M., Hagino, M., 1982, "A contribution to the free-stream turbulence effect on the flow past a circular cylinder," Journal of Fluid Mechanics, v 115, pp. 151-164

Ko, S. C., Graf, W. H., 1972, "Drag coefficient of cylinders in turbulent flow," ASCE Journal of the Hydraulic Division, v 98, n HY5, pp. 897-912

Kwok, K. C. S., 1986, "Turbulence effect on flow around circular cylinder," Journal of Engineering Mechanics, v 112, n 11, pp. 1181-1197

Kwon, T. S., Sung, H. J., Hyun, J. M., 1992, "Experimental investigation of uniform-shear flow past a circular cylinder," *Journal of Fluids Engineering*, v 114, n 3, pp. 457-460

Lee, S.-J., Lim, H.-C., Han, M., Lee, S.-S., 2005, "Flow control of circular cylinder with a V-grooved micro-riblet film," *Fluid Dynamics Research*, v 37, n 4, pp. 246-266

Liu, R., Ting, D.S.-K., Checkel, M. D., 2007, "Constant Reynolds number turbulence downstream of an orificed perforated plate," *Experimental Thermal and Fluid Science*, v 31, n 8, pp. 897-908

Maekawa, T., Mizuno, S. 1967, "Flow around the separation point and in the near-wake of a circular cylinder," *Physics of Fluids*, v 10, n 9, pp. 5184-5186

Moradian, N., Ting, D.S.-K., Cheng, S., 2009, "The effects of freestream turbulence on the drag coefficient of a sphere," *Experimental Thermal and Fluid Science*, v 33, n 3, pp. 460-471

Mulcahy, T. M., 1984, "Fluid forces on a rigid cylinder in turbulent cross flow," *American Society of Mechanical Engineers, Symposium on Flow-Induced Vibration, Winter Ann. Meeting, New Orleans*, pp. 15-28

Nishioka, M., Sato, H., 1974, "Measurements of velocity distributions in the wake of a circular cylinder at low Reynolds numbers," *Journal of Fluid Mechanics*, v 65, pt. 1, pp. 97-112

Norberg, C., 1985, "Interaction between freestream turbulence and vortex shedding for a single tube in cross-flow," *Journal of Wind Engineering and Industrial Aerodynamics*, v 23, n 1-3, pp. 501-514

Norberg, C., Sunden, B., 1987, "Turbulence and Reynolds number effects on the flow and fluid forces on a single cylinder in cross flow," *Journal of Fluids and Structures*, 1, pp. 337-357

Ohya, Y., 2004, "Drag of circular cylinders in the atmospheric turbulence," *Fluid Dynamics Research* 34, pp. 135-144

Relf, E. F., Simmons, L. F., 1925, "On the frequency of the eddies generated by the motion of circular cylinders through a fluid," *London, Edinburgh, and Dublin Philosophical Magazine and Journal of Science*, v 49, n 290, pp. 509-511

Ribner, H. S., Etkin, E. T., 1958, "Canadian Research in Aerodynamic Noise," University of Toronto, Institute of Aerophysics, U.T.I.A. Review 13, 17 pages

Richter, A., Naudascher, E., 1976, "Fluctuating forces on a rigid circular cylinder in confined flow," *Journal of Fluid Mechanics*, v 78, pt. 3, pp. 561-576

Roshko, A., 1961, "Experiments on the flow past a circular cylinder at very high Reynolds number," *Journal of Fluid Mechanics*, v 10, pp. 345-356

Sadeh, W. Z., Saharon, D. B., 1982, "Turbulence Effect on crossflow around a circular cylinder at subcritical Reynolds Numbers," NASA Contractor Report, No. 3622

Sanitjai, S., Goldstein, R. J., 2001, "Effect of free stream turbulence on local mass transfer from a circular cylinder," *International Journal of Heat and Fluid Flow*, 44, pp. 2863-2875

Savkar, S. D., So, R. M. C., Litzinger, T. A., 1980, "Fluctuating lift and drag forces induced on large span bluff bodies in a turbulent cross flow," American Society of Mechanical Engineers, Heat Transfer Division, (Publication) HTD, v 9, pp. 19-26

Schlichting, H., 1979, Boundary Layer Theory, McGraw-Hill

So, R. M. C., Savkar, S. D., 1981, "Buffeting forces on rigid circular cylinders in cross flows," *Journal of Fluid Mechanics*, v 105, pp. 397-428

Stansby, P. K., 1974, "The effects of end plates on the base pressure coefficient of a circular cylinder," *Aeronautical Journal*, v 78, pp. 36-37

Sumner, D., Akosile, O. O., 2003, "On uniform planar shear flow around a circular cylinder at subcritical Reynolds number," *Journal of Fluids and Structures*, v 18, n 3-4, pp. 441-454

Surry, D., 1972, "Some effects of intense turbulence on the aerodynamics of a circular cylinder at subcritical Reynolds number," *Journal of Fluid Mechanics*, v 52, pp. 543-563

Szepessy, S., 1993, "On the control of circular cylinder flow by end plates," *European Journal of Mechanics, B/Fluids*, v 12, n 2, pp. 217-244

Szepessy, S., Bearman, P. W., 1992, "Aspect ratio and end plate effects on vortex shedding from a circular cylinder," *Journal of Fluid Mechanics*, v 234, pp. 191-217

Taneda, S., 1956, "Experimental investigation of the wake behind cylinders and plates at low Reynolds numbers," *Journal of the Physical Society of Japan*, v 11, n 3, pp. 302-307

Taneda, S., 1963, "The stability of two-dimensional laminar wakes at low Reynolds numbers," *Journal of the Physical Society of Japan*, v 18, n 2, pp. 288-296

Tennekes, H., Lumley, J. L., 1972, A First Course in Turbulence, The MIT Press Cambridge, Massachusetts, and London, England

Thoman, D. C., Szewczyk, A. A., 1969, "Time-dependent viscous flow over a circular cylinder," *Physics of Fluids*, pt. II, pp. 76-86

Tritton, D. T., 1959, "Experiments on flow past circular cylinder at low Reynolds number," *Journal of Fluid Mechanics*, v 6, pt. 4, pp. 547-567

Vronskaya, L. P., Taganov, G. I., 1979, "Experimental study of the drag of circular cylinders of high Aspect Ratio at  $Re \ll 1$ ," *Fluid Mechanics-Soviet Research*, v 8, No. 1, pp. 53-59

Wen, C.-Y., Yeh, C.-L., Wang, M.-J., Lin, C.-Y., 2004, "On the drag of two-dimensional flow about a circular cylinder," *Physics of Fluids*, v 16, n 10, pp. 3828-3831

West, G.S., Apelt, C. J., 1982, "The effects of the tunnel blockage and aspect ratio on the mean flow past a circular cylinder with Reynolds number between  $10^4$  and  $10^5$ ," *Journal of Fluid Mechanics*, v 114, pp. 361-377

Wieselsberger, C., 1922, "New data on the laws of fluid resistance," National Advisory Committee For Aeronautics, Technical Note No. 84, Translated from *Physikalische Zeitschrift*, v 22, pp. 321-328

Yeboah, E. N., Rahai, H. R., LaRue, J. C., 1997, "The effects of external turbulence on mean pressure distribution, drag coefficient, and wake characteristics of smooth cylinders," ASME Fluids Engineering Division Summer Meeting, FEDSM'97-3167, 6 pages

Zdravkovich, M. M., 1997, Flow Around Circular Cylinders, Oxford University Press

Zhang, H.-Q., Fey U., Noack, B. R., Konig, M., Eckelmann, H., 1995, "On the transition of the cylinder wake," *Physics of Fluids*, v 7, n 4, pp. 779-794

## APPENDIX A: MatLab Programs

### A.1 Program to calculate the integral length scale

```
clc
clear all;
%% #####GIVE INPUTS HERE
sample=10000000;
gain=1;
offset=0;
% Calibration Coefficients
c0=-34.048351;
c1=83.328880;
c2=-68.661018;
c3=19.041656;
c4=0.000002;
cutoff=0.000013;
sampling_frequency=80000;
imax=1;    % Number of Horizontal Traversing Point
jmax=3;    % Number of Vertical Traversing Point

%% #####INPUTS ENDS HERE#####

for horizontal=1:imax
    if (horizontal < 10 )
        HH=[int2str(0) int2str(horizontal)];
    else
        HH=[int2str(horizontal)];
    end

    for vertical=1:jmax
        if (vertical < 10 )
            VV=[int2str(0) int2str(vertical)];
        else
            VV=[int2str(vertical)];
        end
        sL=[int2str(1) HH VV];
        disp('Reading file');
        s=[sL '.txt']

        raw=load (s);

        E=raw(1:sample,1);
        E=E/4095*10/gain+offset;
        U=c0+c1*E.^1+c2*E.^2+c3*E.^3+c4*E.^4;
        %%%%%%%%%%%%%%%%%%%%%%%%%%%%%%%%%%%%%%%%%%%%%%%%%%%%%%%%%%%%%%%%%%%%%%%%%
        umean(horizontal,vertical)=mean(U);
        urms(horizontal, vertical)=std(U);
        tu(horizontal,vertical)=100*std(U)/mean(U);
        length_n = 1; flag=0;          % Initialising
        row1=0; row2=0;                % Initialising
        mean_velocity=umean(horizontal,vertical)
        u_inst = U-mean_velocity;
        u_rms= mean( u_inst.^2 );
```

```

for n=0:sample-1,
    % break;          % Can be switched ON when Integral length
    % calculation is NOT required.
    flag=0;
    for k=1:sample-n,
        flag = flag + (u_inst(k)*u_inst(k+n));
    end

    row2(n+1) = (flag/(sample-n))/(u_rms) ;

    %if (row2(n+1) < cutoff)
    if (row2(n+1) < cutoff)
        length_n = n;
        break;
    end

end

tau=(1:sample)/sampling_frequency;
T_scale=sum(row2)/sampling_frequency;

integral_length(horizontal,vertical)=T_scale*umean(horizontal,vertical)
plot(tau(1:length(row2)),row2);

end
end

```

## A.2 Program to calculate the air density

```

clc
clear
%function [ro] = air_density(t,hr,p)
% AIR_DENSITY calculates density of air
% Usage :[ro] = air_density(t,hr,p)
% Inputs:  t = ambient temperature (°C)
%          hr = relative humidity [%]
%          p = ambient pressure [Pa] (1000 mb = 1e5 Pa)
% Output:  ro = air density [kg/m3]
t=21.6
hr=67.5
p=99130
v=10.73
% Refs:
% 1)'Equation for the Determination of the Density of Moist Air' P.
Giacomo Metrologia 18, 33-40 (1982)
% 2)'Equation for the Determination of the Density of Moist Air' R. S.
Davis Metrologia 29, 67-70 (1992)
%% ver 1.0 06/10/2006 Jose Luis Prego Borges (Sensor & System
Group, Universitat Politecnica de Catalunya)
% ver 1.1 05-Feb-2007 Richard Signell (rsignell@usgs.gov)
Vectorized

%-----
T0 = 273.16;          % Triple point of water (aprox. 0°C)
T = T0 + t;          % Ambient temperature in °Kelvin

```

```

%-----
% 1) Coefficients values

R = 8.314510;           % Molar ideal gas constant [J/(mol.°K)]
Mv = 18.015*10^-3;     % Molar mass of water vapour [kg/mol]
Ma = 28.9635*10^-3;    % Molar mass of dry air [kg/mol]

A = 1.2378847*10^-5;   % [°K^-2]
B = -1.9121316*10^-2; % [°K^-1]
C = 33.93711047;      %
D = -6.3431645*10^3;   % [°K]

a0 = 1.58123*10^-6;    % [°K/Pa]
a1 = -2.9331*10^-8;    % [1/Pa]
a2 = 1.1043*10^-10;   % [1/(°K.Pa)]
b0 = 5.707*10^-6;     % [°K/Pa]
b1 = -2.051*10^-8;    % [1/Pa]
c0 = 1.9898*10^-4;    % [°K/Pa]
c1 = -2.376*10^-6;    % [1/Pa]
d = 1.83*10^-11;      % [°K^2/Pa^2]
e = -0.765*10^-8;     % [°K^2/Pa^2]

%-----
--
% 2) Calculation of the saturation vapour pressure at ambient
temperature, in [Pa]
psv = exp(A.*(T.^2) + B.*T + C + D./T); % [Pa]

%-----
% 3) Calculation of the enhancement factor at ambient temperature and
pressure
fpt = 1.00062 + (3.14*10^-8)*p + (5.6*10^-7)*(t.^2);

%-----
% 4) Calculation of the mole fraction of water vapour
xv = hr.*fpt.*psv.*(1./p)*(10^-2);

%-----
% 5) Calculation of the compressibility factor of air
Z = 1 - ((p./T).*(a0 + a1*t + a2*(t.^2) + (b0+b1*t).*xv +
(c0+c1*t).*(xv.^2))) + ((p.^2/T.^2).*(d + e.*(xv.^2)));

%-----
% 6) Final calculation of the air density in [kg/m^3]
ro = (p.*Ma./(Z.*R.*T)).*(1 - xv.*(1-Mv./Ma));
DP=(ro/2000)*v.^2

```

## **APPENDIX B: Data Acquisition Selection**

Finding the nearly optimum hot-wire anemometer sampling number and sampling frequency, was an important task of this study to ensure the accuracy of the results for all turbulence parameters.

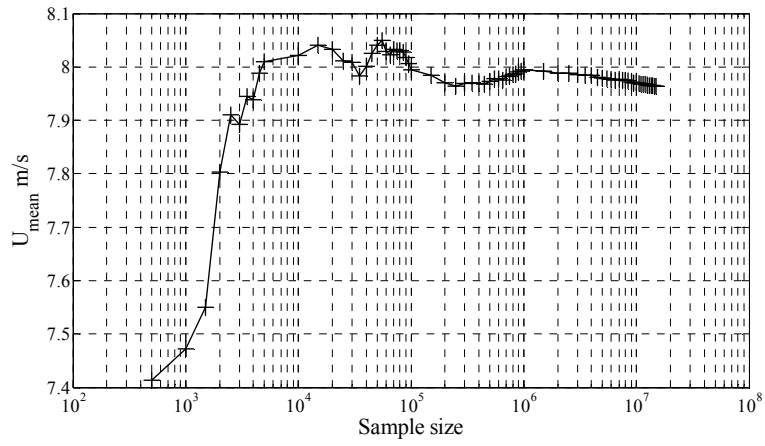
### **B.1 Sample number**

One of the important selections in the hot-wire anemometer measurement is the sample number value (the number of times the hot-wire repeats the reading in each location). This value should be selected with caution as the experiment time increases as the sample number value increases; on the other hand, the accuracy will be affected dramatically if the sample size is too small. This value was determined by an empirical approach in which the desired flow parameter was tested as a function of the sampling number. The minimum sample number was identified as the one beyond which the flow parameter concerned remains nearly constant. The mean velocity, root mean square value, turbulence intensity, and the integral length scale are plotted, versus the sample number as shown in Figures B1-B3. It is very clear that all the curves are nearly stable after a sample number equal to  $10^7$ , and this is the value used for all hot-wire measurements.

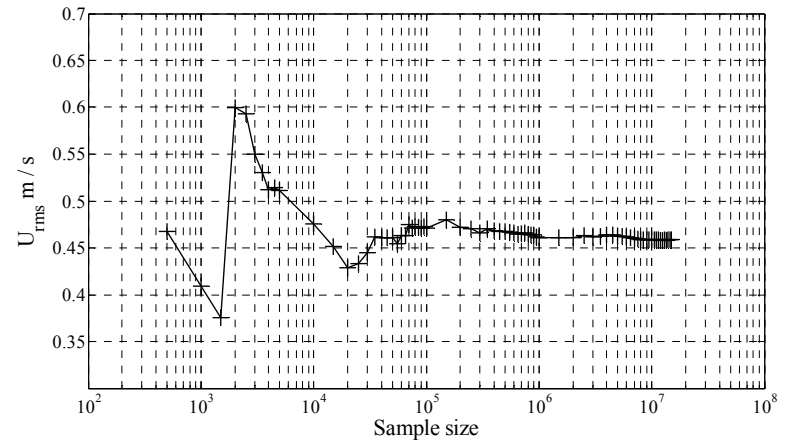
### **B.2 Sampling frequency**

The sampling frequency  $f_s$  is determined by the highest frequency presented in the analog signal, i.e., the cutoff frequency of the analog low-pass filter. In the current study, the low-pass filter was set at 30 kHz before digitization. Therefore, the sampling frequency  $f_s$  was set to 80 kHz which is more than twice the Nyquist frequency to avoid aliasing problems.

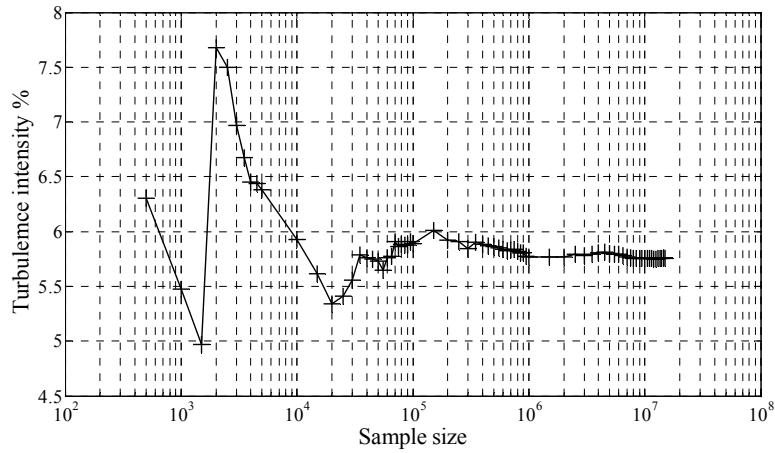




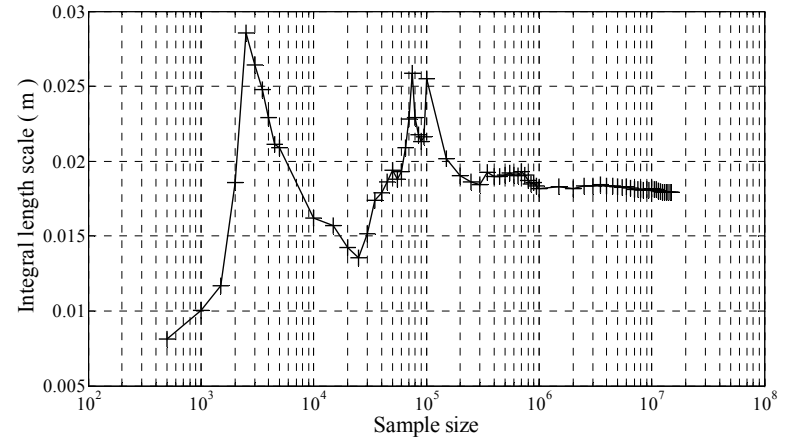
(a)  $U_{\text{mean}}$



(b)  $U_{\text{rms}}$

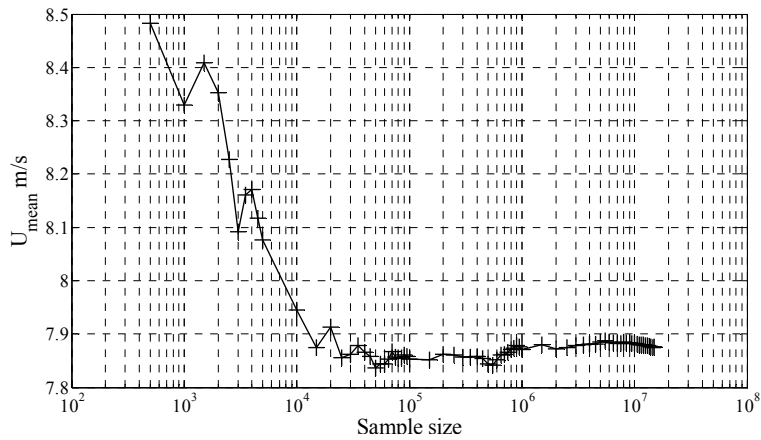


(c) Tu

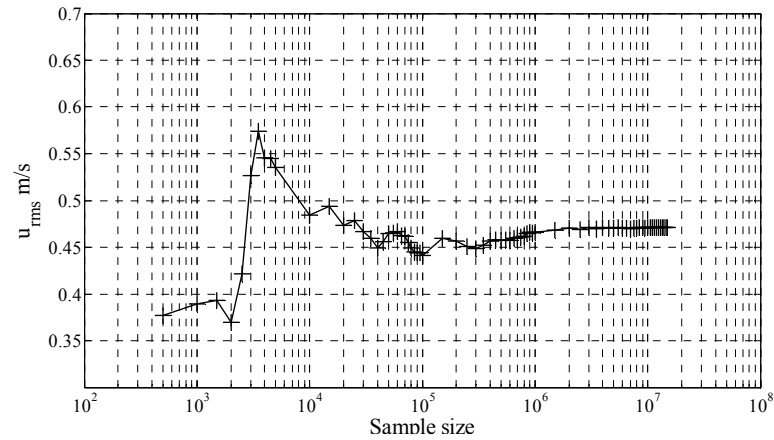


(d) Integral length scale ( $\Lambda$ )

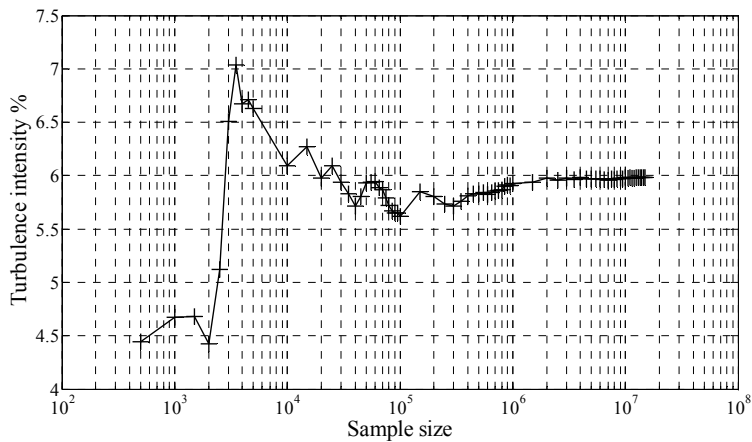
Figure B1 Sample size check for d25 plate located at  $20 x/d$  and  $U_0=8.1$  m/s (a)  $U_{\text{mean}}$  (b)  $U_{\text{rms}}$  (c) Tu % (d) Integral length scale ( $\Lambda$ )



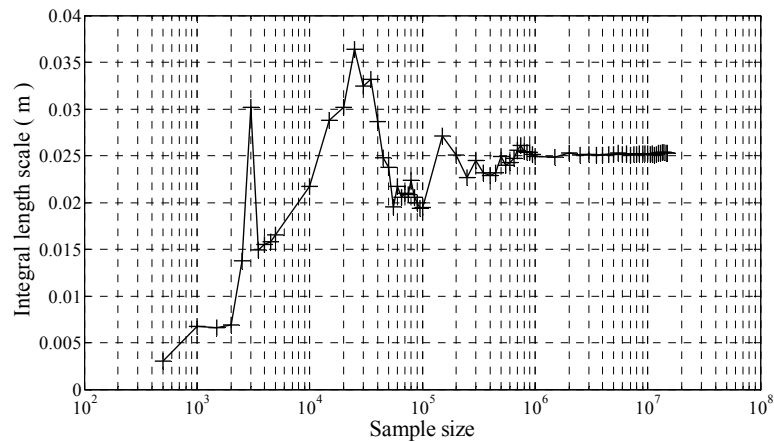
(a)  $U_{\text{mean}}$



(b)  $U_{\text{rms}}$

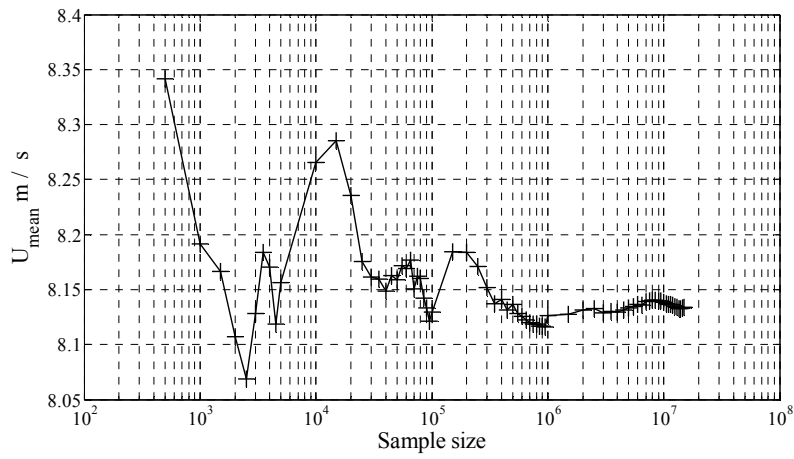


(c) Tu

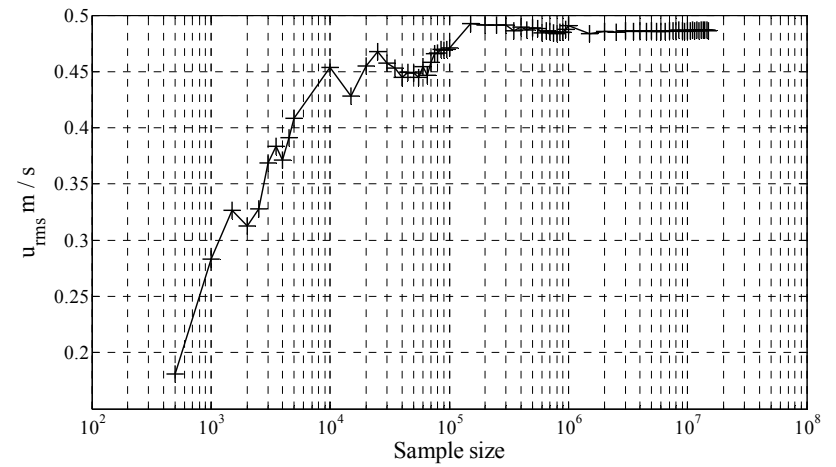


(d) Integral length scale ( $\Lambda$ )

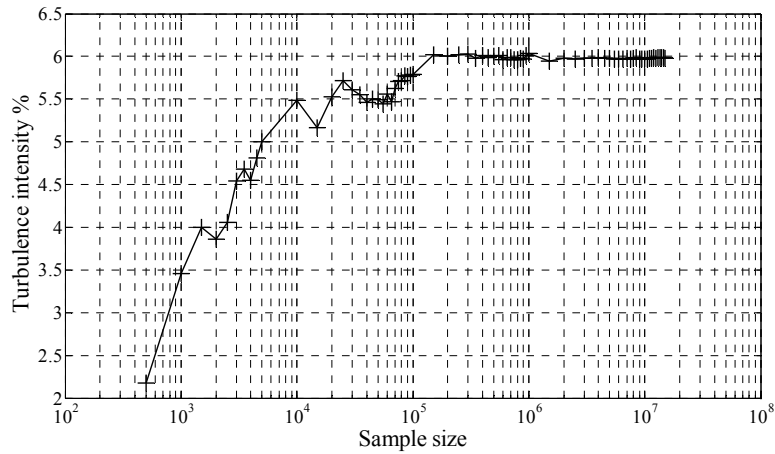
Figure B2 Sample size check for d37.5 plate located at  $20 x/d$  and  $U_0 = 8.1 \text{ m/s}$  (a)  $U_{\text{mean}}$  (b)  $U_{\text{rms}}$   
(c) Tu % (d) Integral length scale ( $\Lambda$ )



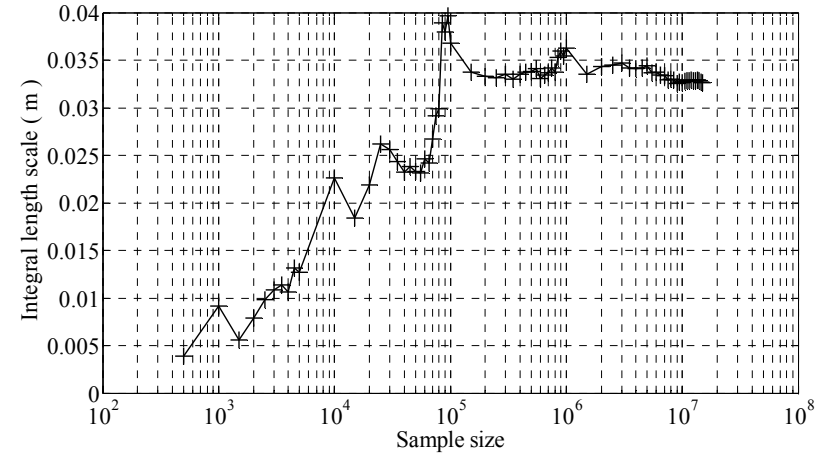
(a)  $U_{\text{mean}}$



(b)  $U_{\text{rms}}$



(c) Tu



(d) Integral length scale ( $\Lambda$ )

Figure B3 Sample size check for d50 plate located at 20 x/d and  $U_0 = 8.1$  m/s (a)  $U_{\text{mean}}$  (b)  $U_{\text{rms}}$  (c) Tu % (d) Integral length scale ( $\Lambda$ )

## APPENDIX C: Hot-wire Probe Calibration

The fully computer-controlled calibration system is intended for probe calibration and has an important role for accuracy and speed. It consists of a calibration Module (Dantec 90H10) to be placed in the Frame and a separate Flow Unit connected to the Calibration Module via a Cable. The normal pressurized air (6 to 8 bars) enters the Flow Unit through an external filter that filters away particles and oil. A Precision Regulator inside the Flow Unit ensures a stable input pressure to the Flow Control. The Flow Unit is able to set velocities from 0.5 m/s to 60 m/s through different replaceable area size nozzles located at the exit. To do a calibration, the sample project in the Dantec manual Vol. 1 is followed. To calibrate the hot-wire probe, the probe is installed near the exit of a jet. The Flow Unit has a low-turbulent free jet, the velocity of which is calculated on the basis of the pressure drop over its exit. It is performed by exposing the probe to a set of known velocities,  $U$ , and then record the voltages,  $E$ . A polynomial curve fit through the points ( $E$ ,  $U$ ) represents the transfer function to be used when converting data records from voltages into velocities. The acceptable linearization errors are less than 1%. Also, the system corrects the voltages  $E$  for temperature variations during calibration and gives five coefficients,  $C_0$ ,  $C_1$ ,  $C_2$ ,  $C_3$ , and  $C_4$  to find the correct velocity values,

$$U = C_0 + C_1E^1 + C_2E^2 + C_3E^3 + C_4E^4 \quad (C1)$$

## APPENDIX D: FFT for load cell output

### D.1 FFT MatLab program

```
%Frequency spectrum
clc;
clear all;
sample=10000; %Sample Size
NFFT=2^16;%NFFT=2^nextpow2(sample)
%Load Raw Data
Fs=1000;%sample frequency
E = load('10.txt');
Pyy=2*abs(fft(E(1:length(E)),NFFT))/NFFT;
f=Fs/NFFT*(0:NFFT/2);
plot(f(2:NFFT/2),Pyy(2:NFFT/2));
xlabel('Frequency, Hz');
ylabel('Amplitude');
axis([0 100 0 2])
```

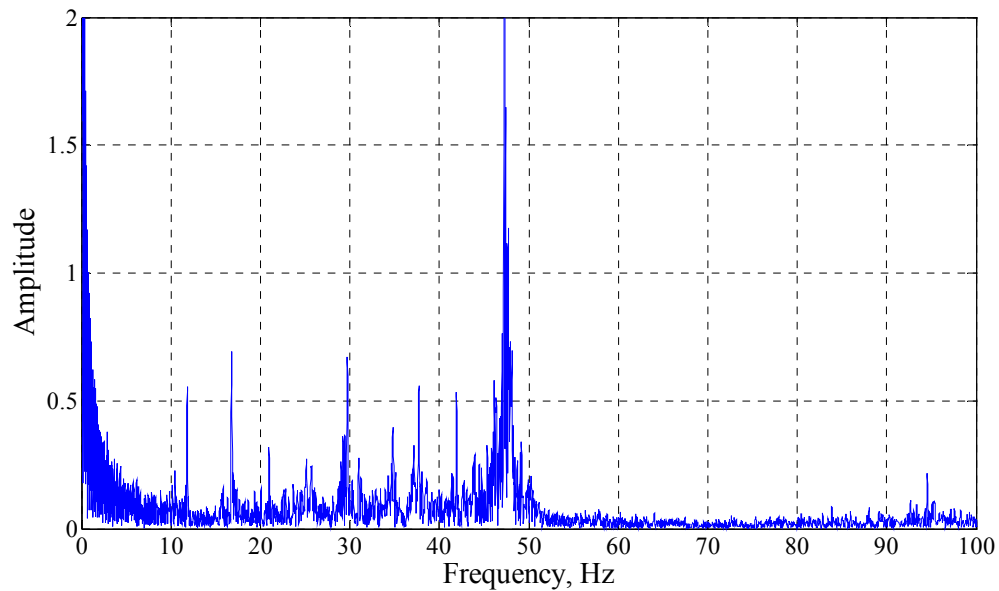


Figure D1 Frequency for 26.7 mm cylinder,  $Tu=5\%$ , and  $U_0=10.7$  m/s

## APPENDIX E: Taylor Microscale

The Taylor microscale is estimated as mentioned by Liu et al. [2007] as,

$$\lambda = \left( \frac{15 \times u_{rms}^2 \times \mu}{\left( \frac{dK}{dt} \right) \times \rho} \right)^{1/2} \quad (E.1)$$

Where K can be defined as,

$$K = B \left( t - \frac{X_0}{U} \right)^{-n} \quad (E.2)$$

By differentiating,

$$\frac{dK}{dt} = -n \times B_f \times \left( t - \frac{X_0}{U} \right)^{-n-1} \quad (E.3)$$

And,

$$X_0 = 7 \times M_s \quad (E.4)$$

The value of M can be found from Table E.1

Table E.1 Mesh size for the orificed perforated plates

Plate	$M_s$ ( mm )
d25	30
d37.5	45
d50	60

Liu et al. [2007] defined the curve fit coefficient  $B_f$  to be equal to 0.0209, and the power law decay  $n$  to be 1.012, for the same orificed perforated plates used in the current study.

For each plate location in (mm) and flow velocity in (m/s) the converted elapsing time can be found from this equation,

$$t = \frac{x}{U} \quad (E.5)$$

## APPENDIX F: Uncertainty Analysis

### F.1 Uncertainty in Reynolds number

The Reynolds number equation is:

$$\text{Re} = \frac{\rho \times U_0 \times D}{\mu} \quad (\text{F.1})$$

The absolute uncertainty in Re:

$$W_{\text{Re}} = \sqrt{\left(\frac{\partial \text{Re}}{\partial \rho} W_{\rho}\right)^2 + \left(\frac{\partial \text{Re}}{\partial U_0} W_{U_0}\right)^2 + \left(\frac{\partial \text{Re}}{\partial D} W_D\right)^2} \quad (\text{F.2})$$

where,

$$\frac{\partial \text{Re}}{\partial \rho} = \frac{U_0 \times D}{\mu} \quad (\text{F.3})$$

$$\frac{\partial \text{Re}}{\partial U_0} = \frac{\rho \times D}{\mu} \quad (\text{F.4})$$

$$\frac{\partial \text{Re}}{\partial D} = \frac{\rho \times U_0}{\mu} \quad (\text{F.5})$$

Thus after disregarding the uncertainty in  $\mu$ ,

$$W_{\text{Re}} = \sqrt{\left(\frac{U_0 \times D}{\mu} W_{\rho}\right)^2 + \left(\frac{\rho \times D}{\mu} W_{U_0}\right)^2 + \left(\frac{\rho \times U_0}{\mu} W_D\right)^2} \quad (\text{F.6})$$

To find the Reynolds number, first the uncertainty in air density should be calculated, the atmospheric temperature, pressure, and the relative humidity of the lab are measured by Kestrel 4500 weather meter every time before any experiment and the air density is considered according to that; the digital thermometer has a resolution of 0.1°C, the manual giving an accuracy of ±1°C. Thus the absolute uncertainty in temperature can be calculated by.

$$(W_T)_{\text{Instrument errors}} = \sqrt{(W_T)_{\text{Resolution}}^2 + (W_T)_{\text{Accuracy}}^2} \quad (\text{F.7})$$

$$W_T = \sqrt{\left(\frac{0.1}{2}\right)^2 + (1)^2} \approx 1^\circ \text{C} = 1^\circ \text{K} \quad (\text{F.8})$$

Kestrel 4500 pressure resolution is 0.01inHg, and the accuracy is ±0.05 inHg. The absolute uncertainty can be calculated as,

$$(W_P)_{\text{Instrument errors}} = \sqrt{(W_P)_{\text{Resolution}}^2 + (W_P)_{\text{Accuracy}}^2} \quad (\text{F.9})$$

$$(W_p)_{\text{Instrument errors}} = \sqrt{\left(\frac{0.01}{2}\right)^2 + (0.05)^2} = 0.0503 \text{ inHg} \quad (\text{F.10})$$

$$W_p = 0.0503 \text{ inHg} = 170.33 \text{ Pa} \quad \text{Where } 29.92126 \text{ inHg} = 101.325 \text{ kPa}$$

Kestrel 4500 relative humidity Resolution is 0.1 and the Accuracy is 3.0%RH. In this study the equation derived by Davis [1992] is used to find the density of the moist air, However the small changes of the relative humidity in this equation is unpronounced, for this reason the uncertainty for the relative humidity will not be considered.

The absolute uncertainty in air density can be calculated from the ideal gas equation which is  $P = \rho RT$ . After neglecting the uncertainty of the gas constant, R:

$$W_p = \sqrt{\left(\frac{\partial \rho}{\partial P} W_p\right)^2 + \left(\frac{\partial \rho}{\partial T} W_T\right)^2} = \sqrt{\left(\frac{W_p}{RT}\right)^2 + \left(-\frac{P \times W_T}{R \times T^2}\right)^2} \quad (\text{F.11})$$

where,

$$\frac{\partial \rho}{\partial P} = \frac{1}{R \times T} \quad (\text{F.12})$$

$$\frac{\partial \rho}{\partial T} = -\frac{P}{R \times T^2} \quad (\text{F.13})$$

The universal gas constant for air is equal to  $287.05 \frac{\text{J}}{\text{kg} \times \text{K}}$  and the normal value of

the atmospheric pressure in the Lab location is around 99.430 kPa, and the temperature is around 22 °C which is 295 °K. Thus,

$$W_p = \sqrt{\left(\frac{W_p}{RT}\right)^2 + \left(-\frac{P \times W_T}{R \times T^2}\right)^2} = \sqrt{\left(\frac{170.33}{287.05 \times 295}\right)^2 + \left(\frac{99430 \times 1}{287.05 \times 295^2}\right)^2} \quad (\text{F.14})$$

$$W_p = \sqrt{(0.00201)^2 + (0.00398)^2} = 0.00446 \text{ Kg/m}^3 \quad (\text{F.15})$$

The free stream velocity in the wind tunnel is measured by Pitot-static tube. The mean flow velocity is calculated by:

$$\Delta P = \frac{1}{2} \rho_{\text{air}} U^2 \quad (\text{F.16})$$

Equation F.16 is changed to the following form:

$$U_0 = \sqrt{\frac{2 \times \Delta P}{\rho_{\text{air}}}} \quad (\text{F.17})$$



The absolute uncertainty in the Pitot static tube velocity obtained from,

$$W_{U_0} = \sqrt{\left(\frac{\partial U_0}{\partial \Delta P} W_{\Delta P}\right)^2 + \left(\frac{\partial U_0}{\partial \rho} W_{\rho}\right)^2} = \sqrt{\left(\sqrt{\frac{\rho}{2 \times \Delta P}} \times \frac{W_{\Delta P}}{\rho}\right)^2 + \left(\sqrt{\frac{\rho}{2 \times \Delta P}} \times \left(-\frac{\Delta P \times W_{\rho}}{\rho^2}\right)\right)^2} \quad (\text{F.18})$$

where,

$$\frac{\partial U_0}{\partial \Delta P} = \sqrt{\frac{\rho}{2 \times \Delta P}} \times \frac{W_{\Delta P}}{\rho} \quad (\text{F.19})$$

$$\frac{\partial U_0}{\partial \rho} = \sqrt{\frac{\rho}{2 \times \Delta P}} \times \left(-\frac{\Delta P \times W_{\rho}}{\rho^2}\right) \quad (\text{F.20})$$

Manometer hysteresis is  $\pm 0.1\%$  of the full scale (0.249kPa), Manometer repeatability is found by measuring the same point more than 10 times for the same velocity and it is found to be 0.00005kPa, and the student-t distribution can be considered as 2 as an engineering approximation. The resolution is 0.0001kPa, considering the minimum and maximum reading in this experiment which is 0.0026kPa, and 0.0677 kPa, respectively.

The absolute uncertainty is,

$$(W_{\Delta P})_{\text{Instrument errors}} = \sqrt{(W_{\Delta P})_{\text{Resolution}}^2 + (W_{\Delta P})_{\text{Hysteresis}}^2} \quad (\text{F.21})$$

$$(W_{\Delta P})_{\text{Instrument errors}} = \sqrt{\left(\frac{0.0001}{2}\right)^2 + (0.001 \times 0.249)^2} = 0.000254\text{kPa} \quad (\text{F.22})$$

$$(W_{\Delta P})_{\text{Precision errors}} = \sqrt{(t_{v,95} \times P_R)^2} = (2 \times 0.00005) = 0.0001\text{kPa} \quad (\text{F.23})$$

$$W_{\Delta P} = \sqrt{(W_{\Delta P})_{\text{Instrument errors}}^2 + (W_{\Delta P})_{\text{Precision errors}}^2} \quad (\text{F.24})$$

$$W_{\Delta P} = \sqrt{(0.000254)^2 + (0.0001)^2} = 0.000273\text{kPa} \quad (\text{F.25})$$

For  $\Delta P = 0.0026 \text{ kPa}$ , this is the smallest manometer reading in the current study,

$$W_{U_0} = \sqrt{\left(\sqrt{\frac{1.16}{2 \times 2.6}} \times \frac{0.273}{1.16}\right)^2 + \left(\sqrt{\frac{1.16}{2 \times 2.6}} \times \left(-\frac{2.6 \times 0.00446}{1.16^2}\right)\right)^2} \quad (\text{F.26})$$

$$W_{U_0} = \sqrt{(0.1112)^2 + (0.00407)^2} = 0.1113 \text{ m/s} \quad (\text{F.27})$$

For  $\Delta P = 0.0174 \text{ kPa}$ ,

$$W_{U_0} = \sqrt{\left(\sqrt{\frac{1.16}{2 \times 17.4} \times \frac{0.273}{1.16}}\right)^2 + \left(\sqrt{\frac{1.16}{2 \times 17.4} \times \left(-\frac{17.4 \times 0.00446}{1.16^2}\right)}\right)^2} \quad (\text{F.28})$$

$$W_{U_0} = \sqrt{(0.0429)^2 + (0.00105)^2} = 0.0442 \text{ m/s} \quad (\text{F.29})$$

For  $\Delta P = 0.0677 \text{ kPa}$ , this is the largest manometer reading in the current study,

$$W_{U_0} = \sqrt{\left(\sqrt{\frac{1.16}{2 \times 67.7} \times \frac{0.273}{1.16}}\right)^2 + \left(\sqrt{\frac{1.16}{2 \times 67.7} \times \left(-\frac{67.7 \times 0.00446}{1.16^2}\right)}\right)^2} \quad (\text{F.30})$$

$$W_{U_0} = \sqrt{(0.0218)^2 + (0.02077)^2} = 0.0301 \text{ m/s} \quad (\text{F.31})$$

The diameter of the cylinder is measured with a digital caliper (Mitutoyo 500-171). The caliper has a resolution of 0.01 mm and an accuracy of  $\pm 0.025 \text{ mm}$ . The measurement showed that the cylinders are not completely perfect. Their maximum inaccuracy is 0.35 mm. The absolute uncertainty in cylinder diameter,

$$(W_D)_{\text{Instrument errors}} = \sqrt{(W_D)_{\text{Resolution}}^2 + (W_D)_{\text{Accuracy}}^2} \quad (\text{F.32})$$

$$(W_D)_{\text{Instrument errors}} = \sqrt{\left(\frac{0.01}{2}\right)^2 + (0.025)^2} = 0.0255 \text{ mm} \quad (\text{F.33})$$

$$(W_D)_{\text{Diameter imperfection}} = 0.35 \text{ mm} \quad (\text{F.34})$$

$$W_D = \sqrt{(W_D)_{\text{Instrument errors}}^2 + (W_D)_{\text{Diameter imperfection}}^2} \quad (\text{F.35})$$

$$W_D = \sqrt{(0.0255)^2 + (0.35)^2} = 0.36 \text{ mm} \quad (\text{F.36})$$

where,

$$\mu = 1.82 \times 10^{-5} \frac{\text{kg}}{\text{m} \times \text{s}} \text{ at } 20^\circ \text{C}$$

For  $\text{Re}=6450$

$$W_{\text{Re}} = \sqrt{\left(\frac{2.1 \times 0.0485}{1.82 \times 10^{-5}} \times 0.00446\right)^2 + \left(\frac{1.16 \times 0.0485}{1.82 \times 10^{-5}} \times 0.1113\right)^2 + \left(\frac{1.16 \times 2.1}{1.82 \times 10^{-5}} \times 0.00036\right)^2} \quad (\text{F.37})$$

$$W_{\text{Re}} = \sqrt{(24.95)^2 + (344.05)^2 + (48.18)^2} = 348.3 \quad (\text{F.38})$$

For Re=18200,

$$W_{Re} = \sqrt{\left(\frac{10.73 \times 0.0267}{1.82 \times 10^{-5}} \times 0.00446\right)^2 + \left(\frac{1.16 \times 0.0267}{1.82 \times 10^{-5}} \times 0.0301\right)^2 + \left(\frac{1.16 \times 10.73}{1.82 \times 10^{-5}} \times 0.00036\right)^2} \quad (\text{F.39})$$

$$W_{Re} = \sqrt{(70.2)^2 + (51.22)^2 + (246.2)^2} = 261.08 \quad (\text{F.40})$$

## F.2 Uncertainty in drag coefficient

The drag coefficient  $C_d$  is calculated by:

$$C_d = \frac{F_D}{\frac{1}{2} \rho \times U_0^2 (D \times L)} \quad (\text{F.41})$$

The absolute uncertainty in drag coefficient can be found from

$$W_{C_d} = \sqrt{\left(\frac{\partial C_d}{\partial F_D} \times W_{F_D}\right)^2 + \left(\frac{\partial C_d}{\partial \rho} \times W_{\rho}\right)^2 + \left(\frac{\partial C_d}{\partial U_0} \times W_{U_0}\right)^2 + \left(\frac{\partial C_d}{\partial D} \times W_D\right)^2 + \left(\frac{\partial C_d}{\partial L} \times W_L\right)^2} \quad (\text{F.42})$$

where,

$$\frac{\partial C_d}{\partial F_D} = \frac{2}{\rho \times U_0^2 \times D \times L} \quad (\text{F.43})$$

$$\frac{\partial C_d}{\partial \rho} = -\frac{2 \times F_D}{\rho^2 \times U_0^2 \times D \times L} \quad (\text{F.44})$$

$$\frac{\partial C_d}{\partial U_0} = -\frac{4 \times F_D}{\rho \times U_0^3 \times D \times L} \quad (\text{F.45})$$

$$\frac{\partial C_d}{\partial D} = -\frac{2 \times F_D}{\rho \times U_0^2 \times D^2 \times L} \quad (\text{F.46})$$

$$\frac{\partial C_d}{\partial L} = -\frac{2 \times F_D}{\rho \times U_0^2 \times D \times L^2} \quad (\text{F.47})$$

Substituting Equation (F.41), (F.42), (F.43), (F.44), and (F.45), into Equation (F.40),

$$W_{C_d} = \sqrt{\left(\frac{2}{\rho \times U_0^2 \times D \times L} \times W_{F_D}\right)^2 + \left(-\frac{2 \times F_D}{\rho^2 \times U_0^2 \times D \times L} \times W_\rho\right)^2 + \left(-\frac{4 \times F_D}{\rho \times U_0^3 \times D \times L} \times W_{U_0}\right)^2 + \left(\frac{2 \times F_D}{\rho \times U_0^2 \times D^2 \times L} \times W_D\right)^2 + \left(-\frac{2 \times F_D}{\rho \times U_0^2 \times D \times L^2} \times W_L\right)^2}$$

(F.48)

For the cylinder length (from the long caliper manual) the resolution is 0.01 mm, the repeatability is 0.01 mm, and the accuracy is:

$$(0.02 + 0.00005 \times L) = (0.02 + 0.00005 \times 657) = 0.052 \text{ mm}$$

The absolute uncertainty is,

$$(W_L)_{\text{Instrument errors}} = \sqrt{(W_L)_{\text{Resolution}}^2 + (W_L)_{\text{Accuracy}}^2}$$

(F.49)

$$(W_L)_{\text{Instrument errors}} = \sqrt{\left(\frac{0.01}{2}\right)^2 + (0.052)^2} = 0.0522 \text{ mm}$$

(F.50)

$$(W_L) = 0.0522 \text{ mm}$$

The load cell Calibration Accuracy Report gives the full-scale error value for Fx which is our concern is 0.04% from the full scale and the Resolution for this load cell is 1/160 N

The absolute uncertainty in drag force is equal to,

$$(W_{F_D})_{\text{Instrument errors}} = \sqrt{(W_{F_D})_{\text{Resolution}}^2 + (W_{F_D})_{\text{Accuracy}}^2}$$

(F.51)

$$(W_{F_D})_{\text{Instrument errors}} = \sqrt{\left(\frac{1}{160}\right)^2 + (0.0004 \times 32)^2} = 0.0142 \text{ N}$$

(F.52)

A number of experiment were done to check the repeatability of the load cell and it is found to be 0.01N, and the student-t distribution can be considered as 2 as an engineering approximation,

$$(W_{F_D})_{\text{Precision errors}} = \sqrt{(t_{v,95} \times P_R)^2} = (2 \times 0.01) = 0.02 \text{ N}$$

(F.53)

$$(W_{F_D}) = \sqrt{(W_{F_D})_{\text{Instrument errors}}^2 + (W_{F_D})_{\text{Precision errors}}^2} = \sqrt{(0.0142)^2 + (0.02)^2} = 0.0245 \text{ N}$$

(F.54)

For

$$U_0 = 2.1 \text{ m/s}, \rho = 1.16 \text{ kg / m}^3, D = 0.0485 \text{ m}, F_D = 0.092 \text{ N}, L = 0.654 \text{ m}, \text{Re} = 6450$$

$$W_{F_D} = 0.0245\text{N}$$

$$W_{\rho} = 0.00446\text{ kg / m}^3$$

$$W_{U_0} = 0.1113\text{ m/s}$$

$$W_D = 0.00036\text{ m}$$

$$W_L = 0.0000522\text{ m}$$

$$W_{C_d} = \sqrt{\left(\frac{2}{1.16 \times 2.1^2 \times 0.0485 \times 0.654} \times 0.0245\right)^2 + \left(-\frac{2 \times 0.092}{1.16^2 \times 2.1^2 \times 0.0485 \times 0.654} \times 0.00446\right)^2 + \left(-\frac{4 \times 0.092}{1.16 \times 2.1^3 \times 0.0485 \times 0.654} \times 0.1113\right)^2 + \left(\frac{2 \times 0.092}{1.16 \times 2.1^2 \times 0.0485^2 \times 0.654} \times 0.00036\right)^2 + \left(-\frac{2 \times 0.092}{1.16 \times 2.1^2 \times 0.0485 \times 0.654^2} \times 0.0000522\right)^2}$$

(F.55)

$$W_{C_d} = \sqrt{(0.302)^2 + (0.00435)^2 + (0.12)^2 + (0.00841)^2 + (0.0000905)^2}$$

(F.56)

$$W_{C_d} = 0.32$$

For

$$U_0=5.51\text{ m/s}, \rho = 1.16\text{ kg / m}^3, D=0.0336\text{ m}, F_D = 0.452\text{ N}, L=0.654\text{m}, \text{Re}=11750$$

$$W_{F_D} = 0.0245\text{N}$$

$$W_{\rho} = 0.00446\text{ kg / m}^3$$

$$W_{U_0} = 0.0442\text{ m/s}$$

$$W_D = 0.00036\text{ m}$$

$$W_L = 0.0000522\text{ m}$$

$$W_{C_d} = \sqrt{\left(\frac{2}{1.16 \times 5.51^2 \times 0.0336 \times 0.654} \times 0.0245\right)^2 + \left(-\frac{2 \times 0.452}{1.16^2 \times 5.51^2 \times 0.0336 \times 0.654} \times 0.00446\right)^2 + \left(-\frac{4 \times 0.452}{1.16 \times 5.51^3 \times 0.0336 \times 0.654} \times 0.0442\right)^2 + \left(\frac{2 \times 0.452}{1.16 \times 5.51^2 \times 0.0336^2 \times 0.654} \times 0.00036\right)^2 + \left(-\frac{2 \times 0.452}{1.16 \times 5.51^2 \times 0.0336 \times 0.654^2} \times 0.0000522\right)^2}$$

(F.57)

$$W_{C_d} = \sqrt{(0.063)^2 + (0.00449)^2 + (0.0187)^2 + (0.0125)^2 + (0.0000932)^2}$$

(F.58)

$$W_{C_d} = 0.067$$

$$U_0 = 10.7 \text{ m/s}, \rho = 1.16 \text{ Kg / m}^3, D = 0.026.7 \text{ m}, F_D = 1.552 \text{ N}, L = 0.654 \text{ m}, \text{Re} = 18200$$

$$W_{F_D} = 0.0245 \text{ N}$$

$$W_{\rho} = 0.00446 \text{ kg / m}^3$$

$$W_{U_0} = 0.0301 \text{ m/s}$$

$$W_D = 0.00036 \text{ m}$$

$$W_L = 0.0000522 \text{ m}$$

$$W_{C_d} = \sqrt{\left(\frac{2}{1.16 \times 10.73^2 \times 0.0267 \times 0.654} \times 0.0245\right)^2 + \left(-\frac{2 \times 1.552}{1.16^2 \times 10.73^2 \times 0.0267 \times 0.654} \times 0.00446\right)^2 + \left(-\frac{4 \times 1.552}{1.16 \times 10.73^3 \times 0.0267 \times 0.654} \times 0.0301\right)^2 + \left(\frac{2 \times 1.552}{1.16 \times 10.73^2 \times 0.0267^2 \times 0.654} \times 0.00036\right)^2 + \left(-\frac{2 \times 1.552}{1.16 \times 10.73^2 \times 0.0267 \times 0.654^2} \times 0.0000522\right)^2}$$

(F.59)

$$W_{C_d} = \sqrt{(0.021)^2 + (0.00512)^2 + (0.00747)^2 + (0.0179)^2 + (0.0001062)^2}$$

(F.60)

$$W_{C_d} = 0.03$$

### F.3 Uncertainty in turbulence intensity

The turbulence intensity, Tu is calculated as:

$$Tu\% = \frac{u_{rms}}{\bar{U}} \times 100 \quad (F.61)$$

The uncertainty of the turbulence intensity can be found from,

$$W_{Tu} = \sqrt{\left(\frac{\partial Tu}{\partial u_{rms}} \times W_{u_{rms}}\right)^2 + \left(\frac{\partial Tu}{\partial \bar{U}} \times W_{\bar{U}}\right)^2} \quad (F.62)$$

But,

$$\frac{\partial Tu}{\partial u_{rms}} = \frac{100}{\bar{U}} \quad (F.63)$$

$$\frac{\partial Tu}{\partial \bar{U}} = -\frac{100 \times u_{rms}}{(\bar{U})^2} \quad (F.64)$$

Thus,

$$W_{Tu} = \sqrt{\left(\frac{100}{\bar{U}} \times W_{u_{rms}}\right)^2 + \left(-\frac{100 \times u_{rms}}{(\bar{U})^2} \times W_{\bar{U}}\right)^2} \quad (F.65)$$

The uncertainty the turbulence intensity depends on the uncertainty of  $U_i$ ,  $\bar{U}$  and  $u$ . for this reason the uncertainty in these parameters should found first.

The total relative uncertainty in the velocity measured by the hot-wire probe is due to hot-wire calibration and data acquisition,

$$U_{eff} = C_0 + C_1 \times E_i + C_2 \times E_i^2 + C_3 \times E_i^3 + C_4 \times E_i^4 \quad (F.66)$$

By differentiating,

$$\frac{dU_{eff}}{dE_i} = C_1 + C_2 \times E_i + C_3 \times E_i^2 + C_4 E_i^3 \quad (F.67)$$

The uncertainty from the digitized hot-wire anemometer output is  $\pm 0.5$  of the least significant bit, which, for the 12 bits A/D with an input range set as 0 to 10V, [Dantec Dynamics Manual, 2000]:

$$W_E = \frac{0.5 \times 10}{2^{12}} = 0.0012V \quad (F.68)$$

The uncertainty in digitizing the hot-wire output,

$$(W_{U_{\text{eff}}})_{\text{Digitalize}} = \frac{W_E}{U_{\text{eff}}} \times \frac{dU_{\text{eff}}}{dE_i} \quad (\text{F.69})$$

$$(W_{U_{\text{eff}}})_{\text{Digitalize}} = \frac{0.0012}{U_{\text{eff}}} \times (C_1 + C_2 \times E_i + C_3 \times E_i^2 + C_4 \times E_i^3) \quad (\text{F.70})$$

$$(W_{U_{\text{eff}}})_{\text{Data aquisition}} = \sqrt{(W_{U_{\text{eff}}})_{\text{Digitalize}}^2 + (W_{U_{\text{eff}}})_{\text{Prob Position}}^2} \quad (\text{F.71})$$

From the Dantec manual the uncertainty in probe position is defined as,

$$(W_{U_{\text{eff}}})_{\text{Probe position}} = \frac{1}{\sqrt{3}} (1 - \cos \alpha) \quad (\text{F.72})$$

The uncertainty is equal to 0.000087 m/s when an error of 1° in the aligning hot-wire angle  $\alpha$ . This uncertainty is very small and could be neglected.

Then the uncertainty in data acquisition will equal to digitized of the hot-wire output.

$$(W_{U_{\text{eff}}})_{\text{Data aquisition}} = \sqrt{(W_{U_{\text{eff}}})_{\text{Digitalize}}^2} \quad (\text{F.73})$$

Then,

$$W_{U_{\text{eff}}} = \sqrt{(W_{U_{\text{eff}}})_{\text{Calibration}}^2 + (W_{U_{\text{eff}}})_{\text{Data aquisition}}^2} \quad (\text{F.74})$$

From Dantec manual the uncertainty in the calibration (of the automatic calibrator) is around 1%. Then effective velocity uncertainty equation will be,

$$W_{U_{\text{eff}}} = W_{U_i} = \sqrt{(0.01)^2 + \left(\frac{0.0012}{U_{\text{eff}}}\right)^2 (C_1 + C_2 \times E_i + C_3 \times E_i^2 + C_4 \times E_i^3)^2} \quad (\text{F.75})$$

The time-averaged flow velocities  $\bar{U}$  are calculated as:

$$\bar{U} = \frac{1}{N} \sum_{i=1}^N U_i \quad (\text{F.76})$$

The uncertainty is estimated as:

$$W(\bar{U}) = \sqrt{\sum_{i=1}^N \left(\frac{\partial \bar{U}}{\partial U_i} \times W(U_i)\right)^2} = \frac{1}{N} \sqrt{\sum_{i=1}^N (W_{U_i})^2} \quad (\text{F.77})$$

The root square means value is calculated as:

$$u_{\text{rms}} = \sqrt{\frac{1}{N} \sum_{i=1}^N (U_i - \bar{U})^2} \quad (\text{F.78})$$

The uncertainty is estimated as:



$$W(u_{rms}) = \sqrt{\left(\frac{\partial(u_{rms})}{\partial U_i} \times W(U_i)\right)^2 + \left(\frac{\partial(u_{rms})}{\partial \bar{U}} \times W(\bar{U})\right)^2} \quad (F.79)$$

$$\frac{\partial(u_{rms})}{\partial U_i} = \frac{\sum_{i=1}^N (U_i - \bar{U})^2}{N \times \sqrt{\frac{1}{N} \sum_{i=1}^N (U_i - \bar{U})^2}} \quad (F.80)$$

$$\frac{\partial(u_{rms})}{\partial \bar{U}} = -\frac{\sum_{i=1}^N (U_i - \bar{U})^2}{N \times \sqrt{\frac{1}{N} \sum_{i=1}^N (U_i - \bar{U})^2}} \quad (F.81)$$

So Equation F.75 can be expressed as

$$W(u_{rms}) = \sqrt{\left(\frac{\sum_{i=1}^N (U_i - \bar{U})^2}{N \times \sqrt{\frac{1}{N} \sum_{i=1}^N (U_i - \bar{U})^2}} \times W(U_i)\right)^2 + \left(-\frac{\sum_{i=1}^N (U_i - \bar{U})^2}{N \times \sqrt{\frac{1}{N} \sum_{i=1}^N (U_i - \bar{U})^2}} \times W(\bar{U})\right)^2} \quad (F.82)$$

$$W(u_{rms}) = \sqrt{\left(\frac{\sum_{i=1}^N (U_i - \bar{U})^2}{N \times \sqrt{\frac{1}{N} \sum_{i=1}^N (U_i - \bar{U})^2}}\right)^2 \times (W^2(U_i) + W^2(\bar{U}))} \quad (F.83)$$

In the current experiment the uncertainties of turbulence intensity is estimated by using a MatLab program and it is found to be  $\pm 0.5\%$ .

#### F.4 Uncertainty in integral length scale

The integral length scale  $\Lambda$  is calculated as explained in Sections 4.5, and its relative uncertainty is estimated as:

$$\frac{W_{\tau_\Lambda}}{\tau_\Lambda} = \sqrt{\left(\frac{W_{(u^2)}}{(u^2)}\right)^2 + \left(\frac{2 \times W_u}{u}\right)^2} \quad (F.84)$$

and,

$$\frac{W_\Lambda}{\Lambda} = \sqrt{\left(\frac{W_{\bar{U}}}{\bar{U}}\right)^2 + \left(\frac{W_{\tau_\Lambda}}{\tau_\Lambda}\right)^2} \quad (\text{F.85})$$

The variance of turbulence fluctuation velocities are calculated as:

$$\overline{u^2} = \frac{1}{N} \sum_{i=1}^N (U_i - \bar{U})^2 \quad (\text{F.86})$$

The uncertainty in the variance is estimated by:

$$W(\overline{u^2}) = \sqrt{\left(\frac{\partial(\overline{u^2})}{\partial U_i} \times W(U_i)\right)^2 + \left(\frac{\partial(\overline{u^2})}{\partial \bar{U}} \times W(\bar{U})\right)^2} \quad (\text{F.87})$$

$$\frac{\partial(\overline{u^2})}{\partial U_i} = \frac{2}{N} \sum_{i=1}^N (U_i - \bar{U}) \quad (\text{F.88})$$

$$\frac{\partial(\overline{u^2})}{\partial \bar{U}} = -\frac{2}{N} \sum_{i=1}^N (U_i - \bar{U}) \quad (\text{F.89})$$

So Equation F.83 becomes:

$$W(\overline{u^2}) = \sqrt{\left(\frac{2}{N} \sum_{i=1}^N (U_i - \bar{U}) \times W(U_i)\right)^2 + \left(\frac{2}{N} \sum_{i=1}^N (U_i - \bar{U}) \times W(\bar{U})\right)^2} \quad (\text{F.90})$$

$$W(\overline{u^2}) = \frac{2}{N} \sqrt{\left(\sum_{i=1}^N (U_i - \bar{U})\right)^2 \times (W^2(U_i) + W^2(\bar{U}))} \quad (\text{F.91})$$

The instantaneous fluctuating velocity is defined as,

$$u = U_i - \bar{U} \quad (\text{F.92})$$

and,

$$W_u = \sqrt{\left(\frac{\partial u}{\partial U_i} \times W_{U_i}\right)^2 + \left(\frac{\partial u}{\partial \bar{U}} \times W_{\bar{U}}\right)^2} \quad (\text{F.93})$$

But,

$$\frac{\partial u}{\partial U_i} = 1 \quad (\text{F.94})$$

$$\frac{\partial u}{\partial \bar{U}} = -1 \quad (\text{F.95})$$

Then,

$$W_u = \sqrt{(W_{U_i})^2 + (W_{\bar{U}})^2} \quad (\text{F.96})$$

Substituting Equation F.82 and Equation F.92 into Equation F.87, gives,

$$W(\overline{u^2}) = 2 \times \overline{u^2} \times W(u) \quad (\text{F.97})$$

Substituting Equation F.74 and Equation F.92 into Equation F.79, this will be,

$$W(u_{\text{rms}}) = \frac{\overline{u^2}}{u_{\text{rms}}} \times W(u) \quad (\text{F.98})$$

In the current experiment the uncertainties of integral length scale is calculated by using a MatLab program and it is found to be 12%. The absolute uncertainty in the plate location ( $x/d$ ) is estimated to be 0.2 and the relative uncertainty in the Taylor microscale is around 10%.

## Vita Auctoris

NAME: Nibras Younis

PLACE OF BIRTH: Baghdad, Iraq

YEAR OF BIRTH: 1965

EDUCATION: Baghdad college High school, Baghdad, Iraq  
1976-1982

University of Baghdad, Baghdad, Iraq  
1982-1986 B.Sc

University of Baghdad, Baghdad, Iraq  
1991-1994 M.Sc

University of Windsor, Windsor, Ontario,  
Canada  
2008-2009 M.Sc